Anderson Travia INTERACTION CROSS SECTIONS NEEDED FOR SIMULATION OF SECONDARY ELECTRON EMISSION SPECTRA FROM THIN METAL FOILS AFTER FAST PROTON IMPACT (Under the direction of Dr. Michael Dingfelder) Department of Physics, June 2009

Monte Carlo simulations of secondary electron emission from thin metal foils after fast proton impact require reliable interaction cross sections with the target under consideration. Total and energy differential inelastic cross sections have been derived for aluminum, copper, and gold thin-metal foils within the plane-wave first Born approximation (PWFBA) that factorizes the double cross section into the generalized oscillator strength and kinematic factors. The generalized oscillator strength or Bethe surface of the medium is obtained by using a semi-empirical optical oscillator strength distribution published in the literature and an extension algorithm based on the delta-oscillator model. Energy differential, total, and stopping cross sections are then obtained by simple integrations. Comparisons with other calculations and experimental values from the literature show that our model offers a good agreement in the energy range considered. As a final step, the cross sections and a transport model for copper have been implemented into the Monte Carlo track structure code PARTRAC where simulations of secondary electron emission spectra from copper foil have been performed.

INTERACTION CROSS SECTIONS NEEDED FOR SIMULATION OF SECONDARY ELECTRON EMISSION SPECTRA FROM THIN METAL FOILS AFTER FAST PROTON IMPACT

A THESIS
PRESENTED TO
THE FACULTY OF THE DEPARTMENT OF PHYSICS
EAST CAROLINA UNIVERSITY

In Partial Fulfillment
of the Requirements for the Degree
Master of Science in Applied Physics

by
Anderson Travia
June, 2009

INTERACTION CROSS SECTIONS NEEDED FOR SIMULATION OF SECONDARY ELECTRON EMISSION SPECTRA FROM THIN METAL FOILS AFTER FAST PROTON IMPACT

by

Anderson Travia

APPROVED BY:
DIRECTOR OF THESIS:

_____

Michael Dingfelder, Ph. D.

COMMITTEE MEMBER:

_____

Larry H. Toburen, Ph. D.

COMMITTEE MEMBER:

_____

Jefferson L. Shinpaugh, Ph. D.

COMMITTEE MEMBER:

_____

David W. Pravica, Ph. D.

INTERIM CHAIR OF THE DEPARTMENT OF PHYSICS:

_____

James M. Joyce, Ph. D.

DEAN OF GRADUATE SCHOOL:

_____

Paul J. Gemperline, Ph. D.

Acknowledgements

I would like to thank the Department of Physics of East Carolina University and in special Dr. Michael Dingfelder and Dr. Larry H. Toburen for providing the means for the conclusion of this project. Needless to say, without their generosity and assistance the conclusion of this study would be just impossible. Thank you very much for your lectures, comments, suggestions, and supervision. I also would like to thank Dr. Jefferson L. Shinpaugh and Dr. David W. Pravica for taking their time to read this work and for providing their also extremely important criticism. Finally, I would like to thank my wife for supporting me through this tough journey.

Table of Contents

List of Figures vii

1 Introduction 1

1.1 Initial facts and observations 1

1.2 Motivation and objectives 2

2 Theory 5

2.1 Basic principles 5

2.1.1 Cross-sections 5

2.1.2 From Maxwell's equations to differential cross-sections 8

2.2 The electric field due to an induced charged density 11

2.3 Modeling the current charge density 15

2.3.1 The point radiator 15

2.3.2 Scattering power for the oscillating free electron 16

2.3.3 The scattering cross-section of a single free electron 19

2.3.4 Scattering by bound electrons 22

2.3.5 Scattering by many-electron atoms 24

2.4 The atomic scattering factor and the oscillator strength 27

2.5 Bethe theory and the GOS of a material 30

2.6 GOS Hartree-Fock approximation for single atomic collision 32

2.7 DICS in condensed-phase - modeling the energy-loss function 35

2.7.1 The key quantity - energy-loss function 35

2.7.2 Link with the differential cross section and GOS 37

2.8 Monte Carlo simulation of radiation transport 39

2.8.1 Tracking of a charged particle 39

2.8.2 The probability distribution function and sampling methods 40

2.8.3 Random track generation 42

2.8.4 An example using a hypothetical mean-free-path PDF 43

3 Procedures 45

3.1 Consistency test for the OOS - sum-rule test 45

3.1.1 Aluminum OOS 48

3.1.2 Copper OOS 49

3.1.3 Gold OOS 50

3.2 Limits of integration 51

3.3 Shell separation 57

3.3.1 Aluminum edge-energies 58

3.3.2 Copper edge-energies 58

3.3.3 Gold edge-energies 58

3.4 Angular distribution of primary and secondary particles 66

3.4.1 Angular distribution of primary protons. 66

3.4.2 Angular distribution of primary electrons 68

3.4.3 Angular distribution of electrons induced by electron impact 69

3.4.4 Angular distribution of electrons induced by proton impact 70

3.4.5 Determination of A(w) and B(w) 70

3.4.6 Aluminum, copper, and gold Bethe coefficients 73

4 Results 79

4.1 Electron impact in aluminum, copper, and gold thin foils 80

4.1.1 Aluminum DIMFP, IMFP, and STP 80

4.1.2 Copper DIMFP, IMFP, and STP 83

4.1.3 Gold DIMFP, IMFP, and STP 86

4.2 Proton impact in aluminum, copper, and gold thin foils 89

4.2.1 Aluminum DIMFP, IMFP, and mass STP 89

4.2.2 Copper DIMFP, IMFP, and mass STP 92

4.2.3 Gold DIMFP, IMFP, and mass STP 95

4.3 Electron yields from 0.1 micron copper foil after 6 MeV proton impact 98

4.3.1 Forward electron yield 98

4.3.2 Backward electron yield 99

5 Conclusion and Remarks 100

References 102

List of Figures

1 Diagram for the scattering of an incident flux of particles J_{in} 7

2 Coordinate system in the direction of the propagation of the incident wave $\widehat{k}_0$ . . .14

3 $\sin^2\theta$ radiation pattern of a small accelerated charge 19

4 Many-electron atom in three random electronic spatial configurations 28

5 Graphical representation of the mean-free-path from a hypothetical PDF 44

6 Analysis of the integration routine used for integration of the OOS 47

7 Optical oscillator strength density distribution of aluminum. 48

8 Optical oscillator strength density distribution of copper 49

9 Optical oscillator strength density distribution of gold 50

10 Limits of integration for electron energy of 10 eV 52

11 Limits of integration for electron energy of 10 keV. 53

12 Limits of integration for proton energy of 100 eV. 54

13 Limits of integration for proton energy of 10 MeV 55

14 Aluminum OOS K, L, and M shell separation 59

15 Copper OOS K, L, and MN shell separation. 60

16 Gold OOS K, L, M, N, O, and P shell separation. 61

17 Aluminum shell coefficients 63

18 Copper shell coefficients 64

19 Gold shell coefficients. 65

20 Classical scattering kinematics 69

21 Bethe A coefficient, as defined in equation 114, for aluminum. 73

22 Bethe B coefficient, as defined in equation 115, for aluminum 74

23 Bethe A coefficient, as defined by equation 114, for copper 75

24 Bethe B coefficient, as defined by equation 115, for copper 76

25 Bethe A coefficient, as defined by equation 114, for gold. 77

26 Bethe B coefficient, as defined in equation 115, for gold 78

27 DIMFP of electrons in aluminum. 80

28 IMFP of electrons in aluminum 81

29 STP of aluminum for electron source. 82

30 DIMFP of electrons in copper. 83

31 IMFP of electrons in copper 84

32 STP of copper for electron source 85

33 DIMFP of electrons in gold 86

34 IMFP of electrons in gold 87

35 STP of gold for electron source 88

36 DIMFP of protons in aluminum. 89

37 IMFP of protons in aluminum 90

38 Mass STP of aluminum for proton source 91

39 DIMFP of protons in copper 92

40 IMFP of protons in copper. 93

41 Mass STP of copper for proton source. 94

42 DIMFP of protons in gold. 95

43 IMFP of protons in gold. 96

44 Mass STP of gold for proton source. 97

45 MC simulation of forward electron yields from copper foil. 98

46 MC simulation of backward electron yields from copper foil 99

1 Introduction

1.1 Initial facts and observations

The study of ionizing radiation is considered by many to begin with the work of the German physicist Wilhelm Conrad Röntgen and the discovery of X- rays in 1895 [1, 2]. Although the effects of X- rays on materials were not initially well understood, shortly after the announcement of its discovery, they were recognized as an important tool for medical diagnosis, but unfortunately for many patients, X-rays were widely adopted without a previous systematic and serious study of its dose-effect properties. It later became evident that X-rays could severely damage biological tissue and demanded a serious analysis not only of its possible applications but also of its ionization effects.

To understand a phenomenon such as ionizing radiation is to have the ability to completely describe its properties in particular, for obvious reasons, its effects on biological medium, for example, water and hydrocarbons. More generally, it includes the reliable capacity to accurately generate, measure, and predict its effects in all relevant systems. For the last 75 years, this has been an ongoing joined effort that includes scientific work specially in physics, chemistry, and biology that are developing the necessary theories and techniques while studying systems from full bodies of experimental animals to base deoxyribonucleic acid (DNA) sequences in target cells. Progressing from full organisms down to tissue, to cell, to chromosome, and to the gene, finally, the diverse biological effects of ionizing radiation can all ultimately be interpreted, understood, and explained in terms of disruptions in these building blocks or base sequences [3, 4].

1.2 Motivation and objectives

This particular study is part of a research project initiated a few years ago at East Carolina University, with two main purposes: To study the transport of secondary electrons in condensed phase and its spectra distribution when emitted from the targets and also to provide rigorous tests for Monte Carlo-based charged particle track structure models used in radiobiology.

The tests began with preliminary comparisons between experimental results of doubly differential electron-yields using two distinct experimental techniques (time of flight and electrostatic) for hydrocarbon targets (electron-yields at 45 degrees from CH_4, C_2H_6, and C_3H_8) and the simulation results from the event-by-event charged particle track structure Monte Carlo (MC) code PARTRAC using its semi-empirical cross section models for liquid water. The main purpose was to test the simulation at the fundamental physics level or before any reactions take place. Since discrepancies were observed between the results obtained from experiment and PARTRAC at the low and high energy ranges (< 50 eV and > 1 keV) and could not be completely clarified from this preliminary test on hydrocarbon foils using the water-cross sections available in PARTRAC, the project was extended to provide experimental data for amorphous solid water (ASW) and other important biological tissues. Exploration of the results from ASW are currently been done and the experimental data obtained for metals are very consistent and will provide an excellent testing ground [5].

Therefore, to make this starting test possible, new cross-sections representative of the metals, which are used as substrate in the experiment, needed to be calculated and implemented into PARTRAC using the similar plane-wave Born theory as it was previously done for water cross-sections used in PARTRAC. It is to fulfill this initial step that I began the study of the interaction of fast charged particles in condensed-phase media to obtain the necessary background to calculate these

cross-sections for aluminum, copper, and gold. This work requires the accomplishment of the following main steps:

- Collect and study key resources in classical electrodynamics and dielectric theory
- Study the plane wave first Born approximation (PWFBA) for description of sources or projectiles
- Understand the oscillator strength concept for the analytical representation of the targets
- Research and construct the optical oscillator strength (OOS) of the relevant target materials
- Research a simple dispersion algorithm for the construction of the generalized oscillator strength (GOS)
- Compare between the classical electrodynamics collision picture and the full quantum mechanical treatment
- Search for key quantities and expressions that are relevant for the determination of the desired differential inelastic cross sections (DICS)
- develop and optimize numerical procedures for the calculation of DICS, total cross sections (TCS), and consistency tests
- Format and graphically represent the obtained DICS and TCS calculations and compare them with well known results

It is hoped that this study in association with others that are currently being performed can help the group answer the questions that were set since the first data on carbon foils. For instance, it is desired to understand the phenomenon of metal and water foil-charging and its relation with the reduction of low energy electron-yields based on the physical properties of the foils [5].

2 Theory

2.1 Basic principles

2.1.1 Cross-sections

An incident charged particle interacts with another by exerting a Coulomb force on it that depends simultaneously on the charge of both particles and the distance of separation between them [6, 7]. Unfortunatelly, the study of the atomic structure and properties of materials usually involves the simultaneous interaction of a large amount of charged particles, which is known as a many body problem that is impossible to be precisely solved. Therefore, statistical tools must be employed when dealing with such problems, and if statistical fluctuations can be minimized by taking a large number of measurements, the searched properties and values can be inferred as an average over them. It is from this necessity that the concept of cross section comes to play a fundamental role in atomic physics.

Without being concerned with the precise way in which an incident particle interacts simultaneously with a large number of target particles, possibly exchanging energy and momentum with all of them, the desired properties are inferred by setting the measurement devices to only “count” or detect the particles that satisfy a pre-defined physical property. In an extremelly simplified way, this is experimentally done by setting the detector’s position with respect to the incident particle’s direction, adjusting the detector’s sensitivity, or measuring the scattering particle’s time-of-flight if the scattered particle’s momentum and energy are desired. From the following picture, see figure 1, the analytical representation of the cross section for a particular event can be constructed as:

Let an incident flux of particles per unit of target's area, J_{inc}, interact with a material. The scattered flux of particles within a solid angle $d\Omega = \sin\theta d\theta d\phi$, dN_s, measured from the center of the interaction area on the target to the detector's position is then expected to be proportional to this incident flux, which can be written as

$$\frac{dN_s(\theta,\phi)}{d\Omega} = \frac{d\sigma(\theta,\phi)}{d\Omega} J_{inc}, \tag{1}$$

where $\frac{d\sigma(\theta,\phi)}{d\Omega}$ is a proportionality constant, known as differential interaction cross-section that can then be expressed as

$$\frac{d\sigma(\theta,\phi)}{d\Omega} = \frac{1}{J_{inc}} \frac{dN_s(\theta,\phi)}{d\Omega}. \tag{2}$$

The total cross-section is given by

$$\sigma = \int \frac{d\sigma(\theta,\phi)}{d\Omega} d\Omega = \int_0^{\pi} \sin\theta d\theta \int_0^{2\pi} \frac{d\sigma(\theta,\phi)}{d\Omega} d\phi. \tag{3}$$

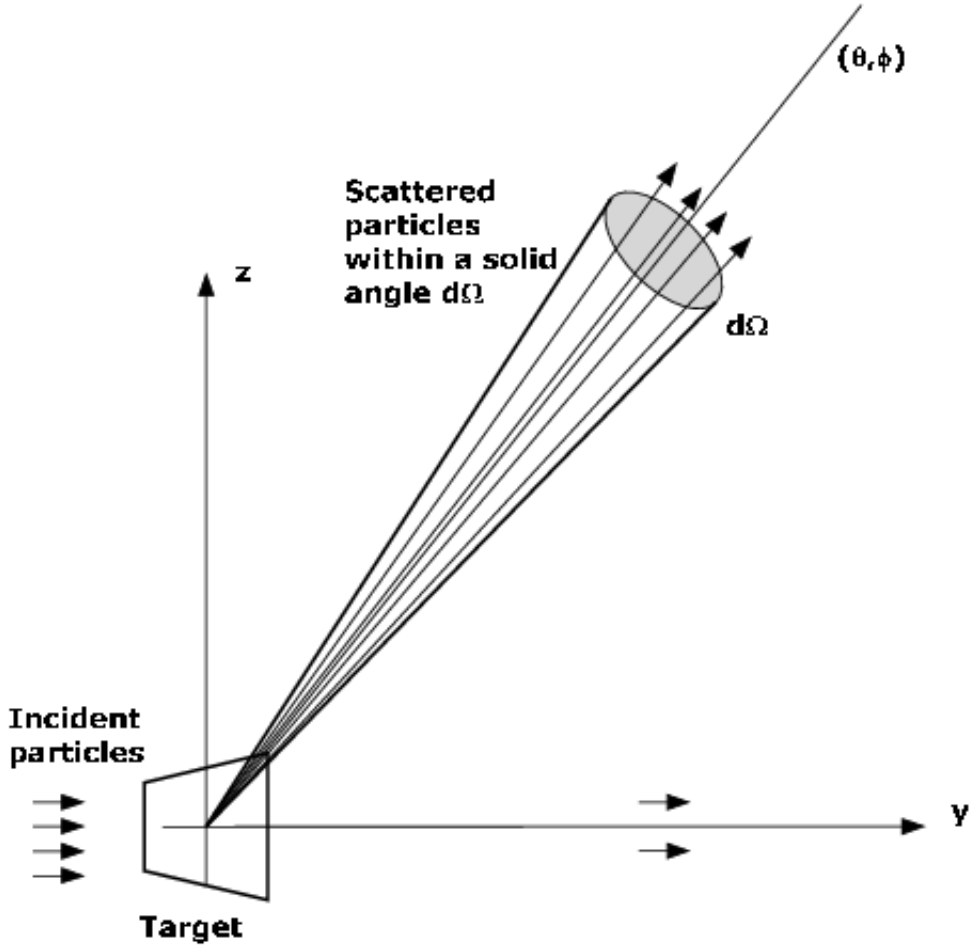

Figure 1: Diagram for the scattering of an incident flux of particles J_{in}.

After interaction with the target, only the flux of particles that have been scattered $dN_s(\theta,\phi)$ within a solid angle $d\Omega$ in the direction defined by the plane angles θ and ϕ will be considered in the determination of the proportionality factor between the incident flux and the scattered flux known as the differential cross section $\frac{d\sigma(\theta,\phi)}{d\Omega}$.

2.1.2 From Maxwell's equations to differential cross-sections

The above over-simplified pictorial description of the experimental determination of a differential cross-section can theoretically be more completely described from ab-initio classical electrodynamics that obviously starts from the well known four fundamental Maxwell's equations [6, 7, 8, 9]

In the following equations, let $\nabla = \overrightarrow{\nabla}$, $E = \overrightarrow{E}(\overrightarrow{r},t)$, $D = \overrightarrow{D}(\overrightarrow{r},t)$, $B = \overrightarrow{B}(\overrightarrow{r},t)$, $H = \overrightarrow{H}(\overrightarrow{r},t)$, $A = \overrightarrow{A}(\overrightarrow{r},t)$, $J = \overrightarrow{J}(\overrightarrow{r},t)$, and $\rho = \rho(\overrightarrow{r},t)$.

$$\nabla \times H = \frac{\partial D}{\partial t} + J, \tag{4}$$

$$\nabla \times E = -\frac{\partial B}{\partial t}, \tag{5}$$

$$\nabla \cdot B = 0, \tag{6}$$

and

$$\nabla \cdot D = \rho, \tag{7}$$

where the electrical displacement and induced magnetic field are respectively defined as

$$D = \varepsilon_0 E \tag{8}$$

and

$$B = \mu_0 H. \tag{9}$$

To study the interaction of an incident electromagnetic field due, for example, to an incident charged particle approaching the target with defined energy and momentum, we need to obtain the wave equation that describes the moving field. Recognizing the vector identity

$$\nabla \times (\nabla \times A) = \nabla(\nabla \cdot A) - \nabla^2 A, \tag{10}$$

the wave equation is obtained after following some basic steps, which start by taking the curl of the Faraday's Law. Following, is the complete derivation.

$$\nabla \times (\nabla \times E) = \nabla \times \left(-\frac{\partial B}{\partial t}\right)$$

$$\nabla(\nabla \cdot E) - \nabla^2 E = -\mu_0 \frac{\partial}{\partial t}(\nabla \times H)$$

$$\vec{\nabla}\left(\frac{\rho}{\varepsilon_0}\right) - \vec{\nabla}^2 E = -\mu_0 \frac{\partial}{\partial t}\left(\frac{\partial \vec{D}}{\partial t} + \vec{J}\right)$$

$$\nabla\left(\frac{\rho}{\varepsilon_0}\right) - \nabla^2 E - \varepsilon_0 \mu_0 \frac{\partial}{\partial t}\left(\frac{\partial E}{\partial t} + \frac{J}{\varepsilon_0}\right)$$

$$\varepsilon_0\mu_0\frac{\partial^2 E}{\partial t^2}-\nabla^2 E=-\mu_0\frac{\partial J}{\partial t}-\frac{1}{\varepsilon_0}\vec{\nabla}\rho$$

$$\left(\frac{\partial^2}{\partial t^2}-c^2\nabla^2\right)E=-\frac{1}{\varepsilon_0}\left[\frac{\partial J}{\partial t}+c^2\nabla\rho\right]$$

Note that

$$c\equiv\frac{1}{\sqrt{\varepsilon_0\mu_0}}$$

is the phase velocity of the moving radiation in vacuum, which is often referred as the speed of “light in vacuum” with ε_0 and μ_0 being the electric permitivity and magnetic permeability of free space.

This wave equation is then the point of departure for explaining all the properties of interest involving, for example, propagation, reflection, refraction, and in special for this study the scattering processes with single and many-electron atoms involving free and bound electrons.

Looking back into the wave-equation, we can interpret it as an association between induced source terms on the right of the equation, given by the current and charge densities, and the field they generate. Therefore, by appropriately representing the response of the target to an incident electric field through the current and charge densities induced in the material, the new field resulting from the induction process can be in principle calculated.

The objective is then to solve the wave equation for the radiated electric field $E(r,t)$ in the presence of accelerated source terms represented by free or bound electrons and

combine this field with the incident polarization agent or inductive field to obtain the resulting scattering wave.

2.2 The electric field due to an induced current charge density

To solve the wave equation

$$\left(\frac{\partial^2}{\partial t^2} - c^2\nabla^2\right)E = -\frac{1}{\varepsilon_0}\left[\frac{\partial J}{\partial t} + c^2\nabla\rho\right] \tag{11}$$

for $E(r,t)$, in the presence of source terms, we can treat the quantity between parentheses on the left of equation 11 as an operator and consider solving for $E(r,t)$ for arbitrary sources with the form

$$E(r,t) = \int [G(r,t)]\,[source]\,dr, \tag{12}$$

where $G(r,t)$ represents the Green's or response function due to the source term [10, 11]. This can be considerably simplified if we move to the temporal ω and spatial k frequency domains that are connected to the coordinate r space through the Fourier-Laplace transforms

$$E(\overrightarrow{r},t) = \int_k\int_\omega E_{k\omega}e^{-i(\omega t - \overrightarrow{k}\cdot\overrightarrow{r})}\frac{d\omega dk}{(2\pi)^4} \tag{13}$$

and

$$E_{k\omega} = \int_r \int_t E(\overrightarrow{r}, t) e^{i(\omega t - \overrightarrow{k} \cdot \overrightarrow{r})} dr dt, \tag{14}$$

where $d\omega$ and dk correspond to scalar volume elements, $E_{k\omega} = E(k, \omega)$, and $\omega = \omega_r + i\omega_i$, with $\omega_i > 0$. This is necessary for the convergence of equation 14 when $t \to \infty$.

Thus, in Laplace-Fourier space, the wave equation in operator form simplifies to

$$(\omega^2 - k^2 c^2) E_{k\omega} = \frac{1}{\varepsilon_0} \left[(-i\omega) J_{k\omega} + ic^2 k \rho_{k\omega} \right], \tag{15}$$

which can be solved for the electric field.

The path is clear now. If we construct appropriate models for the sources $J(r,t)$ and $\rho(r,t)$, we can obtain the electric field from equation 15.

Using the equation for charge conservation

$$\nabla \cdot J + \frac{\partial \rho}{\partial t} = 0, \tag{16}$$

which is derived by taking the divergence of Ampere's Law and the known vector relation $\nabla \cdot (\nabla \times A) = 0$, the charge density can be written as

$$\rho_{k\omega} = \frac{\overrightarrow{k} \cdot J_{k\omega}}{\omega}. \tag{17}$$

Finally, the electric field can be written as

$$E_{k\omega} = -\frac{i\omega}{\varepsilon_0}\left[\frac{J_{k\omega} - \hat{k}_0(\hat{k_0}\cdot J_{k\omega})}{\omega^2 - k^2c^2}\right], \tag{18}$$

where $\vec{k} = k\hat{k}_0$ with $k = \frac{2\pi}{\lambda}$.

Equation 18 can be further simplified if we adopt a coordinate system oriented around the propagation direction defined by the unit vector $\hat{k}_0$, please see figure 2, and decompose the source as $J_{k\omega} = J_{Tk\omega} + |J_{Lk\omega}|\vec{k}_0$ with transverse and longitudinal components. It can then be finally be expressed as

$$E_{k\omega} = -\frac{i\omega}{\varepsilon_0}\frac{J_{Tk\omega}}{\omega^2 - k^2c^2}, \tag{19}$$

with its real-space representation

$$E(r,t) = \int_k\int_\omega \left(-\frac{i\omega}{\varepsilon_0}\right)\frac{J_{Tk\omega}e^{-i(\omega t - k\cdot r)}}{(\omega^2 - k^2c^2)}\frac{d\omega dk}{(2\pi)^4}. \tag{20}$$

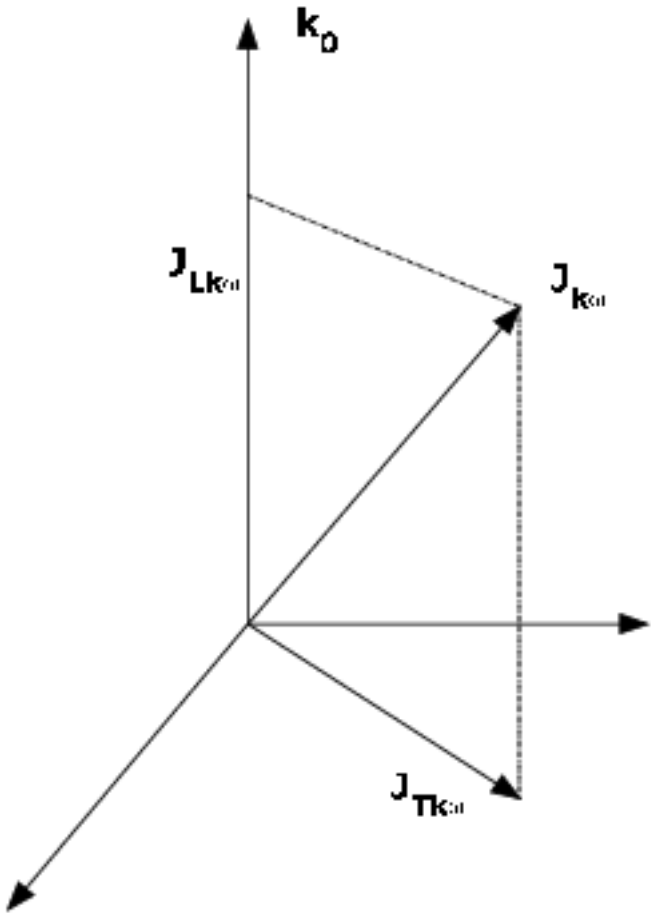

Figure 2: Coordinate system in the direction of the propagation of the incident wave $\hat{k}_0$. This simplifies the expression describing the radiation field $E_{k\omega}$ through the decomposition of J_{kw} into longitudinal J_{Lkw} and transverse J_{Tkw} components.

2.3 Modeling the current charge density

2.3.1 The point radiator

Lets initially consider the case of an accelerating free electron that is small when compared with the wavelength of the radiating field, thus allowing us to represent its charge density by a Dirac delta function [6, 7, 8]. Thus, the moving electron can be expressed as a current density given by

$$J = qn(r,t)\overrightarrow{v}(r,t), \tag{21}$$

where q is the charge, n represents the particle number density, and $\overrightarrow{v}$ the particle's velocity.

The real-space and Laplace-Fourier space current densities are repectively

$$J = -e\delta(r)\overrightarrow{v}(t),$$

where in Cartesian coordinates $\delta(r) = \delta(x)\delta(y)\delta(z)$,

and

$$J_{k\omega} = -e\overrightarrow{v}(\omega), \tag{22}$$

with transverse component

$$J_{Tk\omega} = -e\overrightarrow{v}_T(\omega). \tag{23}$$

Substituting this current density back into equation 20 and integrating we can recognize the expected connection between the radiated field and the particle's acceleration given by

$$E = \frac{e}{4\pi\varepsilon_0 c^2 r}\frac{d\overrightarrow{v}_T(t-r/c)}{dt} \tag{24}$$

and

$$E = \frac{e\overrightarrow{a}_T(t-r/c)}{4\pi\varepsilon_0 c^2 r}. \tag{25}$$

2.3.2 Scattering power for the oscillating free electron

The Poynting vector (energy flow or power per unit area) in electromagnetic theory is given by [6, 7]

$$\overrightarrow{S}(\overrightarrow{r},t) = E \times H. \tag{26}$$

Again from Faraday's Law and the definition of magnetic induction we can derive the Magnetic field H as follows

$$\nabla \times E = -\frac{\partial B}{\partial t}$$

$$B = \mu_0 H$$

$$\nabla \times E = -\mu_0 \frac{\partial H}{\partial t}$$

$$i\hat{k} \times E_{k\omega} = i\omega\mu_0 H_{k\omega},$$

from which we obtain

$$H_{k\omega} = \sqrt{\frac{\varepsilon_0}{\mu_0}}\hat{k}_0 \times E_{k\omega}, \tag{27}$$

where $\omega = kc$,with $c = \frac{1}{\sqrt{\varepsilon_0\mu_0}}$ for propagation in free space.

Using the vector identity $A \times (B \times C) = (A \cdot C)B - (A \cdot B)C$ and the fact that for transverse waves $\hat{k}_0 \cdot E = 0$, we obtain

$$\overrightarrow{S}(\overrightarrow{r},t) = \frac{1}{Z_0}|E|^2\widehat{k}_0, \tag{28}$$

where $Z_0 = \sqrt{\frac{\mu_0}{\varepsilon_0}}$ is the impedance of free space.

Noting that $a_T = |\vec{a}_T| = |\vec{a}| \sin\theta$ the radiated power $\vec{S}(\vec{r},t)$ can be represented by the acceleration, which reveals the familiar form for the dipole radiation [6, 7], see figure 3 below.

$$\vec{S}(\vec{r},t) = \frac{e^2|\vec{a}|^2 \sin^2\theta}{16\pi^2\varepsilon_0 c^3 r^2}\hat{k}_0 \tag{29}$$

or

$$\frac{dP}{d\Omega} = \frac{e^2|\vec{a}|^2 \sin^2\theta}{16\pi^2\varepsilon_0 c^3}, \tag{30}$$

where $\vec{S}(\vec{r},t) = \frac{dP}{dA}\hat{k}_0$, for $dA = r^2 d\Omega$.

The total power radiated immediately follows from the integration of equation 30,

$$P = \frac{8\pi}{3}\left(\frac{e^2|\vec{a}|^2}{16\pi^2\varepsilon_0 c^3}\right). \tag{31}$$

Note that the average radiated power, which is used in the calculation of the differential cross section for the radiation of an accelerated charged electron in the direction defined by the acceleration vector $\vec{a}(\vec{r},t)$ can be expressed as [6, 7]

$$\bar{\vec{S}} = \frac{1}{2}Re[E \times H^*] \tag{32}$$

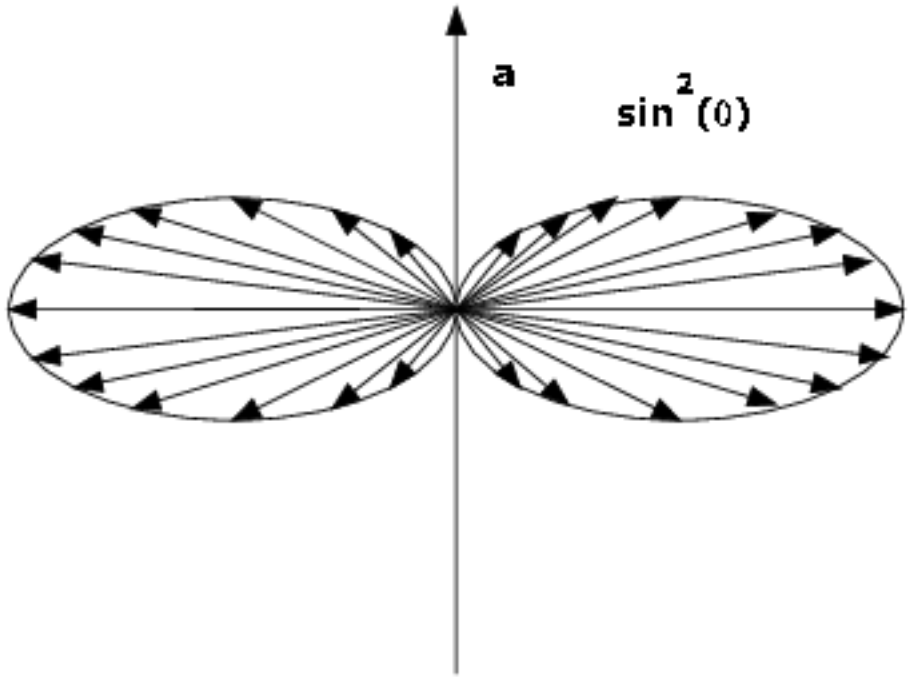

Figure 3: $\sin^2\theta$ radiation pattern of a small accelerated charge.

2.3.3 The scattering cross-section of a single free electron

Now that we know the radiation power of the point oscillator, we can calculate the scattering cross section by defining it as the ratio between the average scattered power $\bar{P}_{sc}$ and the average total incident power $|\bar{\vec{S}}_i|$,

$$\sigma = \frac{\bar{P}_{sc}}{|\bar{\vec{S}}_i|}. \tag{33}$$

Let a free electron experience the oscillatory Lorentz force

$$\overrightarrow{F} = -e\left[E_i + \overrightarrow{v} \times B_i\right], \tag{34}$$

when in the presence of an incident field

$$E_i(r,t) = E_0 e^{-i(\omega t - \overrightarrow{k}\cdot\overrightarrow{r})}. \tag{35}$$

The equation of motion is then given by

$$m\overrightarrow{a} = -e\left[E_i + \overrightarrow{v} \times B_i\right]. \tag{36}$$

The magnetic induction in this case is expressed as

$$B_i(r,t) = \frac{\hat{k}_0 \times E_i(\overrightarrow{r},t)}{c}. \tag{37}$$

Thus, we can neglect the $\overrightarrow{v} \times B_i$, in equation 36 since it is proportional to v/c, which is very small for non-relativistic velocities and equation 36 simplifies to

$$\overrightarrow{a}(\overrightarrow{r},t) = -\frac{e}{m}E_i(\overrightarrow{r},t). \tag{38}$$

The transverse component is obviously obtained by

$$a_T = a\sin\theta = -\frac{e}{m}|E_i|\sin\theta. \tag{39}$$

Introducing the electron radius $r_e = \frac{e^2}{4\pi\varepsilon_0 mc^2}$, the scattered electric field in the direction θ with respect to the polarization direction of the incident field,

$$E(\overrightarrow{r},t) = -\frac{e^2|E_i|\sin\theta}{4\pi\varepsilon_0 mc^2 r}e^{-i\omega(t-r/c)}, \tag{40}$$

can be more compactly written as

$$E(\overrightarrow{r},t) = -\frac{r_e|E_i|\sin\theta}{r}e^{-i\omega(t-r/c)}. \tag{41}$$

Therefore, the single free-electron scattering cross section (Thomson) can be written as

$$\sigma = \frac{\overline{P_{sc}}}{|\overline{S_i}|} = \frac{\frac{4\pi}{3}\left(\frac{e^4|E_i|^2}{16\pi^2\varepsilon_0 m^2c^3}\right)}{\frac{1}{2}\sqrt{\frac{\varepsilon_0}{\mu_0}}|E_i|^2} \tag{42}$$

or

$$\sigma_e = \frac{8\pi}{3}r_e^2. \tag{43}$$

The differential form follows as,

$$\frac{d\sigma_e}{d\Omega} = \frac{1}{|S_i|}\frac{d\bar{P}}{d\Omega} \tag{44}$$

or

$$\frac{d\sigma_e}{d\Omega} = r_e^2 \sin^2\theta. \tag{45}$$

2.3.4 Scattering by bound electrons

The approach for the calculation of the scattering cross section for bound electrons is similar to the one used for free electrons as described above. First a connection between the radiated field and the charged particles' acceleration is constructed. The acceleration is then obtained from a model for the motion of the charges and the cross section is finally obtained from the radiated power and the total power. What changes in each case is the equation of motion.

The model we will use for bound electrons accounts for the discrete binding energies of each electron and considers that the relatively massive nucleus with charge $+Ze$ does not respond dynamically to the high frequency incident field. On the other hand, the electrons are set in oscillatory motion with frequency imposed by the passing electromagnetic field. The response of each electron to the incident field is directly related to their individual resonance frequency that reflects the different restoring

forces upon them. Thus, the influence of the incident field on the motion of a particular electron depends on how close the incident frequency is to the resonance frequency of that particular electron.

Let the equation of motion of a bound electron be expressed as

$$m\frac{d^2\vec{x}}{dt^2} + m\gamma\frac{d\vec{x}}{dt} + m\omega_s^2\vec{x} = -e\left[E_i + \vec{v} \times Bi\right], \tag{46}$$

which involves the acceleration $\frac{d^2\vec{x}}{dx^2}$ of the electron with mass m, a dissipative force to account for the energy loss with a damping factor γ defined by $m\gamma\frac{d\vec{x}}{dt}$, and a restoring force $m\omega_s^2\vec{x}$ for an oscillatory motion with resonance frequency ω_s. Again we can neglect the $\vec{v} \times B_i$ term for non-relativistic velocities.

For an incident field of the form $\vec{E}(\vec{r},t) = E_i e^{-i\omega t}$, we can expect the displacement, velocity, and acceleration to contain the same $e^{-i\omega t}$ time dependence. Therefore, the equation can be written as

$$\left[m(-i\omega)^2\vec{x} + m\gamma(-i\omega)\vec{x} + m\omega_s^2\vec{x} = -eE_i\right]e^{-i\omega t}, \tag{47}$$

from which we finally obtain

$$\vec{x} = \frac{e^{-i\omega t}}{\omega^2 - \omega_s^2 + i\gamma\omega}\frac{eE_i}{m} \tag{48}$$

and

$$\overrightarrow{a} = \frac{-\omega^2 e^{-i\omega t}}{\omega^2 - \omega_s^2 + i\gamma\omega} \frac{eE_i}{m}. \tag{49}$$

Following the same, already given, free-electron procedures, the semi-classical scattering cross section for a bound electron of resonance frequency ω_s is given by

$$\sigma = \frac{8\pi}{3} r_e^2 \frac{\omega^4}{(\omega^2 - \omega_s^2)^2 + (\gamma\omega)^2}. \tag{50}$$

2.3.5 Scattering by many-electron atom

Using an electron distribution for this semi-classical model of multi-electron atom that can be written as

$$n(\overrightarrow{r}, t) = \sum_{s=1}^{Z} \delta(\overrightarrow{r} - \triangle \overrightarrow{r}_s(t)), \tag{51}$$

where r is the nucleus' coordinate, $\triangle \overrightarrow{r}$ the vector displacement from the nucleus, and Z the total number of electrons held by the atom, we can write the charge distribution as

$$J(\overrightarrow{r}, t) = -e \sum_{s=1}^{Z} \delta(\overrightarrow{r} - \triangle \overrightarrow{r}_s(t)) \overrightarrow{v}_s(t). \tag{52}$$

Applying the Born approximation, which neglects the effects due to neighboring electrons and assumes that $\overrightarrow{v}_s(t)$ will be dominated by the incident field only and following steps similar to the ones for bound electrons, which are all well explained in [6, 8, 12, 13], first the current density is again expressed in $k-\omega$ space by

$$J_{k\omega} = -e\sum_{s=1}^{Z} e^{-i\overrightarrow{k}\cdot\triangle\overrightarrow{r}}\overrightarrow{v}_s(\omega), \tag{53}$$

and the electric field is given by

$$E(\overrightarrow{r},t) = -\frac{e}{\varepsilon_0}\sum_{s=1}^{Z}\int_k\int_\omega \frac{(-i\omega)e^{i\overrightarrow{k}\cdot(\overrightarrow{r}-\triangle\overrightarrow{r}_s)}\overrightarrow{v}_{Ts}(\omega)e^{-i\omega t}}{(\omega-kc)(\omega+kc)}\frac{dkd\omega}{(2\pi)^4}. \tag{54}$$

Letting $\overrightarrow{r}_s \equiv \overrightarrow{r}-\triangle\overrightarrow{r}$, we finally obtain

$$E(\overrightarrow{r},t) = \frac{e}{4\pi\varepsilon_0 c^2}\sum_{s=1}^{Z}\frac{\overrightarrow{a}_{Ts}(t-r_s/c)}{r_s}. \tag{55}$$

The complete form involving the angular dependence is given by

$$E(\overrightarrow{r},t) = -\frac{r_e}{r}f(\triangle\overrightarrow{k},\omega)|E_i|\sin\theta e^{-i\omega(t-r/c)}, \tag{56}$$

where

$$f(\triangle \overrightarrow{k}, \omega) = \sum_{s=1}^{Z} \frac{\omega^2 e^{-i\triangle \overrightarrow{k} . \triangle \overrightarrow{r}_s}}{(\omega^2 - \omega_s^2 + i\gamma\omega)} \tag{57}$$

is the complex atomic scattering factor.

The differential and total scattering cross sections are then written as

$$\frac{d\sigma}{d\Omega} = r_e^2 |f|^2 \sin^2\theta \tag{58}$$

and

$$\sigma = \frac{8\pi}{3} r_e^2 |f|^2. \tag{59}$$

2.4 The atomic scattering factor and the oscillator strength

The atomic scattering factor in equation 57 presents a phase factor $e^{-i\triangle \overrightarrow{k} \cdot \triangle \overrightarrow{r}_s}$, please see figure 4, to account for the different positions of the electrons in the atom. A simplification is possible for the case of forward scattering and also in the long wavelength limit. In each of these two cases, the atomic scattering factor $f(\Delta \overrightarrow{k}, \omega)$ reduces to

$$f^0(\omega) = \sum_{s=1}^{Z} \frac{\omega^2}{\omega^2 - \omega_s^2 + i\gamma\omega}. \tag{60}$$

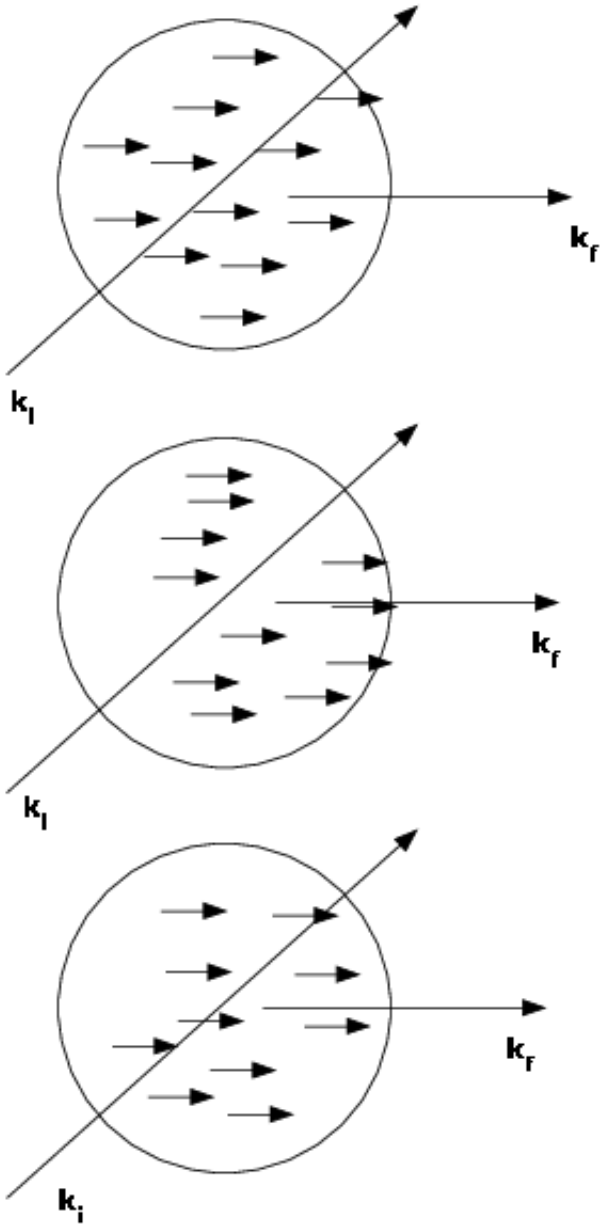

Figure 4: Many-electron atom in three random electronic spatial configurations.

Although some electrons may experience the same incident phase in the $\overrightarrow{k}_i$ direction, the scattering field due to each electron has distinct phase as seen by an observer in the $\overrightarrow{k}_f$ direction.

Letting g_s , known as the oscillator strength of the atom, indicates the fraction of oscillators of the system associated with a given resonance frequency it is then required that

$$\sum_s g_s = Z, \tag{61}$$

which allows the re-writing of the forward atomic scattering factor to be

$$f^0(\omega) = \sum_s \frac{g_s \omega^2}{\omega^2 - \omega_s^2 + i\gamma\omega} = f_1^0(\omega) + i f_2^0(\omega). \tag{62}$$

The forward atomic scattering factor, is usually calculated by first obtaining the imaginary part $f_2^0(\omega)$ from photo-absorption experiments. The absorption coefficient (μ) is measured and $f_2^0(\omega)$ calculated through

$$\mu = \frac{2r_e\lambda}{Am_u} f_2^0(\omega). \tag{63}$$

Finally, Kramers-Kronig relations are used to derive the real part.

This classical approach brings to light two important features of the cross-section calculation in the more general case of scattering from bound electrons: First, it shows that the target's response to a specific type of interaction can be described by a single complex quantity named the atomic scattering factor. Second, and more important, it offers a way to link the theory with experiment through the determination of absorption

coefficients of materials. Although not complete, the classical theory description of interaction cross sections presents these two properties or ideas that will remain in the treatment of the interaction between fast charged particles and single atoms as given by Bethe's full quantum theory and in condensed-phase targets using the dielectric theory.

2.5 Bethe theory and the GOS of a material

Tracing back the theoretical work that lead to current understanding of the inelastic interaction between charged particles and the stopping power of materials, among many important contributions we can mention some key specific work: N. H. D. Bohr in 1913 for his derivation of an explicit formula for the stopping power for heavy charged particles using full classical treatment that relied in part on intuition and insight due to the not yet available quantum theory; to H. A. Bethe for the development of the full quantum theory of stopping power of materials in gas-phase or by single atomic interaction in the 1930s [14, 15, 16]; to E. Fermi for his semi-classical theory for the energy-loss in gasses and in condensed materials [17], to J. Lindhard, J. Hubbard and R. H. Ritchie in the 1950s for showing that the inelastic interaction of charged particles in condensed-phase materials is best described by the dielectric function of the medium [18], and to U. Fano for applying the dielectric theory to various penetration phenomena and extending Bethe's theory to condensed-phase materials in 1963 [19].

Summarizing what is presented in detail by Inokuti [13, 14, 15, 16], Bethe's inelastic differential cross section for fast collisions, where the velocity of the incident particle is much greater than the electron's mean orbital velocity in the shell under consideration, is constructed under the first Born approximation of the interaction field and views the collision as a suden and small external perturbation in the target's field caused by the projectile. Under these considerations, the expression of the differential cross-section for the exchange of energy and momentum factorizes into two distinct

terms - a kinematical term involving properties of the projectile only and a term, called the generalized oscillator strength (GOS), which stores all the target's properties.

The expression is given by

$$d\sigma_n = 2\pi Z^2 e^4 (mv^2)^{-1} q^{-1} |\varepsilon_n(q)|^2 d(\ln q), \tag{64}$$

where Z, v, and m are respectively the electric charge, the velocity, and the rest mass of the incident particle, e is the electron's charge, $\hbar\overrightarrow{K} = \hbar(\overrightarrow{k}_i - \overrightarrow{k}_f)$ is the projectile's change in momentum, and $q = \frac{(\hbar\overrightarrow{K})^2}{2m}$ the recoil energy, which are all related exclusively to the projectile. $|\varepsilon_n(q)|^2$ represents the conditional probability that the target-atom undergoes a transition from ground-state $|0\rangle$ to an excited state $|n\rangle$ when receiving a momentum transfer of $\hbar\overrightarrow{K}$ after the collision. $\varepsilon_n(q)$ is called the inelastic-scattering form factor and carries the dynamics of the target atom only.

Realizing the connection between the form factor and the familiar optical dipole oscillator strength f_n, Bethe introduced a new quantity called the generalized oscillator strength, which is related to the inelastic-scattering form factor by

$$f_n(q) = \frac{E_n}{q} |\varepsilon_n(q)|^2, \tag{65}$$

and to the dipole oscilator strength through

$$f_n = \frac{E_n}{R} M_n^2, \tag{66}$$

where

$$M_n^2 = \left| \frac{1}{a_0} \int \psi_n^* \sum_{j=1}^{z} x_j \psi_0 dr_1 ... dr_z \right|^2, \tag{67}$$

where a_0 is the Bohr radius, z the total number of electrons, x_j a component of r_j, and finally, $\psi_0(r_1,...,r_z)$ and $\psi_n(r_1,...,r_z)$ are the many-body eigenfunctions for the ground and excited states respectively.

Recalling similarity with the classical derivation from ab-initio electrodynamics, in the long wavelength limit, the optical oscillator strength f_n is proportional to photon-absorption cross section, which offers an extremely important link between Bethe's theory and experimental results.

2.6 GOS Hartree-Fock approximation for single atomic collision

As well explained in [13, 14, 15, 19], for large impact energies, the excitation or ionization in the encounter of a proton with charge Z_p and mass M with an atom in the first Born approximation can be written as [20, 21]

$$Q_{0n}(E) = \frac{2\pi Z_p^2 M}{E(E_n - E_0)} \int_{q_{min}}^{q_{max}} f_{0n}(q) \frac{dq}{q}, \tag{68}$$

where E is the energy of the incident particle, q is its change in momentum after scattering, and E_0 and E_n are the eigenvalues of the initial and final states of the target.

The GOS for a particular transition $f_{0n}(q)$ is defined as

$$f_{0n}(q) = \frac{2}{q^2}(E_n - E_0)|\varepsilon_{0n}(q)|^2, \tag{69}$$

where

$$\varepsilon_{0n}(q) = \sum_{s=1}^{z} \int \int \Psi_n^*(r_1, ..., r_s) exp(iqz_s) \Psi_0(r_1, ..., r_s) dr_1 ... dr_s. \tag{70}$$

$\Psi_0(r_1, ...r_s)$ and $\Psi_n(r_1, ...r_s)$ are respectively the eigenfunctions of the initial and final states of the target.

Note that the necessary functions needed to describe the initial and final states of the target are only available for the simplest targets and approximation techniques to derive these functions must be employed for more complex systems with more than one electron. A common method is the Hartree-Fock approximation, which neglects nuclei kinetic energy and adopts constant repulsion between them [22, 23]. In this approximation, the electronic Hamiltonian is described as

$$H_{elec} = -\sum_{i=1}^{N} \frac{1}{2} \nabla_i^2 - \sum_{i=1}^{N} \sum_{A=1}^{M} \frac{Z_A}{r_{iA}} + \sum_{i=1}^{N} \sum_{j>i}^{N} \frac{1}{r_{ij}}, \tag{71}$$

and when inserted into the Schrödinger equation

$$H_{elec} \Phi_{elec} = \varepsilon_{elec} \Phi_{elec}, \tag{72}$$

provides the solution

$$\Phi_{elec} = \Phi_{elec}(\{r_i\};\{R_A\}), \tag{73}$$

which describes the motion of the electrons with explicit dependence on the electronic coordinates and parametric dependence on the nuclear coordinates. Same as the electronic energy

$$\varepsilon_{elec} = \varepsilon_{elec}(\{R_A\}). \tag{74}$$

The parametric dependence means that, for different arrangements of the nuclei, Φ_{elec} is a different function of the electronic coordinates.

In the Hartree-Fock theory, the many-electron wave function, which describes the electron's motion and spin are composed by the product of a spatial function or orbital $\Psi(r)$ and a spin orbital $\alpha(r,\uparrow)$ or $\beta(r,\downarrow)$. Since the Hartree product does not account for antisymmetry $\Psi(r_1,r_2) = -\Psi(r_2,r_1)$ and correlation, they are modified by representing the wave functions as single Slater determinantes or as a linear combination of them to supply antisymmetry and correlation properties. For a two electron system, for example, it can be written as

$$\Psi(r_1,r_2) = 2^{-1/2}\begin{vmatrix} \chi_i(r_1) & \chi_j(r_1) \\ \chi_i(r_2) & \chi_j(r_2) \end{vmatrix}, \tag{75}$$

where $\chi(r) = \left\{ \begin{array}{c} \Psi(r)\alpha(r,\uparrow) \\ or \\ \Psi(r)\beta(r,\downarrow) \end{array} \right\}$.

Finally, for a general N-electron system we write [22, 23]

$$\Psi(r_1, r_2) = (N!)^{-1/2} \begin{vmatrix} \chi_i(r_1) & \chi_j(r_1) & \dots & \chi_k(r_1) \\ \chi_i(r_2) & \chi_j(r_2) & \dots & \chi_k(r_2) \\ \dots & \dots & \dots & \dots \\ \chi_i(r_N) & \chi_j(r_N) & \dots & \chi_k(r_N) \end{vmatrix}. \quad (76)$$

A clear presentation of the Hartree-Fock method is given in [22, 23].

2.7 DICS in condensed-phase - modeling the energy-loss function

2.7.1 The key quantity - energy-loss function

Finally, we reach the point where we can present in more detail the theoretical approach that will be used in this work for the determination of the inelastic cross-sections for the interaction of fast protons and electrons in uniform and isotropic thin foils of aluminum, copper, and gold. In principle, there are two methods from where we can derive inelastic cross-sections: the microscopic, in which the Hamiltonian of the system is constructed and the eigenfunctions optimized and linked to the material's dynamic-factor or inelastic form-factor using approximation methods as the Hartree-Fock self-consistent method concisely described above, and the macroscopic or dielectric function formalism.

As it was first shown by Lindhard, Hubbard, and Ritchie in the 1950s [18], for condensed-phase systems where its many-body features are very strong and cannot be neglected, the inelastic interaction of charged particles is best described by the dielectric properties of the medium (dielectric formalism) where the energy-loss-function is the key quantity of the theory and it can be obtained

experimentally from spectroscopic techniques. An important advantage of this method is that the energy-loss function, in the long wavelength limit, can be constructed from optical measurements [24].

In this approach, the dielectric constant of the medium ε is generalized to address absorption of energy, through the energy-loss $w = \hbar\omega$ dependence, and scattering properties, through the momentum transfer $q = \hbar K$ dependence, of the target medium to external perturbations. It is then a complex dielectric function that can be written as

$$\varepsilon(w,q) = \varepsilon_1(w,q) + i\varepsilon_2(w,q), \tag{77}$$

where w and q are respectively the energy and momentum transfer with K being a scalar for uniform and isotropic materials. Usually, the imaginary component of the dielectric function $\varepsilon(\omega,q)$ is obtained from experiment and the real term derived from Kramers-Kronig relations [6, 11, 25, 26]. The energy-loss function, which plays a central role in the slowing-down of fast charged particles is then defined as [13, 18, 19, 24, 27, 28].

$$\eta_2(w,q) = \Im\left[\frac{-1}{\varepsilon(w,q)}\right] = \frac{\varepsilon_2(w,q)}{\varepsilon_1^2(w,q) + \varepsilon_2^2(w,q)}, \tag{78}$$

where $\Im\left[\frac{-1}{\varepsilon(w,q)}\right]$ represents the imaginary part of $\frac{-1}{\varepsilon(w,q)}$.

2.7.2 Link with the differential cross-section and GOS

In the non-relativistic limit and under the first Born approximation, the fundamental element from which we can derive all the other desired quantities is the double differential inelastic macroscopic cross-section (DDICS) that is expressed by [13, 27, 28]

$$\frac{d^2\Sigma}{dqdw}(E;w,q) = \frac{1}{\pi a_0 E}\frac{\eta_2(w,q)}{q}, \tag{79}$$

where

$$\eta_2(w,q) = \frac{\pi}{2}\frac{Ep^2}{Z}\frac{1}{w}\frac{df(w,q)}{dw}$$

is the energy loss function, $E_p = 28.816\left(\frac{\rho Z}{A}\right)^{1/2}$ is the nominal plasma energy in electron-volts [29], a_0 is the Bohr radius, E is the total energy of the incident particle, w the energy-loss, $q = \hbar k$ is the linear momentum transfered, Z the atomic number of the material, and finally $\frac{df(w,q)}{dw}$ the generalized oscilator strength of the material from which inelastic inverse mean free-path $\Sigma = M^{(0)}$, and electronic stopping-power $-\frac{dw}{dx} = M^{(1)}$, follows from [24, 27, 28]

$$M^{(i)}(E) = \int w^i dw \int dq \frac{d^2\Sigma}{dqdw}. \tag{80}$$

Thus we can see that through the GOS $\frac{df(w,q)}{dw}$ the DDCIS can be calculated using a two-step process consisting first of obtaining the optical limit or OOS, $\frac{df(w,0)}{dw}$, from experiment and implementing the momentum dependency analytically through a model. The model we will use is the so called δ-oscillator model, which was first presented by J. C. Ashley [30]. This δ-oscillator dispersion model connects the energy-loss function of the material with the optical energy-loss function, and hence experimental optical data, through

$$w\Im\left[-\frac{1}{\varepsilon(k,w)}\right]=\int_0^x dw'w'\Im\left[-\frac{1}{\varepsilon(0,w')}\right]\delta[w-(w'+(\hbar k)^2/2)]. \tag{81}$$

Thus relating the GOS with the OOS through

$$\frac{df(w,q)}{dw}=\frac{df(w-(\hbar k)^2/2)}{dw} \tag{82}$$

This method was first introduced by the Oak Ridge group (R. H. Richie, J, C. Ashley, and co-workers) [30].

Finally, we can write the desired single relation between the DDICS and the OOS with implemented momentum dependence through the delta-oscillator model as

$$\frac{d^2\Sigma}{dqdw}(E;w,q)=\frac{1}{2a_0Z}\frac{Ep^2}{E}\frac{1}{w}\frac{1}{q}\frac{df(w-q^2/2)}{dw} \tag{83}$$

This is the fundamental searched relation that connects the DDICS with our initial semi-empirical OOS data. From successive integrations, we can then obtain SDCS, TCS and other desired quantities necessary for the MC simulation of the secondary electron emission from the targets.

2.8 Monte Carlo simulation of radiation transport

For completeness, the end of this document provides two results of MC simulations using PARTRAC, a Monte Carlo code designed by GSF (The National Research Center for Environment and Health of Germany) [31]. They were accomplished and kindly provided by Dr. Michael Dingfelder after the inplementation of our interaction models.

2.8.1 Tracking of a charged particle

In Monte Carlo simulation, the interaction of primary charged particles with other medium, consists of random sequences of free flights, where no interaction between projectile and target takes place (original physical state of the particle is conserved), ending with the occurence of an event (some change in the previous physical state of the particle). This event is characterized by a possible loss or transfer of certain amount of energy, change in direction of movement, and can possibly cause ionizations or generation of secondary particles. For the analitical or numerical description of all this to be possible, an interaction model or a set of differential cross-sections (DCS) for each type of event under consideration needs to be implemented into the MC simulation routines. These DCSs will then serve to determine the normalized probability distribution functions (PDF) of the random variables needed to describe a "track." With appropriate inverse methods, the fundamental equation involving the corresponding cummulative distribution functions (CDF) and a random number $\xi = [0,1[$, $cdf(\psi) = \int_a^{\psi} pdf(x)dx = \xi$, can be written as a relation between the desired random variable ψ and ξ, $\psi = f(\xi)$. Finally, histories can be generated by sampling methods and quantitative information is obtained by averaging them over many calculations. Following is a more detail explanation of this process.

2.8.2 The probability distribution function and sampling methods

As previously said, to describe the physical state (its energy and momentum for example) of a particle as it travels or interacts with some target material, we need the relevant random variables. These are obtained from random sampling their respective probability distribution function (PDFs). In general, this is accomplished with the use of random generators that produce uniform distributed random numbers $\xi \in [0,1[$. The desired random variables x are then obtained by solving the following sampling equation, involving the cumulative distribution function on the left and uniform random variable on the right, for x using inverse transform methods [32, 33]

$$\int_{x_{min}}^{x} p(x')dx' = \xi, \tag{84}$$

where $p(x)$ is the probability distribution function of x and ξ are random numbers.

Now, letting the particle's direction be defined by the polar and azimuthal angles θ and ϕ, the energy-loss per event by w, and assuming that the particle could possibly interact with the target through one out-of-two exclusive possible scattering methods A or B, the scattering model for each kind of collision can be written as

$$\frac{d^2\sigma_A(E;w,\theta)}{dwd\Omega}$$

and

$$\frac{d^2\sigma_B(E;w,\theta)}{dwd\Omega},$$

respectively for collisions or interactions types A and B, where E is the initial energy of the projectile, $d\Omega$ is a solid angle element in the direction θ, ϕ.

The total cross-sections (per target element) are

$$\sigma_{A,B}(E) = \int_0^E dw \int_0^\pi 2\pi \sin\theta d\theta \frac{d^2\sigma_{A,B}(E;w,\theta)}{dwd\Omega}. \tag{85}$$

The PDFs of the energy-loss and polar scattering angle for individual events are

$$p_{A,B}(E;w,\theta) = \frac{2\pi\sin\theta}{\sigma_{A,B}(E)} d\theta \frac{d^2\sigma_{A,B}(E;w,\theta)}{dwd\Omega}, \tag{86}$$

where $p_{A,B}(E;w\theta)dwd\theta$ gives the normalized probability that, in a scattering event of type A or B, the particle loses energy in the interval $(w, w+dw)$ and suffers deflection into the solid angle $d\Omega$ in the direction θ, ϕ, relative to the initial direction. For an azimuthal symmetric system, the azimuthal scattering angle per collision is uniformly distributed within the interval $(0, 2\pi)$ with probability distribution function

$$p(\phi) = \frac{1}{2\pi}. \tag{87}$$

Finally, the probability distribution for the discrete random variable that defines the kind of interaction in a single event can be written as

$$p_A = \frac{\sigma_A}{\sigma_T} \tag{88}$$

and

$$p_B = \frac{\sigma_B}{\sigma_T}, \tag{89}$$

where $\sigma_T = \sigma_A + \sigma_B$ is the total interaction cross section.

2.8.3 Random track generation

Now, with the necessary probability distribution functions (PDFs) and a random generator suplying random numbers uniformly distributes in the interval $\xi \in [0,1[$ at hand, a random track is simulated as follows:

The length between events, where the particle moves freely without interacting with the medium (free-path), the type of event (scattering mechanism) that will take place, the change in direction, and the energy-loss in the event are all random variables that are sampled from their corresponding PDFs. The position of next event can be written as

$$\vec{r}_{n+1} = \vec{r}_n + \alpha\hat{d}, \tag{90}$$

where α is the random variable sampled from the free-path PDF, $r = (x, y, z)$, is the position vector of an event in the medium, and $\hat{d} = (u, v, w)$ is the direction cosines of the direction of flight. The energy-loss w and the polar scattering angle θ are sampled from the distribution $p_{A,B}(E; w, \theta)$ with a suitable sampling technique and the azimuthal angle is generated from a uniform distribution in the interval $(0, 2\pi)$ as

$$\phi = 2\pi\xi. \tag{91}$$

2.8.4 An example using a hypothetical mean-free-path PDF

Let a statistical model or PDF for the mean-free-path of certain particle be represented by the following exponential function

$$pdf(x) = e^{-x}. \tag{92}$$

Noting that this function is already normalized,

$$\int_0^\infty e^{-x} dx = 1, \tag{93}$$

we can obtain the CDF and its relation with $\xi = [0, 1[$ from

$$f(\lambda) = \int_0^\lambda e^{-x} dx = 1 - e^{-\lambda} = \xi. \tag{94}$$

This results in a implicit relation involving our desired random variable λ and a set of random numbers ξ. By inverse methods we finally obtain the explicit relation that can be written as

$$\lambda(\xi) = -\ln(1-\xi), \tag{95}$$

from which we can sample the mean-free-path of the particle λ from an uniform random distribution $\xi = [0,1[$ given by an random generator. Following, please see figure 5, is the graphical representations of the mean-free-path random distribution after 10000 runs of the random generator using our hypothetical exponential pdf.

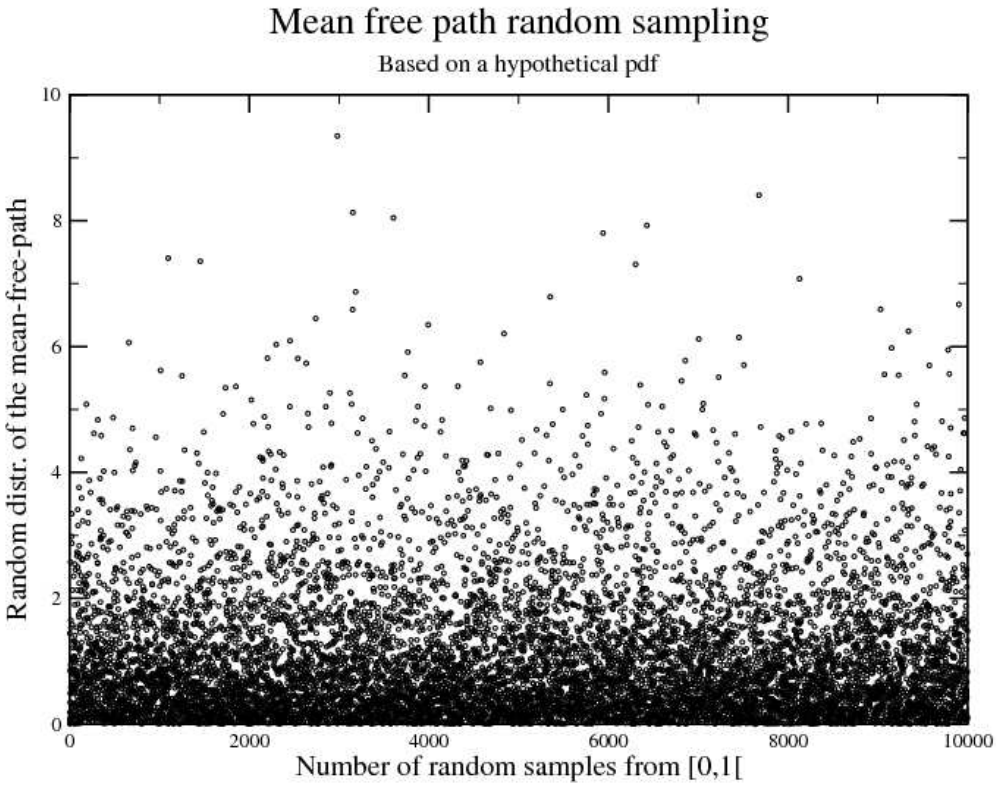

Figure 5: Graphical representation of the mean-free-path from a hypothetical PDF. Each point represents a possible value for the mean-free-path that is obtained from equation 95. The graph shows 10,000 points or runs of the random generator. The final result is taken as an average over them.

A full explanation of this process can be found in [31, 32, 33].

3 Procedures

3.1 Consistency test for the OOS - sum-rule test

Our starting point is the verification of of Bethe's sum-rule of the initially available semi-empirical optical-oscillator-strength-data of aluminum, copper, and gold defined as [14, 15]

$$\int_0^\infty \frac{df(w,q=0)}{dw} dw = Z, \tag{96}$$

where $\frac{df(w,0)}{dw}$ is the OOS, w is the energy-loss grid, q is the linear momentum transfer, and Z the number of electrons per atom in the material.

Since the OOS is constructed in part from experiment [25], where index of refraction and extinction coefficients are used to construct the dielectric function and the energy loss function of the medium under consideration, please see section (G) of this document, and in part with a extrapolation-scheme for the higher-energy shells, this test verifies if any normalization factor needs to be applied to the data.

The numerical integration of the OOS is also a good point to verify and optimize the numerical inrtegration routines. The optimization of the energy loss step size dw for the numerical integration in the energy loss domain w was accoplished by force where direct integration of the OOS as function of step size was done and compared with an approximately three percent allowed error band with respect to the optimum total number of atomic electrons that have the well known values of 13, 29, and 79,

respectively for aluminum, copper, and gold. It was found that the best results were obtained by first dividing the OOS into three regions with distinct energy loss steps where $dw1$ and $dw3$ values were maintained constant at $dw1 = 1.00 \times 10^{-5}$ Hartrees or 2.72×10^{-4} eV for $w < 4.00$ Hartrees or 108.8 eV, and $dw3 = 1.00 \times 10^{1}$ Hartree or 272 eV for $w > 3.50 \times 10^{2}$ Hartree or 9.52 keV. By varing the energy loss step size $dw2$ of the second interval in the energy loss domain, where $4.00 < w < 3.50 \times 10^{2}$ Hartrees, the OOS integration could be optimized. The optimum value of $dw2$ was found to be 1.00×10^{-2} Hartrees or 0.272 eV, please see figure 6. Following are also given the graphical representations of the OOS for all three materials. Please, see figures 7 through 9.

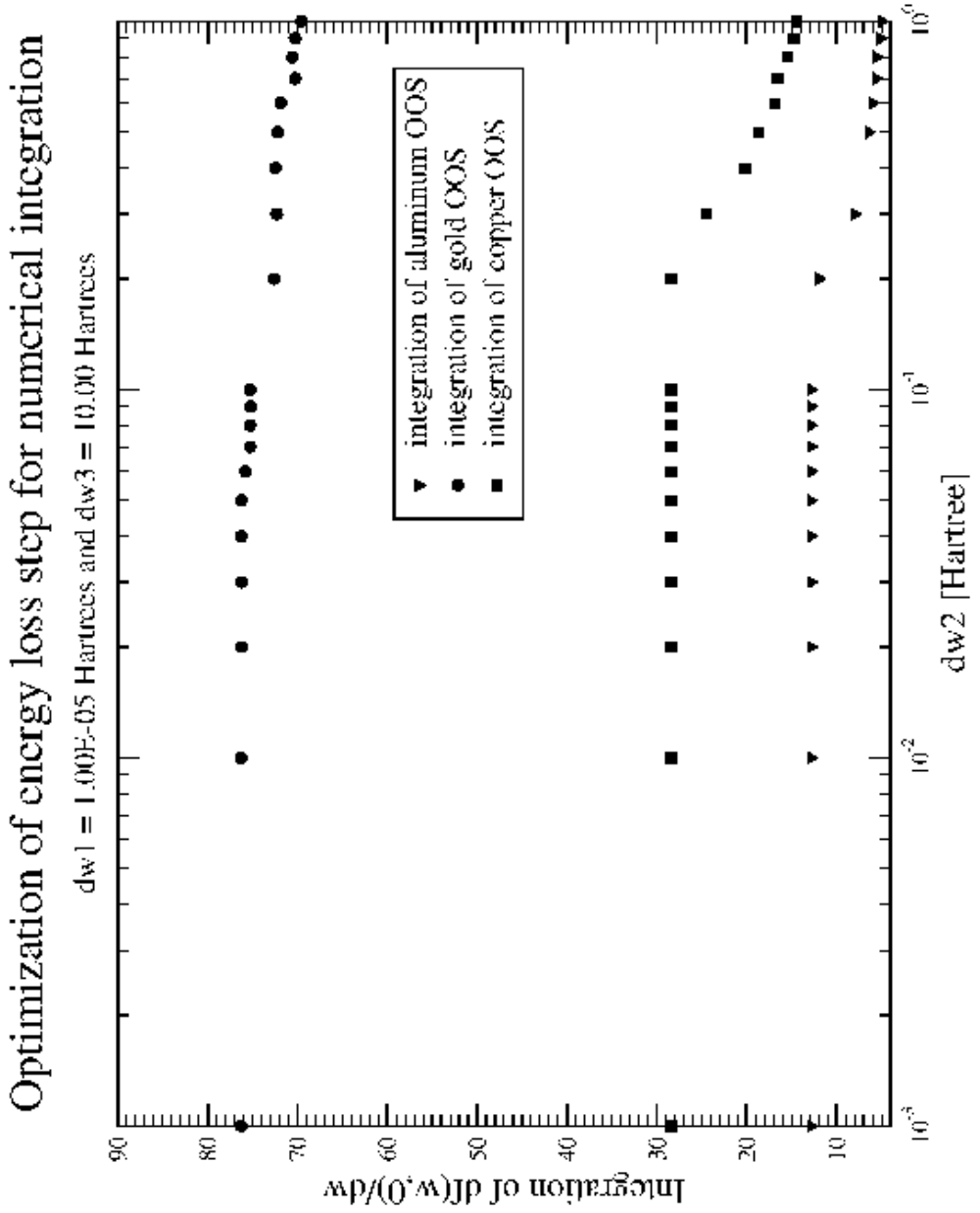

Figure 6: Analysis of the integration routine used in the integration of the OOS. The integration results is shown as function of the energy-loss step $dw2$. The optimum results are values that stay within approximately 3 percent of the total number of electrons por atom of the target material (Aluminum Z = 13, copper Z = 29, and gold Z = 79).

3.1.1 Aluminum OOS

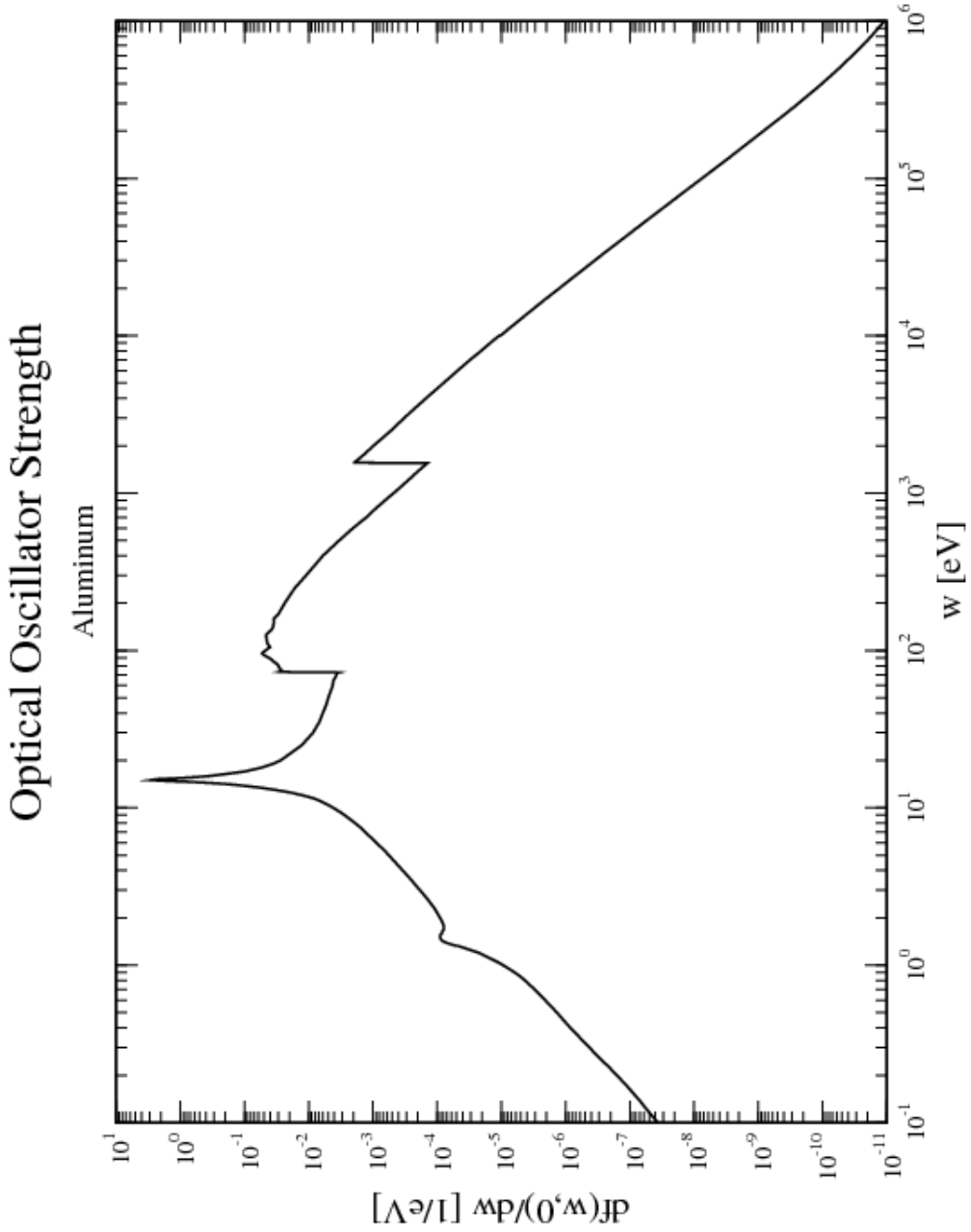

Figure 7: Optical oscillator strength density distribution of aluminum (Z = 13). Obtained partially from experimental data [25] and partially from NIST [26] for $w > 1.0$ keV.

3.1.2 Copper OOS

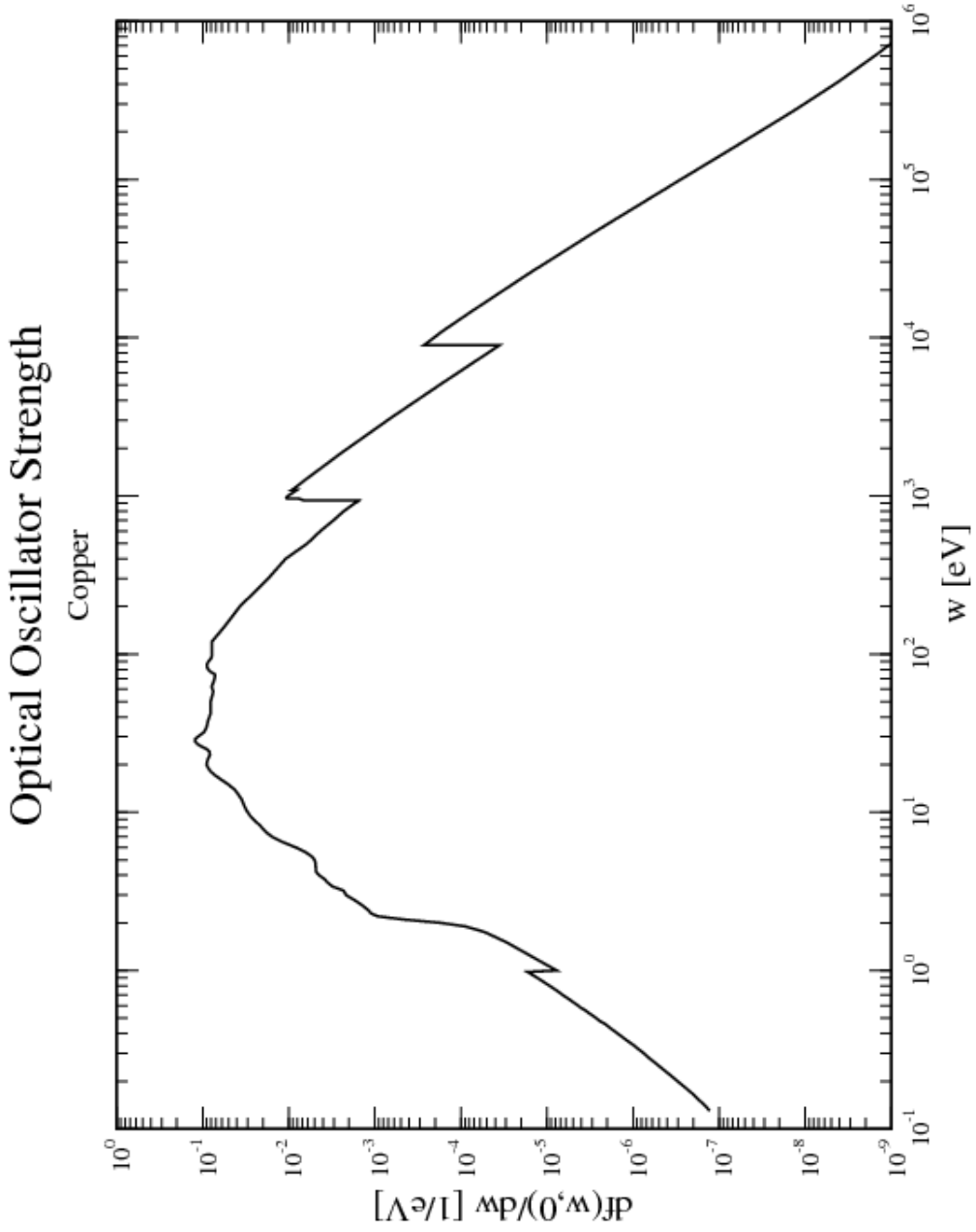

Figure 8: Optical oscillator strength density distribution of copper (Z = 29). Obtained partially from experimental data [25] and partially from NIST [26] for $w > 1.0$ keV.

3.1.3 Gold OOS

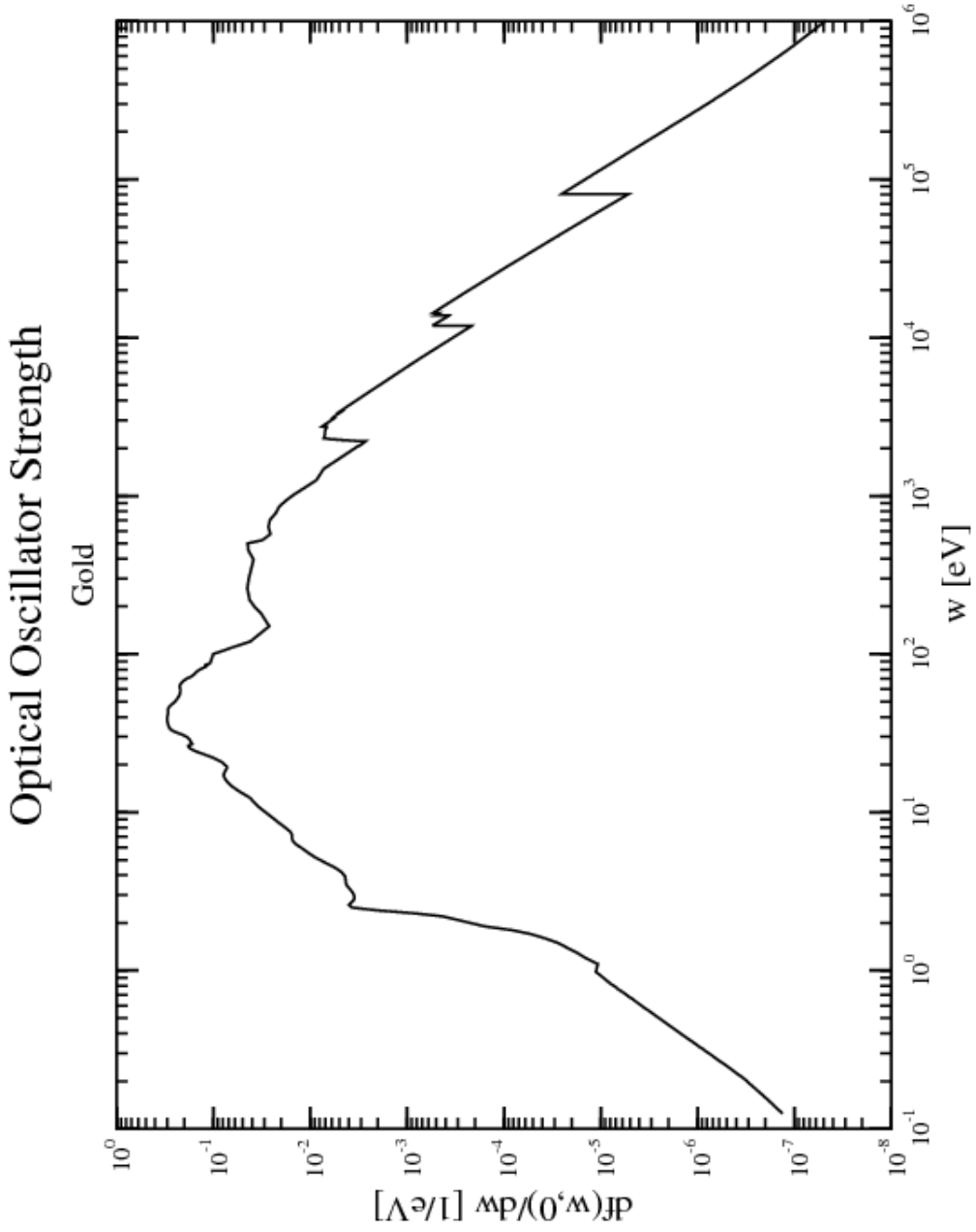

Figure 9: Optical oscillator strength density distribution of gold (Z = 79).

Obtained partially from experimental data [25] and partially from NIST [26] for $w > 1.0$ keV.

3.2 Limits of integration

From the kinematics of the collision we can define the following interval of integration for the momentum space (q_{min}, q_{max}). Recalling the relations between linear momentum and the energy of the incident particle we can write

$$q_{init} = \sqrt{2mE} \tag{97}$$

where: q_{init} is the initial linear momentum magnitude of the incident particle, E the incident particle's total kinetic energy, and m its mass.

Now, for a possible loss of energy w during the collision with a target, it is clear that the incident particle's magnitude of linear momentum can assume values from a minimum of

$$q_{min} = q_{init} - q' = \sqrt{2m}(\sqrt{E} - \sqrt{(E-w)}) \tag{98}$$

to a maximum of

$$q_{max} = q_{init} + q' = \sqrt{2m}(\sqrt{E} + \sqrt{(E-w)}) \tag{99}$$

where: $q' = \sqrt{2m(E-w)}$.

Following are graphical representations of these limits as function of energy-loss for electrons at 10 eV and 1 keV, and proton sources at 100 eV, and 1 MeV, please see figures 10 through 13.

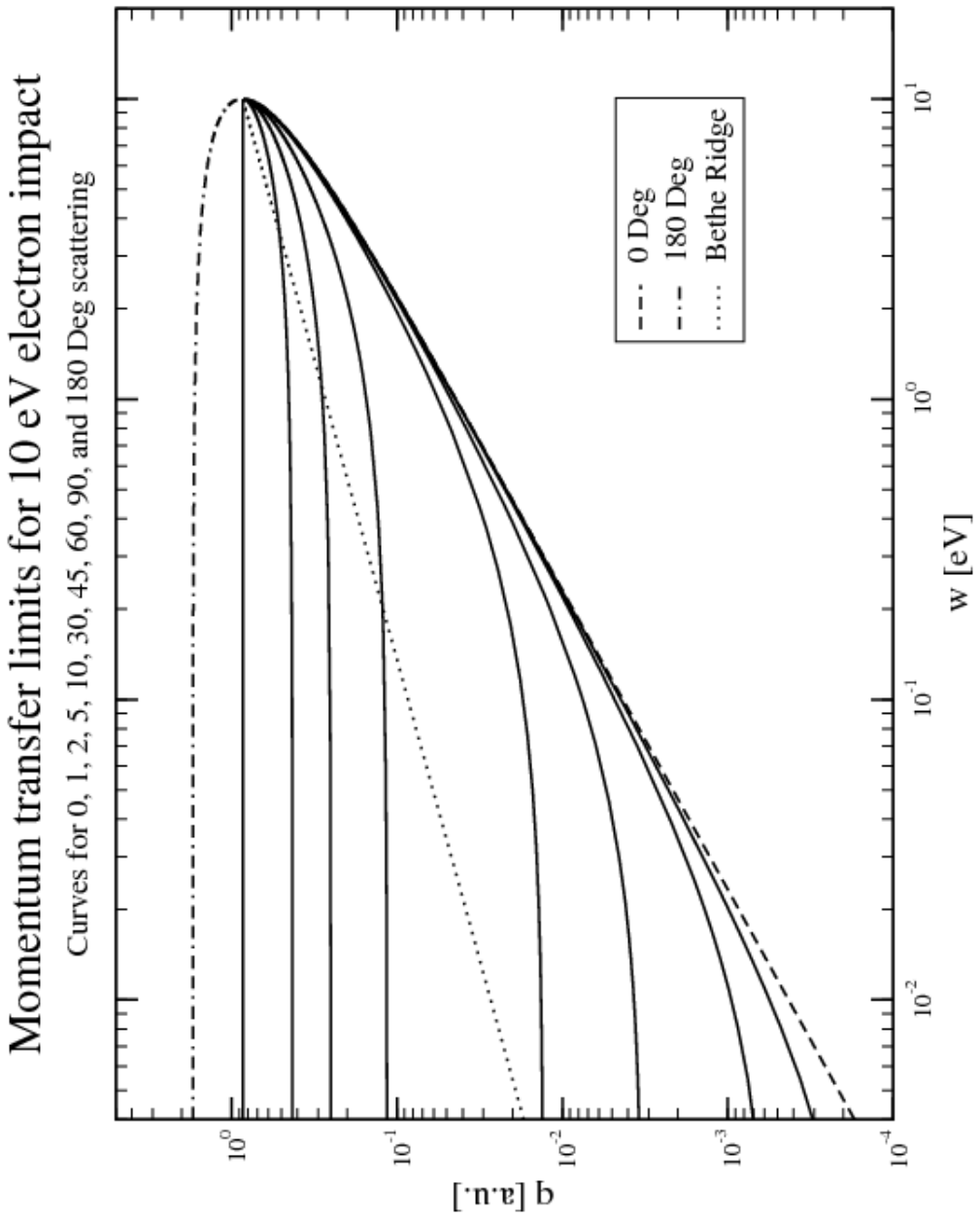

Figure 10: Limits of integration for electron energy of 10 eV

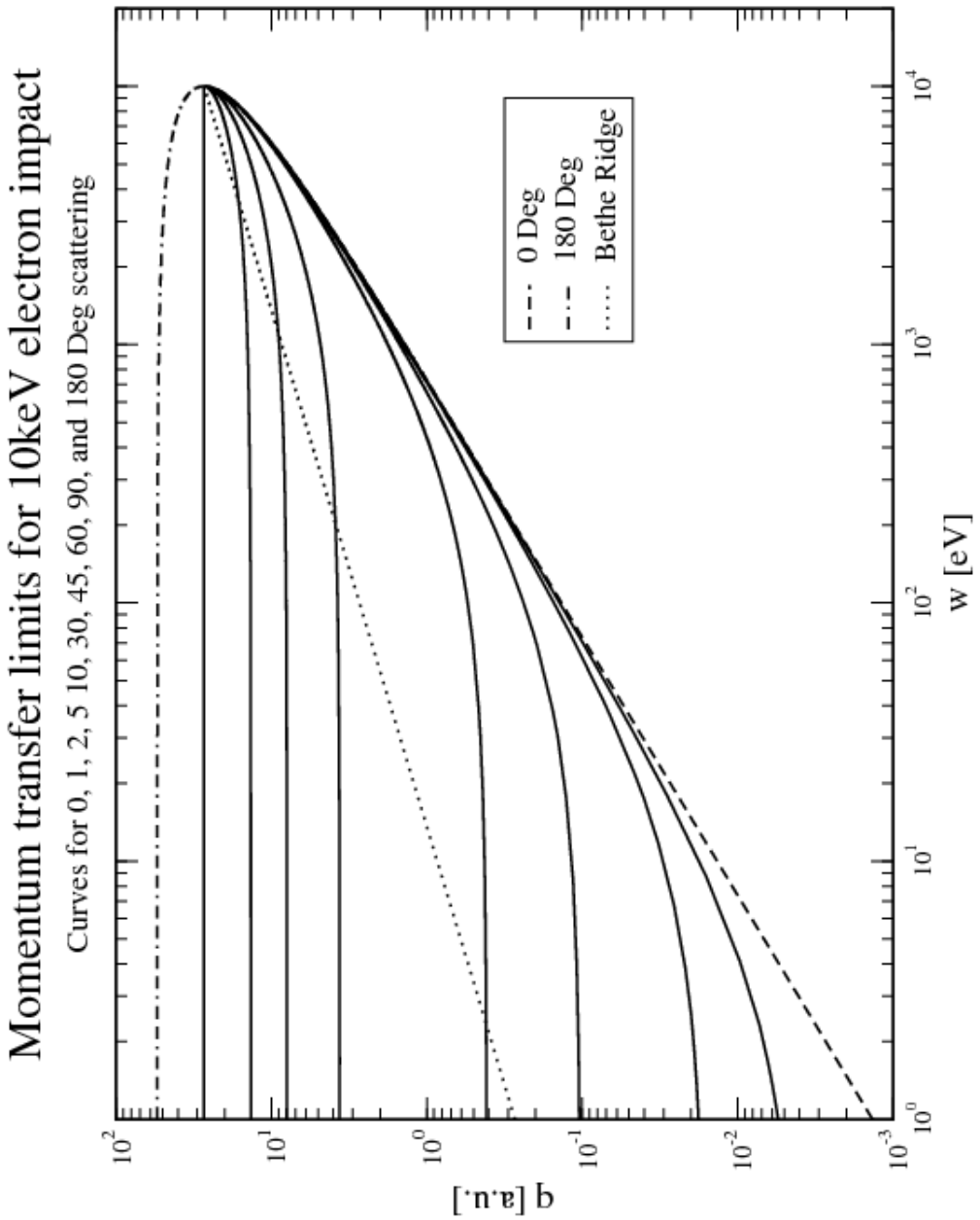

Figure 11: Limits of integration for electron energy 10 keV

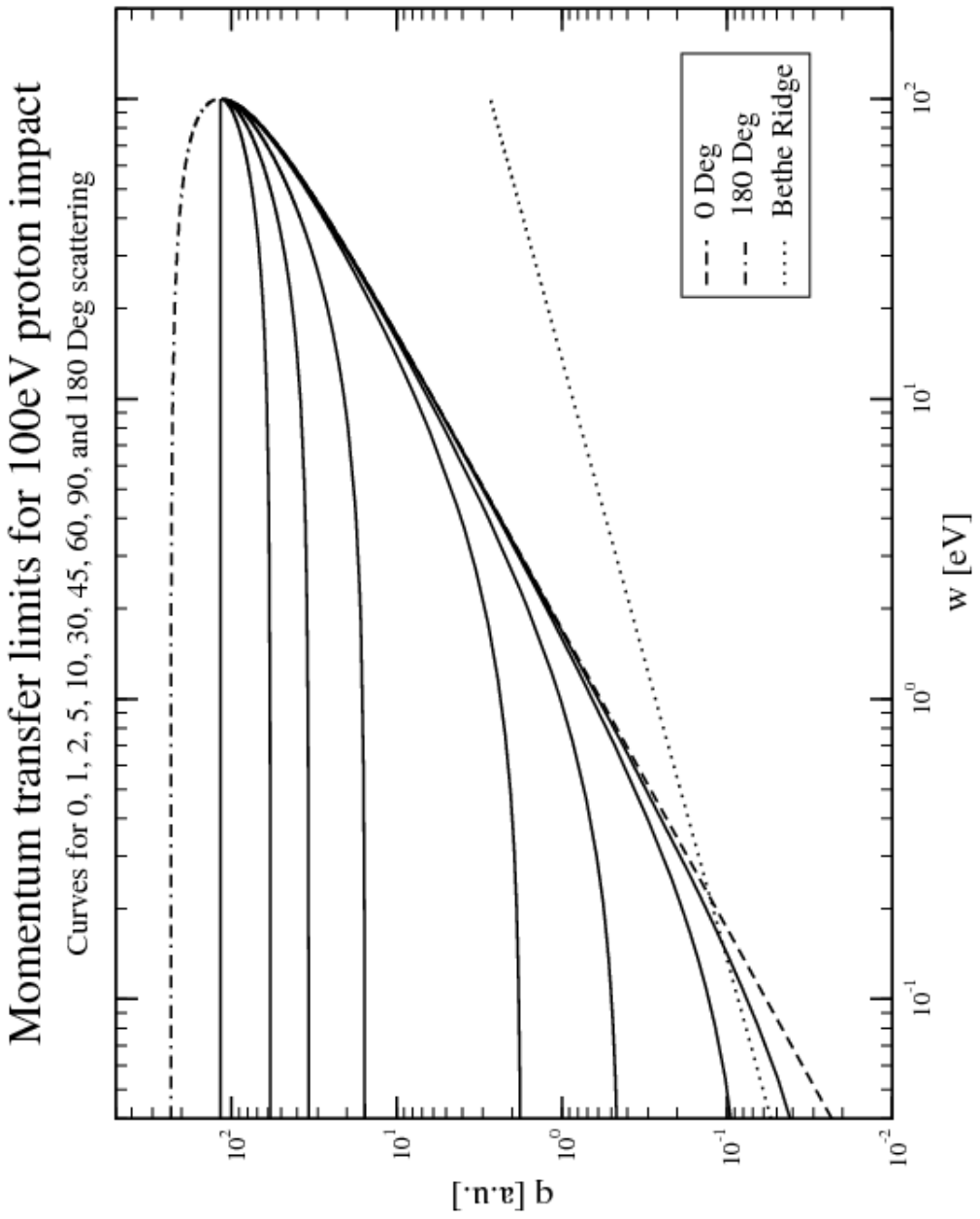

Figure 12: Limits of integration for proton energy of 100 eV

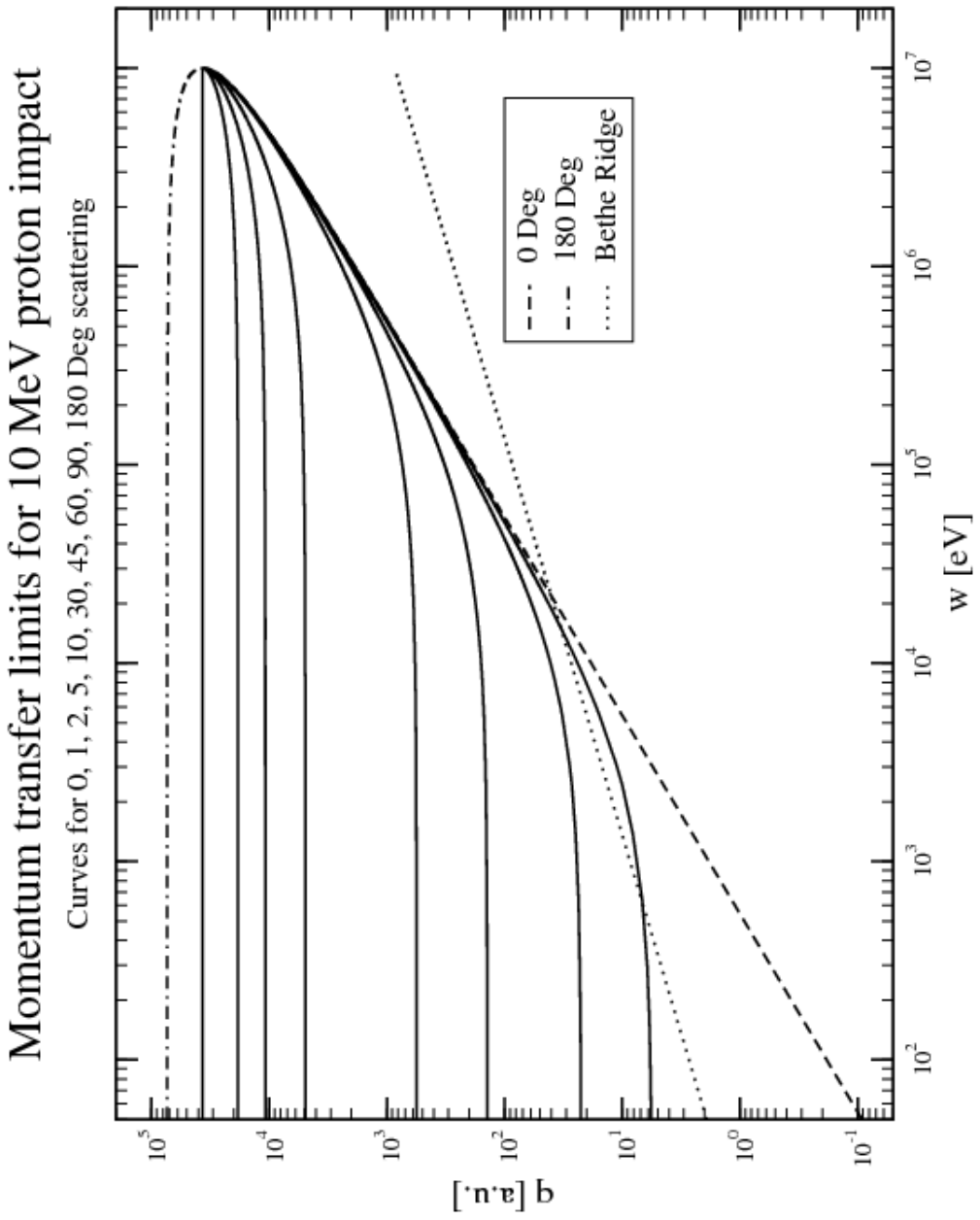

Figure 13: Limits of integration for proton energy of 10 MeV

As expected for the convergence of the integral over linear momentum, see next paragraph for the calculation of the differential inverse-mean-free-path, the limits converge to the single value $q_{min} = q_{max} = \sqrt{2mE}$ as $w \to E$.

Therefore, the first integration of equation 83 defines our first important relation. The single differential macroscopic cross-section or the differential inverse-mean free-path (DIMFP) can then be written as

$$\frac{d\Sigma}{dw}(E;w,q) = \frac{1}{2a_0 Z}\frac{Ep^2}{E}\frac{1}{w}\int_{q_{min}}^{q_{max}}\frac{1}{q}\frac{df(w-q^2/2)}{dw}dq \tag{100}$$

or more conveniently

$$\frac{d\Sigma}{dw}(E;w,q) = \frac{1}{2a_0 Z}\frac{Ep^2}{E}\frac{1}{w}\int_{\rho_1}^{\rho_2}\frac{df(w-q^2/2)}{dw}d\rho \tag{101}$$

where: ρ, ρ_1,and ρ_2 are respectively $\ln q$, $\ln q_{min}$, and $\ln q_{max}$.

Finally, a second integration over the energy-loss limits defines the other necessary quantity for the construction of the probability distribution functions for the MC simulation of the interaction. The inverse-mean-free-path (IMFP) can then be written as

$$\Sigma(E) = \frac{1}{2a_0 Z}\frac{Ep^2}{E}\int_0^w\frac{1}{w}dw\int_{q_{min}}^{q_{max}}\frac{1}{q}\frac{df(w-q^2/2)}{dw}dq \tag{102}$$

Note that the IMFP $\Sigma(E)$ or macroscopic total cross section is related to the microscopic total cross-section $\sigma(E)$ through the simple relation $\Sigma(E) = N\sigma(E)$, where N is the number density of the target.

3.3 Shell separation

So far, the calculation of the differential and total cross-sections using the total OOS as described in figures 7 through 9 respectively for aluminum, copper, and gold returns the necessary quantities for the MC simulation without providing information about the initial energy of ejection of the secondary particles in the case of ionization events. Similar to the case where the tracking of the primary particles is only possible if we know, during all the simulation time, the energy and direction of these particles, to "track" possible secondary electrons, we also need to know their initial energies and ejection angle distributions.

To fulfill this requirement, the oscillator strength distributions were separated into shells from where coefficients of proportionality could be introduced and calculated based on the complete oscillator distribution and sum rules. Following, please see figures 14 through 16, are the oscillator strength of aluminum, copper, and gold with their corresponding distribution of oscillators per shell.

Following are also given the edge energies or threshold energies for the corresponding shells, which were selected to distinct one shell from another. Please note, especially in the case of gold, that the nomenclature used for the shells do not correspond to the standard classification. This was due to difficulties encountered to distinct the subshells. Where we say K, L, M, N, O, and P -shells, in the case of gold, some are actually sub-shells named L1, L2, and L3 and so on. For our purposes, what is important for this simulation is to know where the distinctions are made by their corresponding edge-energies. Specially between what is consider inner and outer-shells.

3.3.1 Aluminum edge-energies

- L-edge $w > 74$ eV
- K-edge $w > 8.979$ eV

3.3.2 Copper edge-energies

- L-edge $w > 950$ eV
- K-edge $w > 9.979$ keV

3.3.3 Gold edge-energies

- O-edge $w > 150$ eV
- N-edge $w > 2.21$keV
- M-edge $w > 11.92$ keV
- L-edge $w > 13.70$ keV
- K-edge $w > 80.72$ keV

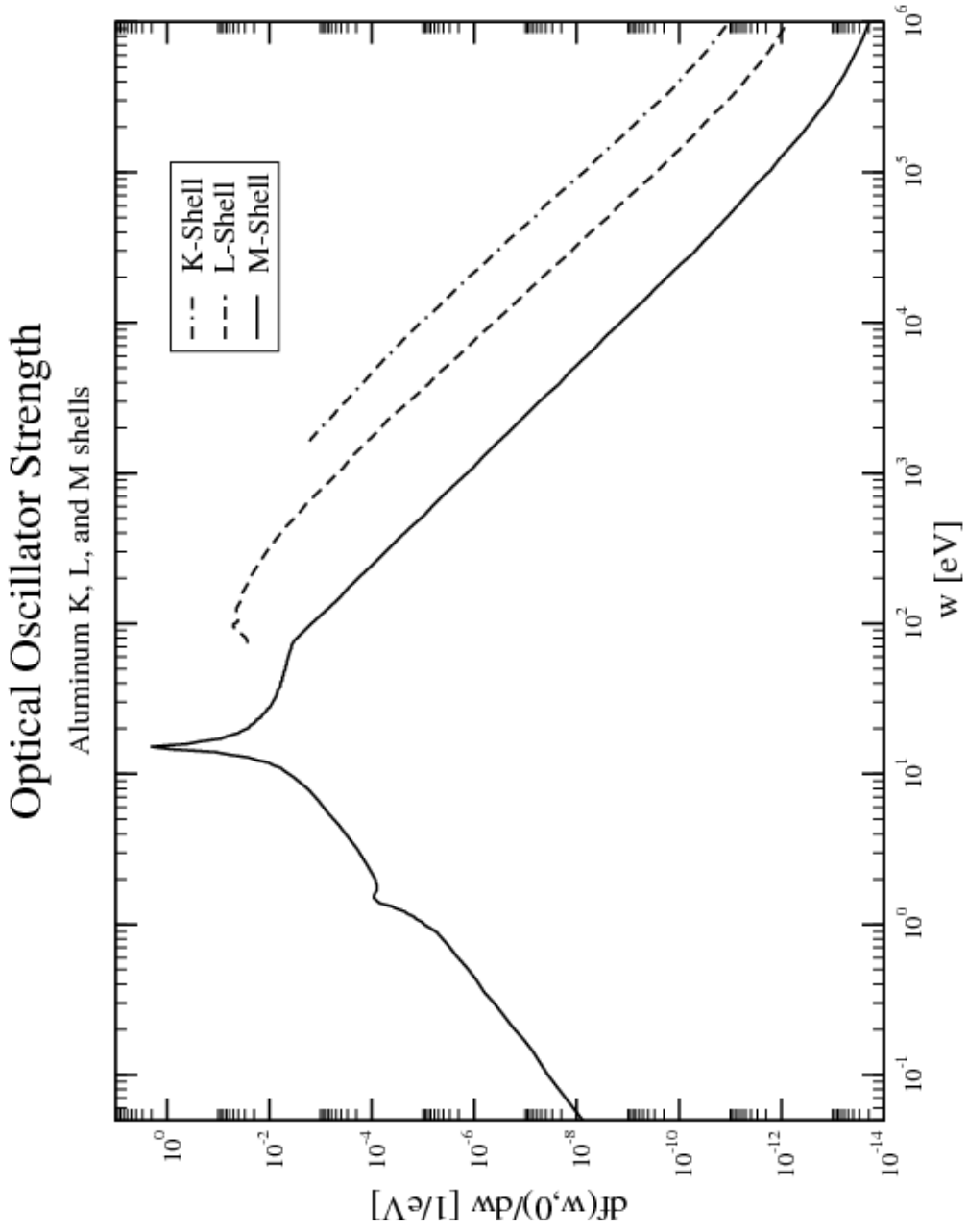

Figure 14: Aluminum OOS K, L, and M shell separation

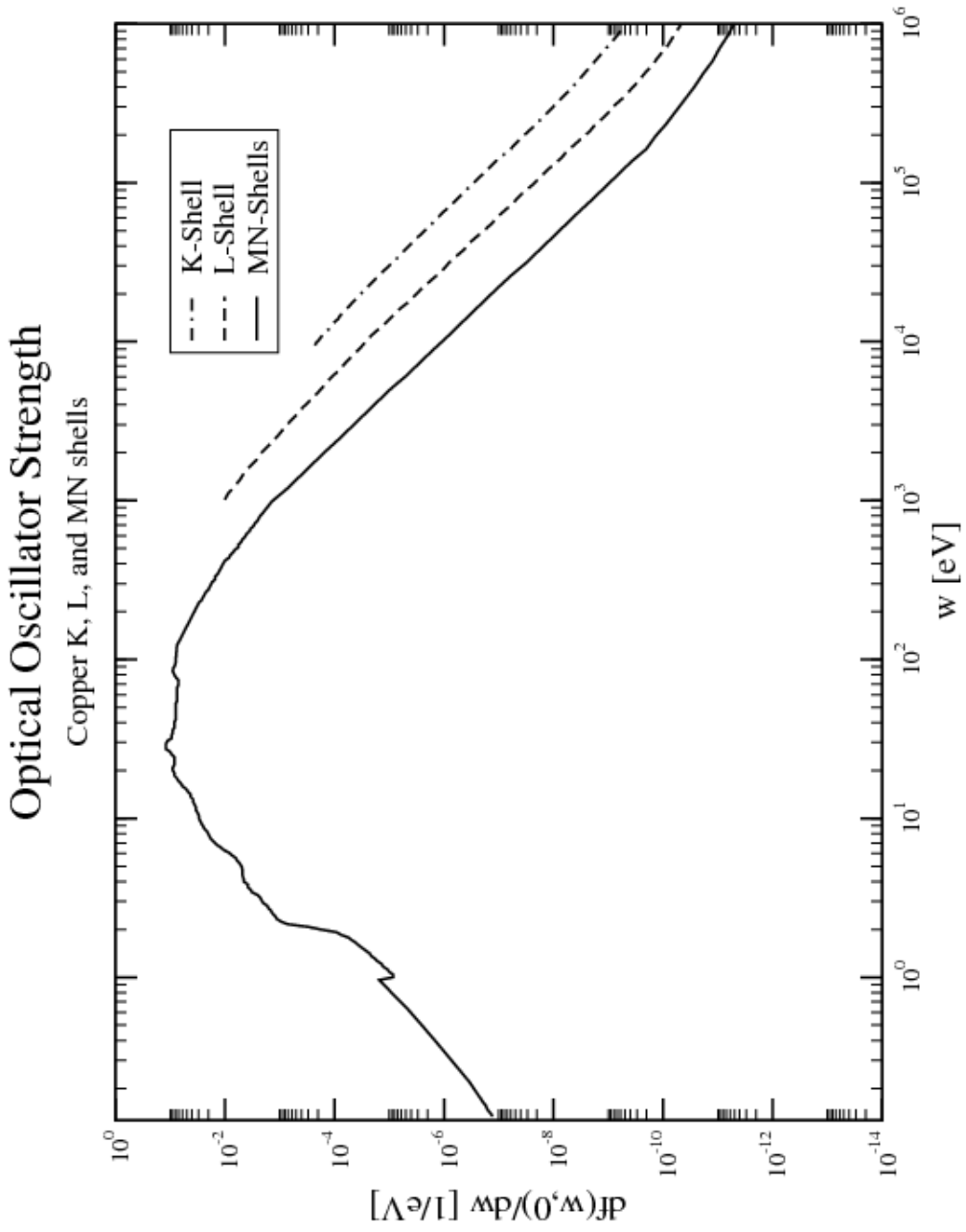

Figure 15: Copper OOS K, L, and MN shell separation

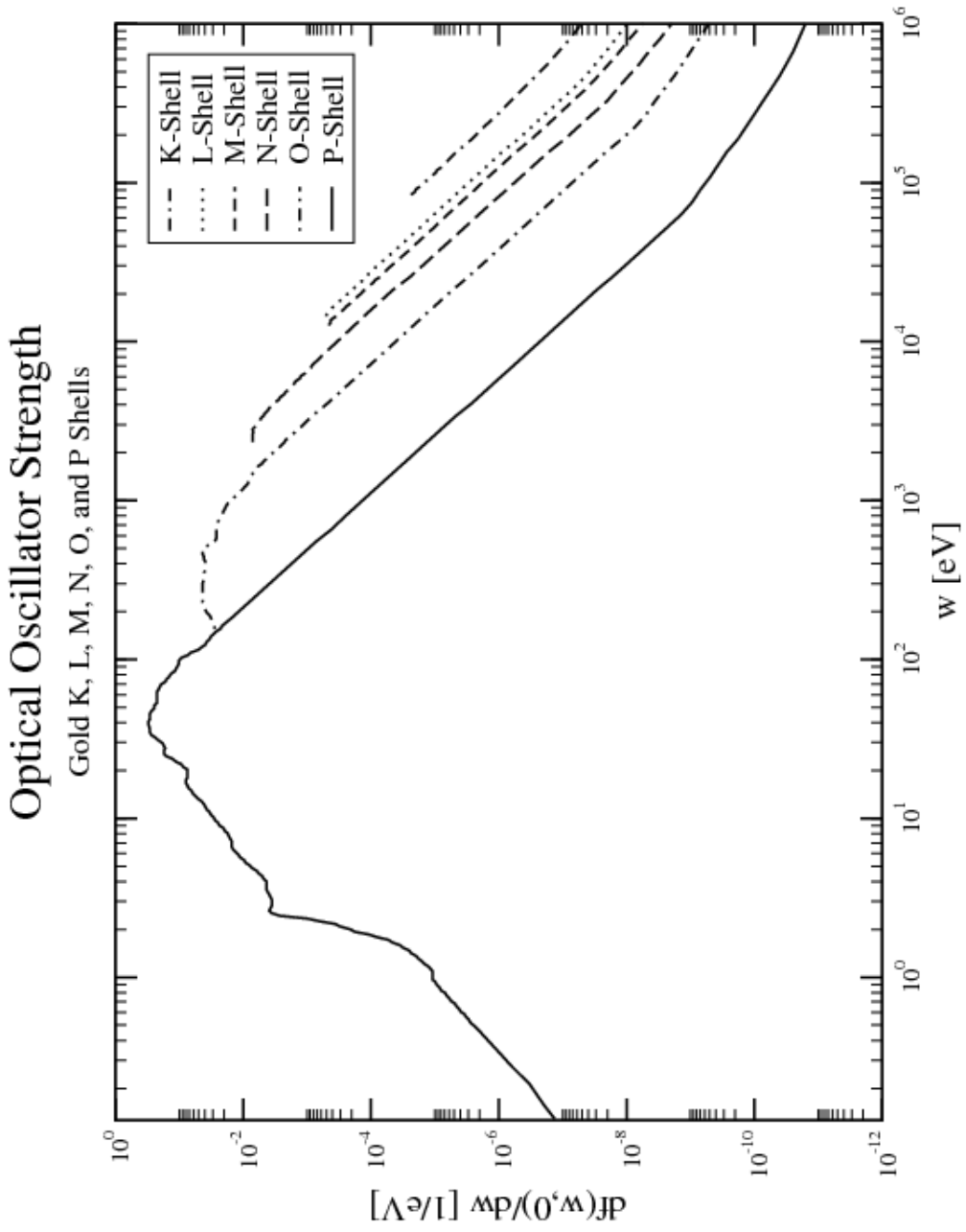

Figure 16: Gold OOS K, L, M, N, O, and P shell separation

The construction of the shell-coefficients was done in a three step process as follows:

First, a particular shell and its spectrum of participation is identified. In the case of the aluminum K-shell, its participation starts at $w > 8.979$ eV , as indicated above. Second, if other shells overlap in the same energy range, the OOS of the considered shell is appropriately subtracted from the OOS of these overlaping shells. Finally, normalization is obtained by dividing the resulting shell-OOS by the total OOS in the considered spectrum. The result is a coefficient that ranges from 0 to 1 that indicates how strong is the participation of a certain OOS-shell in a particular spectrum. Again using the aluminum K-shell OOS as an example, we can see that its corresponding coefficient should be 0 for $w < 8.979$eV, and assume a value $0 < C_k < 1$ for $w > 8.979$eV. Please, refer to figures 17 through 19 for the complete values of the shell-coefficients for aluminum, copper, and gold.

The differential and total cross-sections can then be obtained by multiplying these coefficients by the previously calculated differential and total cross-sections using the complete oscillator strength distributions. Again, please see figures 17 through 19, for the graphical representations of the shell-coefficients for aluminum, copper, and gold. Note that their sum at any point in the spectrum must equal to 1.

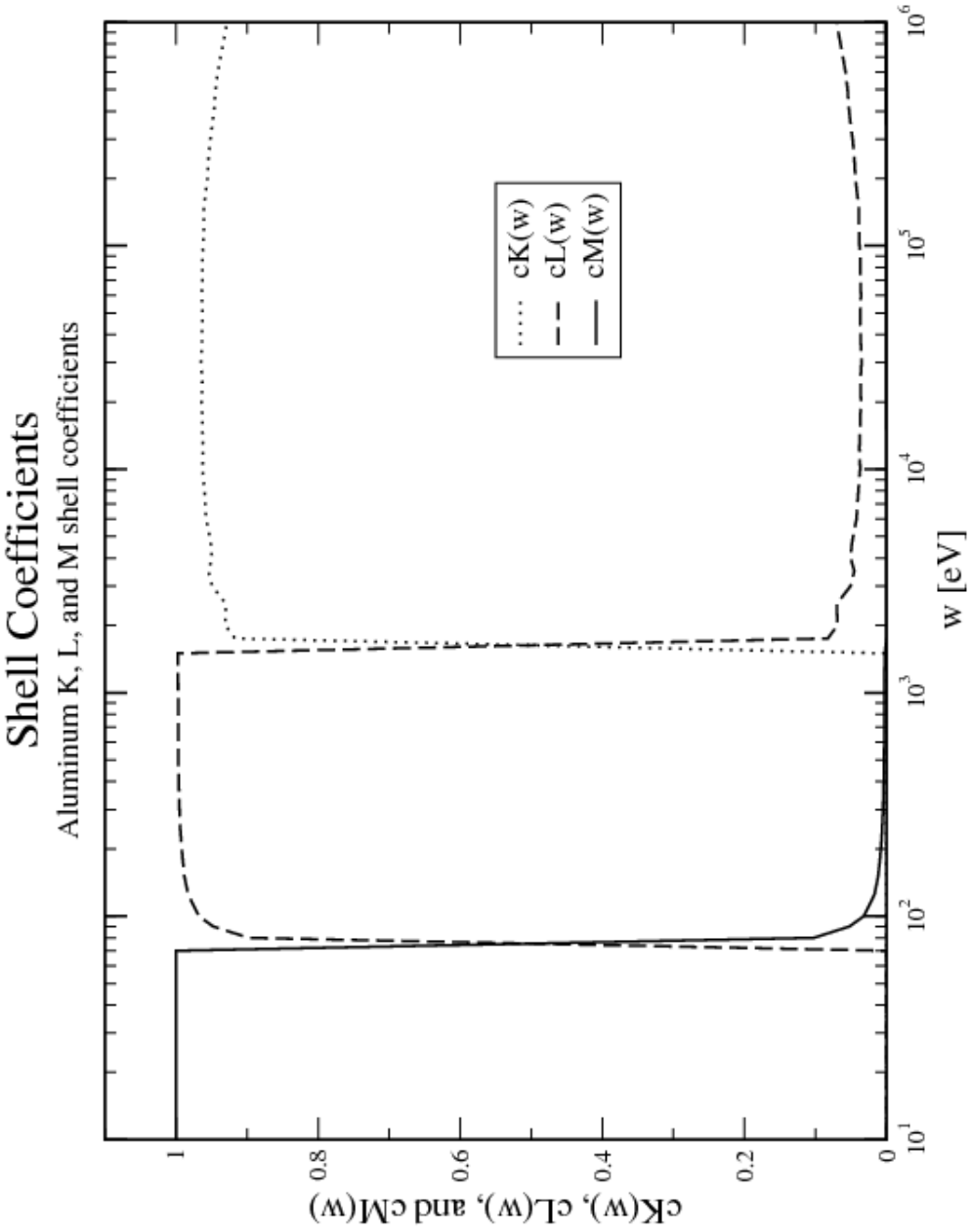

Figure 17: Aluminum shell coefficients.

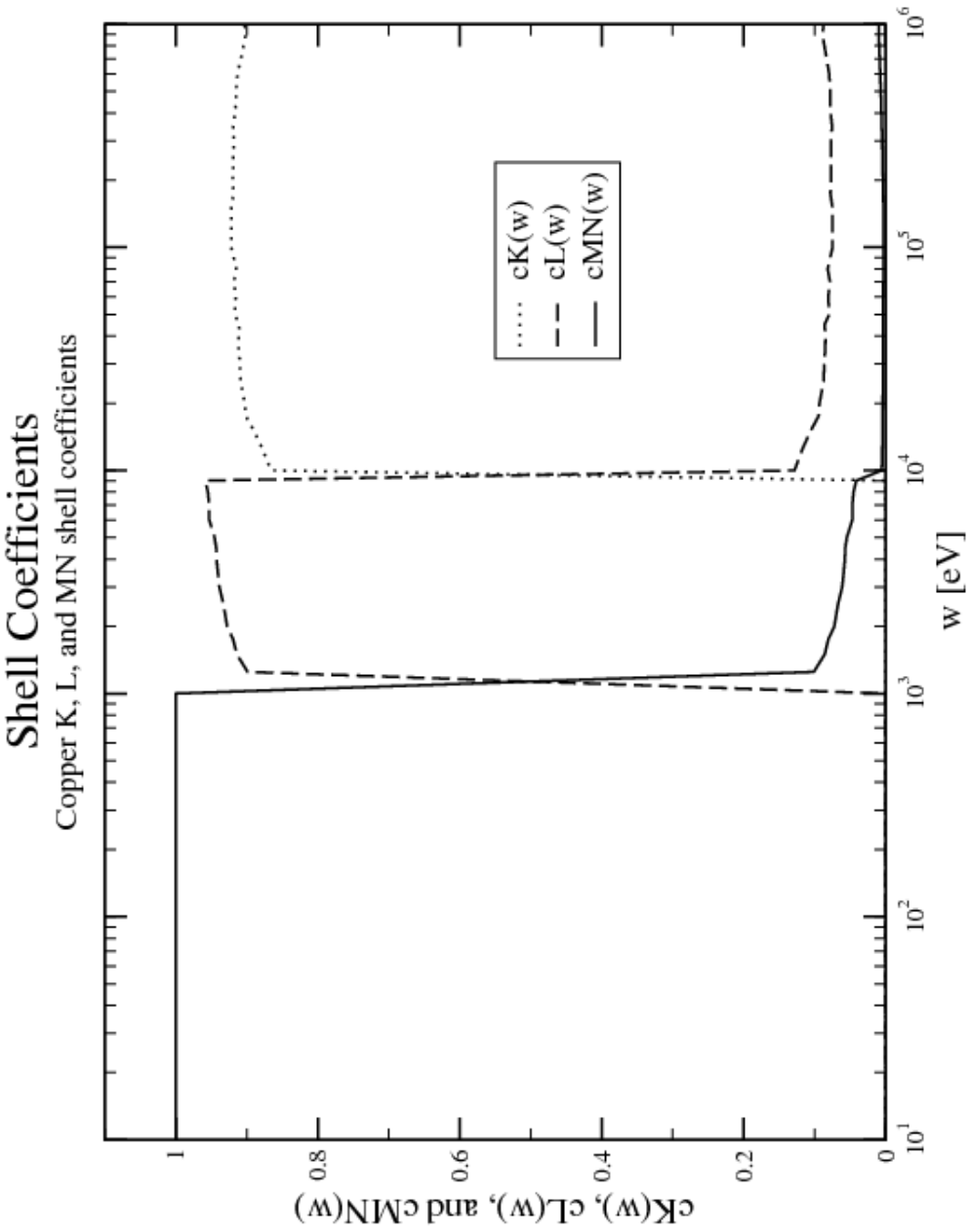

Figure 18: Cooper shell coefficients.

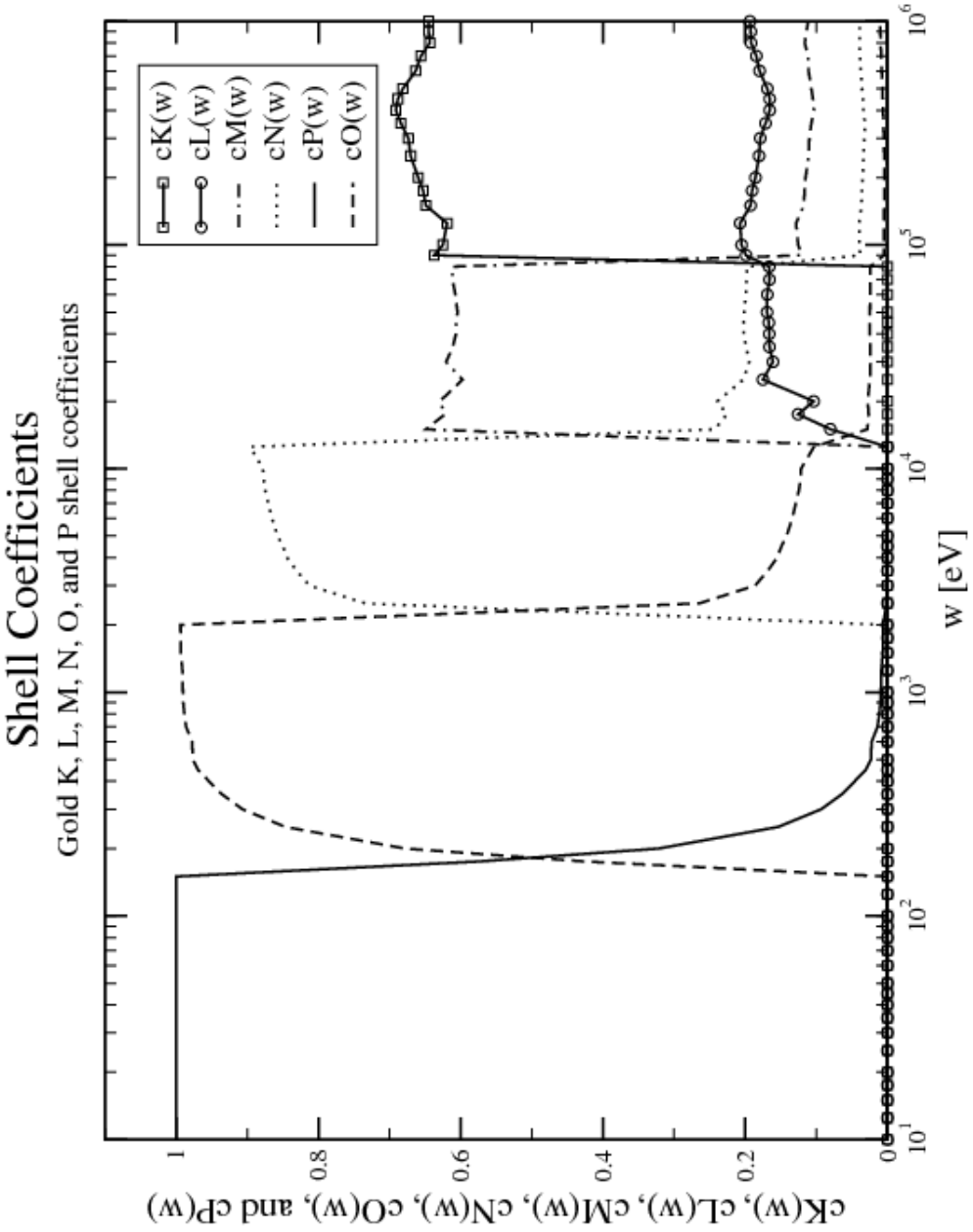

Figure 19: Gold shell coefficients.

3.4 Agular distribution of primary and secondary particles

So far, we have considered only the particle's initial energy and its mean free path for the determination of their track structure or MC simulation. To complete the modeling of the simulation of the track-structure of a primary or secondary particle, as they travel through the target foil, we also need to know the direction that they will take after an event, elastic or inelastic, takes place. More specifically, we must know their respective angular probability distribution functions from which the angular variables θ, and ϕ can be obtained by appropriate sampling methods. There are four cases to be considered:

- The angular distribution of fast proton source particles
- The angular distribution of primary electrons that can also cause further ionizations
- The angular distribution of secondary electrons induced by electron impact
- The angular distribution of secondary electron induced by proton impact

3.4.1 Angular distribution of primary protons

For the proton as primary particle, due to its overwhelmingly bigger mass with respect to the mass of the target electrons ($m_p \approx 1836\, m_e$) and with initial momentum p_i also much greater than the momentum transfer q, ($p_i \gg q$), it is then justifiable to consider that they will approximately travel in straight lines through the material from the beginning of the simulation to the end. The kinematics resulting in such approximation follows:

From classical collision theory and due the dramatic difference between the masses of the fast primary protons and the secondary electrons, we can conclude that there will be a very small transfer of energy and momentum between these particles. Applying the case of elastic maximum energy transfer, or “head-on” type of collision, to a target initially at rest, we then obtain from the ratio of the kinetic energies f_1 and f_2 as follows:

$$f_1 = \frac{K_{1f}}{K_{1i}} = \left(\frac{m_1 - m_2}{m_1 + m_2}\right)^2 \tag{103}$$

and

$$f_2 = \frac{K_{2f}}{K_{1i}}, \tag{104}$$

where K_{1f}, K_{1i}, K_{2f}, m_1, and m_2 are respectively the final and initial kinetic energies of the projectile, the final kinetic energy of the target, and the masses of the projectile and target.

From the conservation of energy we can write

$$f_1 + f_2 = 1, \tag{105}$$

which results in

$$f_2 = 1 - f_1 = \frac{4m_1m_2}{(m_1 + m_2)^2}. \tag{106}$$

Therefore, a maximum energy tranfer of

$$K_{2f} = \frac{4m_1m_2}{(m_1 + m_2)^2} K_{1i}, \tag{107}$$

occurs from which we can see that if $m_1 \gg m_2$, $K_{2f} \simeq \frac{4m_2K_{1i}}{m_1} \ll K_{1i}$.

This lead us to consider for the simulation that the primary fast protons will travel through the material without being deflected by the target electrons.

3.4.2 Angular distribution of primary electrons

In the case of primary electrons, the interaction with target electrons can be explained by using eleastic and binary knematics as follows:

Let an incident (primary) electron emerge from a proton impact with initial kinetic energy E and final energy $E - w$ respectively before and after its binary encounter with a target electron. Relatively fast but still classic impact allows us to simplify our calculations by considering the target electron to be initially at rest and to acquire an energy w after the collision. Under these approximations we can easily obtain the scattering angle of the projectile electron θ as follows. Please see figure 26.

From these known energies we can define the corresponding initial, final, and transferred momenta as

$$p_i = \sqrt{2mE} \tag{108}$$

$$p_f = \sqrt{2m(E-w)} \tag{109}$$

$$q = \sqrt{2mw} \tag{110}$$

We finally obtain the scattering angle of the incident electron, after its interaction with a target electron, that can be written as

$$\cos\theta = \frac{E - w}{\sqrt{E(E - w)}} \tag{111}$$

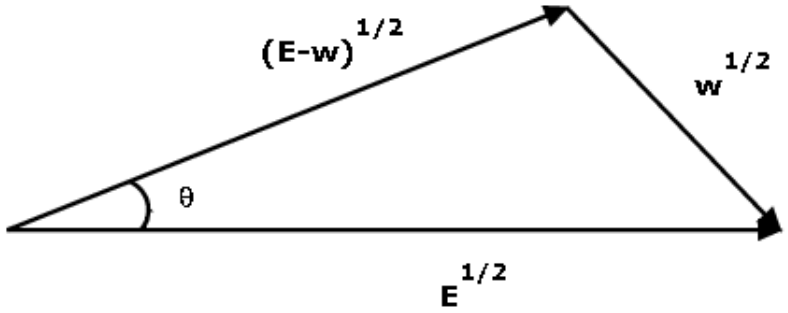

Figure 20: Classical scattering kinematics. An incident particle with initial kinetic energy E loses energy w after its collision with a free electron. The energy w that is acquired by the target. The incident particle is scattered in an angle θ with respect to its original trajectory.

3.4.3 Angular distribution of electrons induced by electron impact

In the case of electron-induced emissions, these secondary electrons will be emitted at 90^o with respect to the direction of the primary electrons. The models are based on results from experiments involving gas-phase targets and photo-ionization data.

The emission angles for these electrons, known as secondary electrons, comes from two sources:

For energy transfers $w < 100$ eV, the experimental data from Opal et al. [34, 35] were used. For energy transfers $w \geqq 100$ eV, non-relativistically, the secondary electron is emitted perpendicular to the scattered primary electron following approximately ionization by photon impact where the electrons are ejected in the direction of the perpendicular field [36, 37].

3.4.4 Angular distribution of electrons induced by proton impact

Following the steps from Dingfelder et al. in [27] and references therein, the interaction between the fast protons and the target electrons can be separated into two types - close or hard collisions and soft collisions due to dipole interactions. This involving theory is usually called the mixed binary and Bethe theory or binary encounter dipole model [38].

In summary, it implements or includes the angular dependency into the Bethe coefficients by hand that can be written as

$$A(w,\theta) = A(w).f_1(\theta) \tag{112}$$

and

$$B(w,\theta) = B(w).f_2(\theta) \tag{113}$$

The functions $f_1(\theta)$ and $f_2(\theta)$ are modelled based respectively on data from photo-electron emission and binary theory.

3.4.5 Determination of A(w) and B(w)

The proportionality between the Bethe coefficients $A(w)$ and $B(w)$, which account respectively for the “soft” and “hard” interaction terms, and the energy-loss function were used for the calculation of these coefficients. They can be written as

$$A(w) = \frac{1}{2}\eta_2(w,0) \tag{114}$$

and

$$B(w) = \frac{1}{2}\eta_2(w,0) ln \left[4(\bar{k}a_0)^2 \left(\frac{Ry}{w}\right)^2\right] + J_1 + J_2, \tag{115}$$

where the auxiliary integrals J_1 and J_2 can be written respectively as

$$J_1(w) = \int_{\overline{q}}^{\infty} \eta_2(w,q)\frac{dq}{q} \tag{116}$$

and

$$J_2(w) = \int_0^{\overline{q}} \left[\eta_2(w,q) - \eta_2(w,0)\right]\frac{dq}{q}. \tag{117}$$

In the auxiliary integrals J_1 and J_2, $\overline{q}$ is an introduced value, independent of E, that separates the high-q and low-q domains. Dingfelder et al. in [27] presents the complete derivations.

Note that, in the assymptotic region, $E \gg w$, the First Born approximation differential cross-section can be substituted by the Bethe differential cross-section, which can be written as

$$\frac{d\Sigma}{dw} = \frac{1}{\pi a_0 E}\left[A(w)\ln\left(\frac{E}{Ry}\right) + B(w) + O\left(\frac{w}{E}\right)\right], \tag{118}$$

where a_0 is the Bohr radius, w the energy-loss, E the particle's kinetic energy, Ry is the Rydenberg energy (13.6 eV). The Bethe total cross-section, after integration of equation 118, was than used to check our Bethe coefficient calculation results. Please

refer to the graphs of the total cross-sections at the end of this document where our PWFBA calculations are plotted together with the Bethe total cross-sections, which rely on $A(w)$ and $B(w)$, showing a good agreement in the high energy spectrum.

Finally, to complete the angular profile of the particles, in this case independent of the their type, the azimuthal direction is defined by the polar angle ϕ and obtained from an uniform distribution in the interval $(0, 2\pi)$ from which random sampling takes place.

Following are the calculated Bethe coefficients for aluminum, copper, and gold based on their respectively energy-loss functions as previously described by relations 114, 115, 116, and 117.

3.4.6 Aluminum, copper, and gold Bethe coefficients

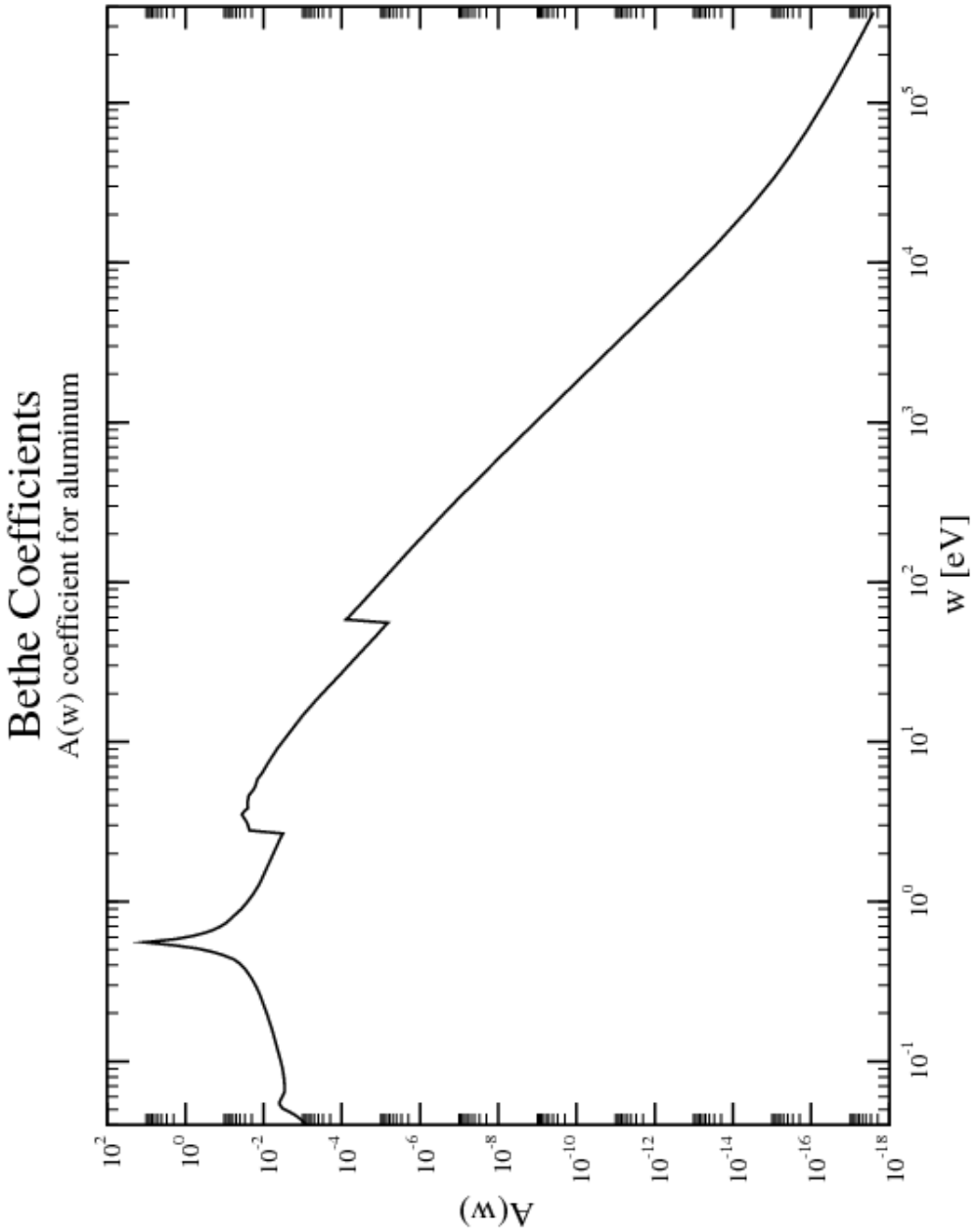

Figure 21: Bethe A coefficient, as defined in equation 114, for aluminum.

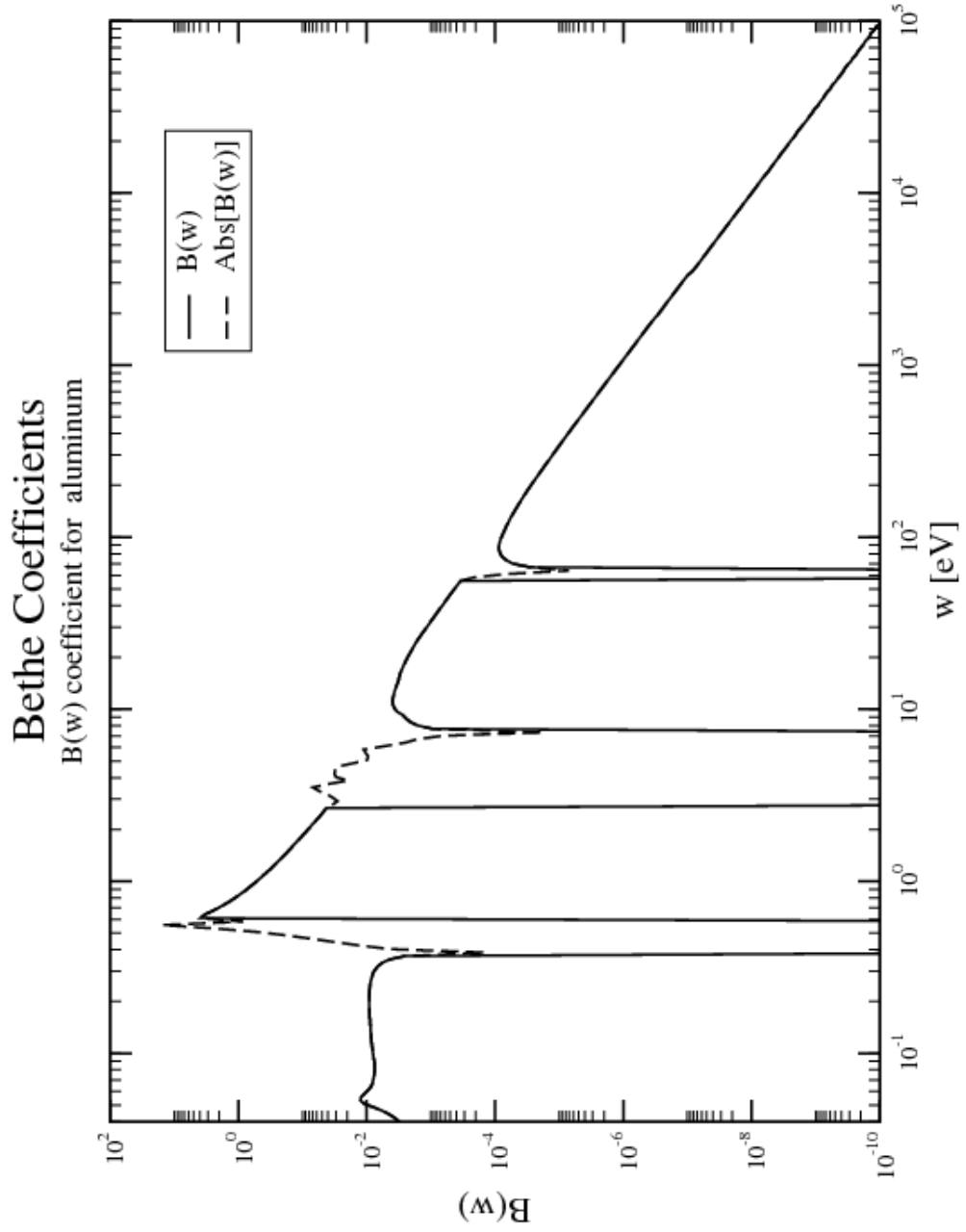

Figure 22: Bethe B coefficient, as defined in equation 115, for aluminum. The B coefficients as indicated by the dashed line are actually negative in value.

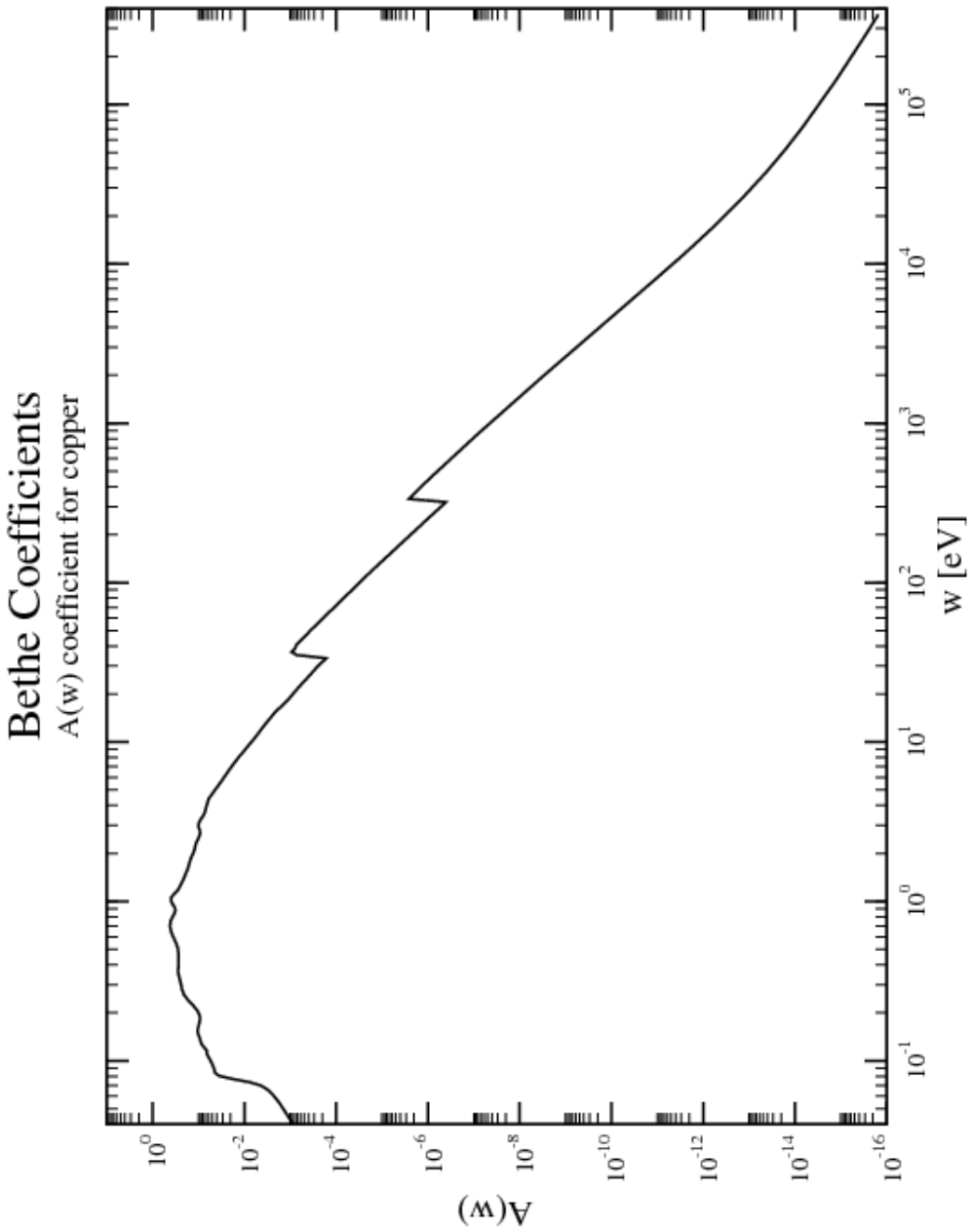

Figure 23: Bethe A coefficient, as defined in equation 114, for copper.

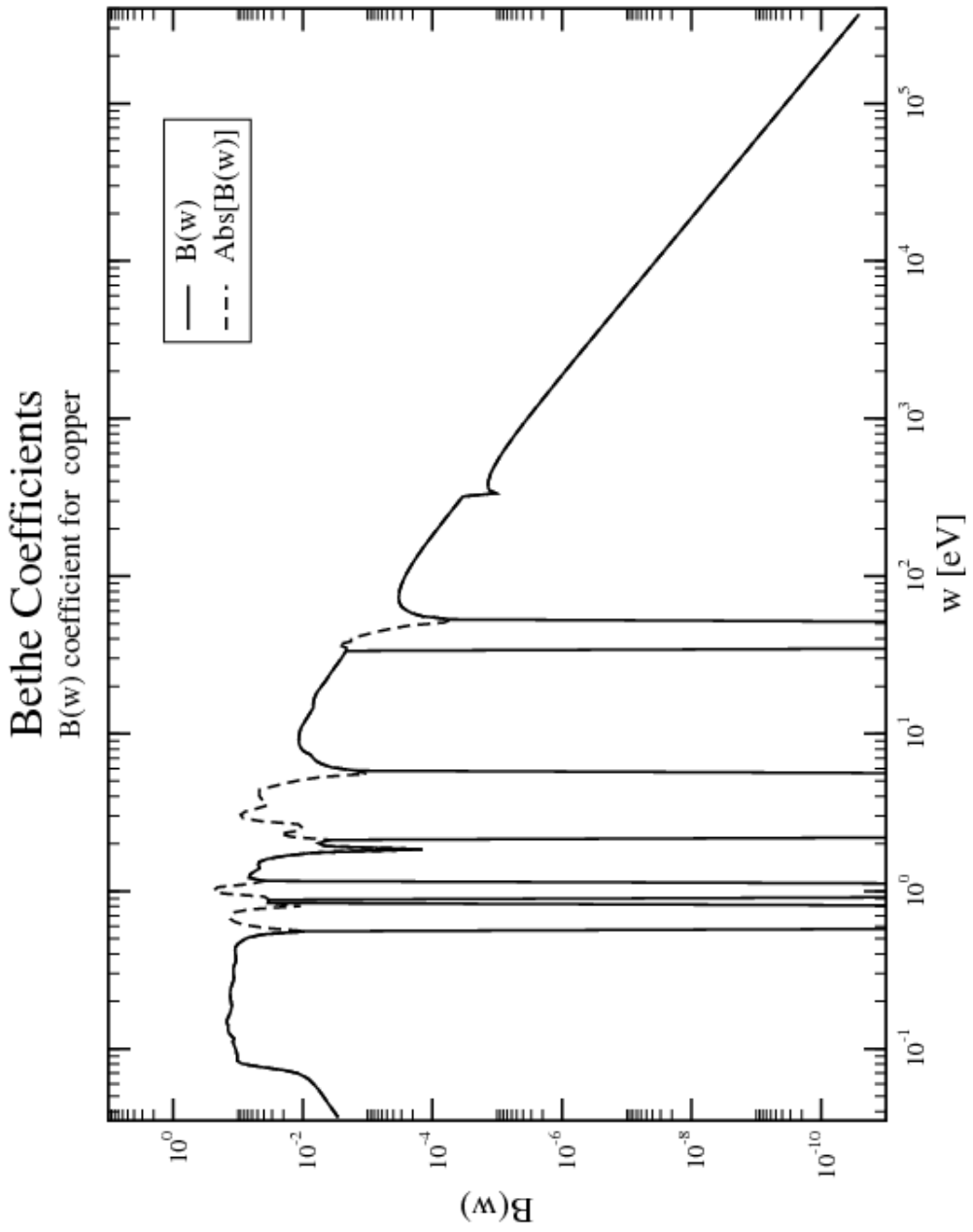

Figure 24: Bethe B coefficient, as defined in equation 115, for copper. The B coefficients as indicated by the dashed line are actually negative in value.

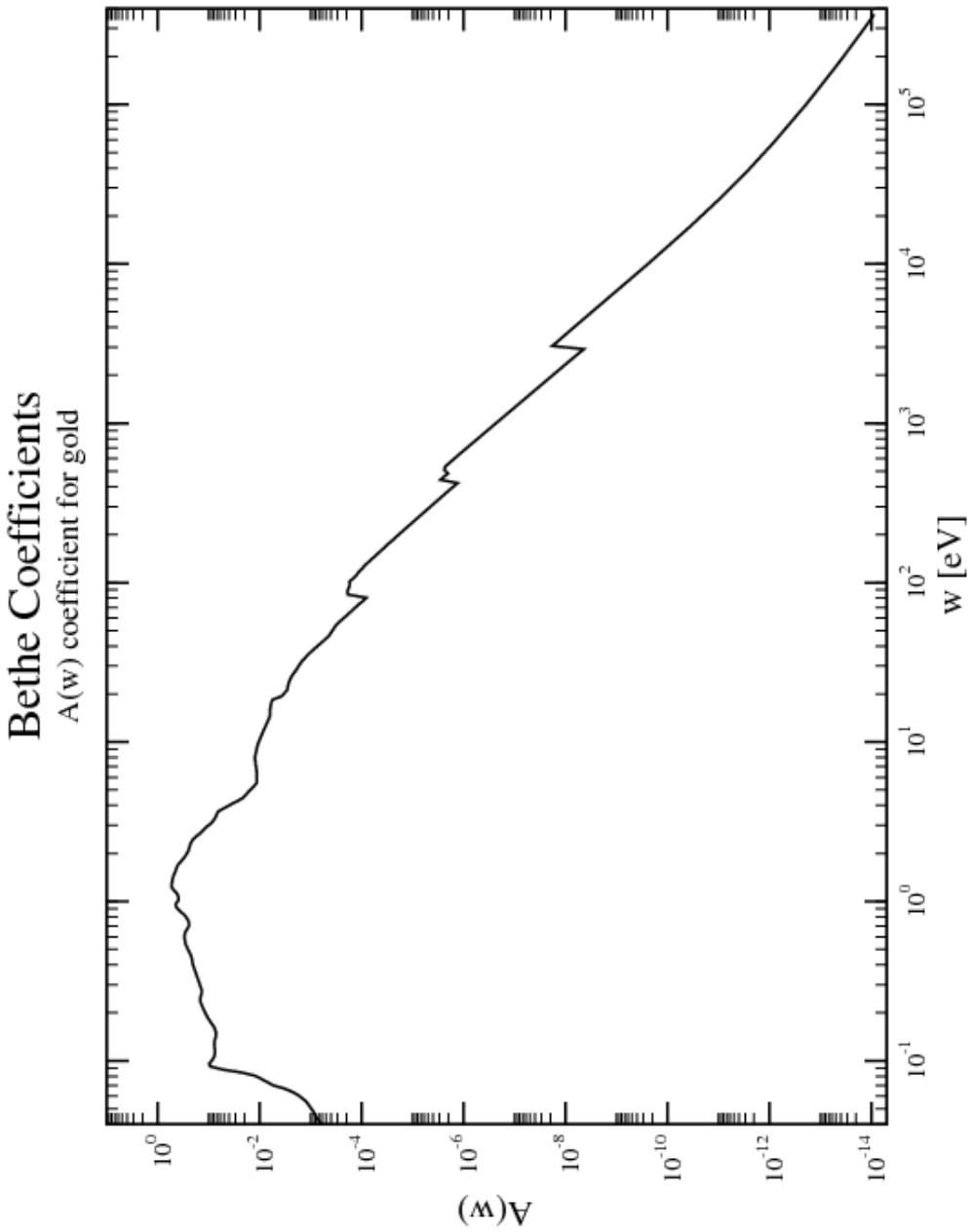

Figure 25: Bethe A coefficient, as defined in equation 114, for gold.

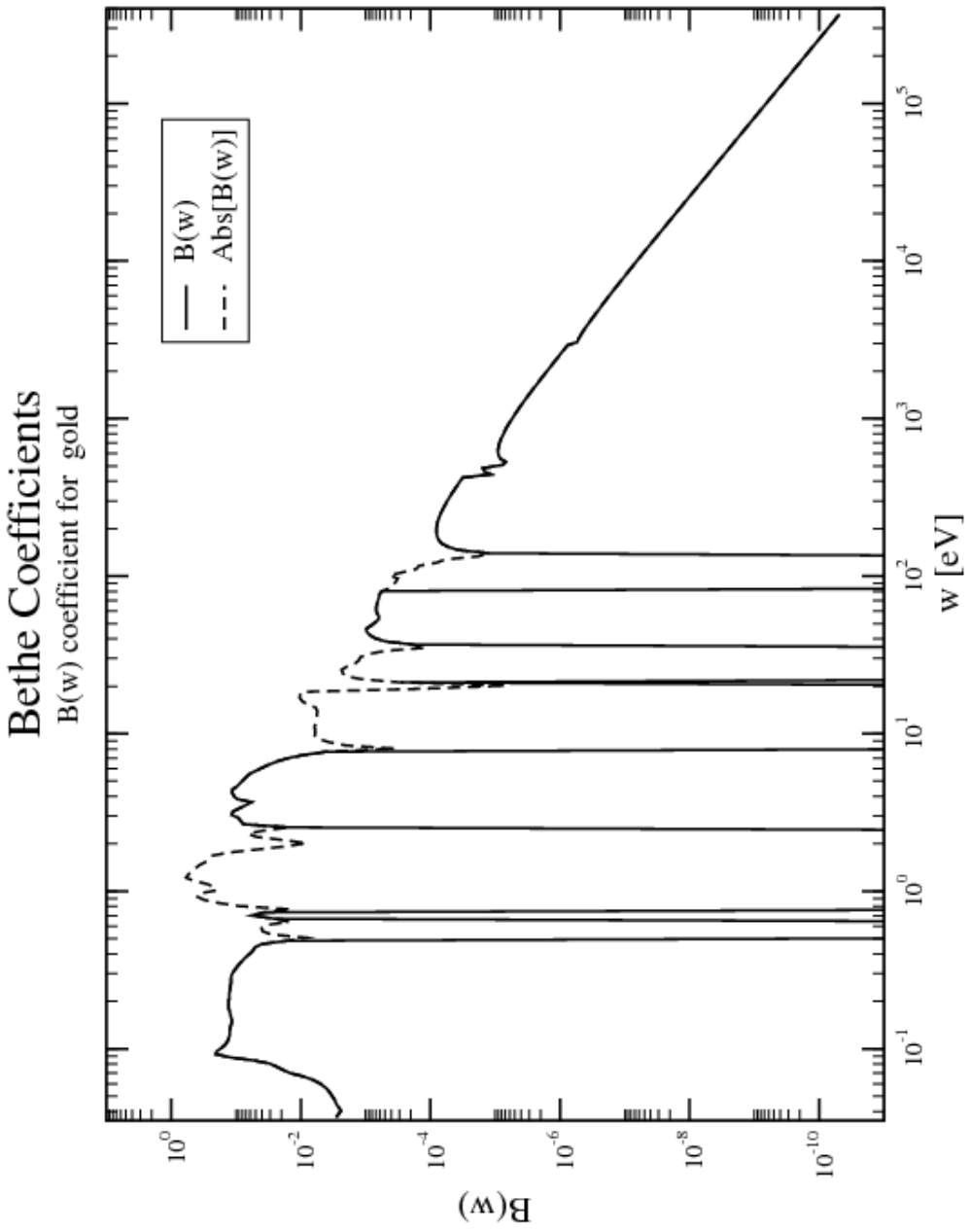

Figure 26: Bethe B coefficient, as defined in equation 115, for gold. The B coefficients as indicated by the dashed line are actually negative in value.

4 Results

Finally, we present the complete set of single differential inverse-mean-free-paths and the total macroscopic cross sections or inverse-mean-free-paths for electron and proton impact in isotropic and homogeneous aluminum, copper, and gold thin foils. We also show the PARTRAC simulation of the forward and backward electron yields from 0.1 micron thick copper foil after a 6 MeV proton impact.

Our calculations using the (PWFBA) are also compared with our calculations using the Bethe approach and other well known published data. For the inverse mean free path and stopping power of the foils for electron source the data was compared with results from Fernandez-Varea. et al. [39, 40]. The proton impact calculations were compared with well known data from ICRU report 49 [41].

4.1 Electron impact in aluminum, copper, and gold thin foils

4.1.1 Aluminum DIMFP, IMFP, and STP

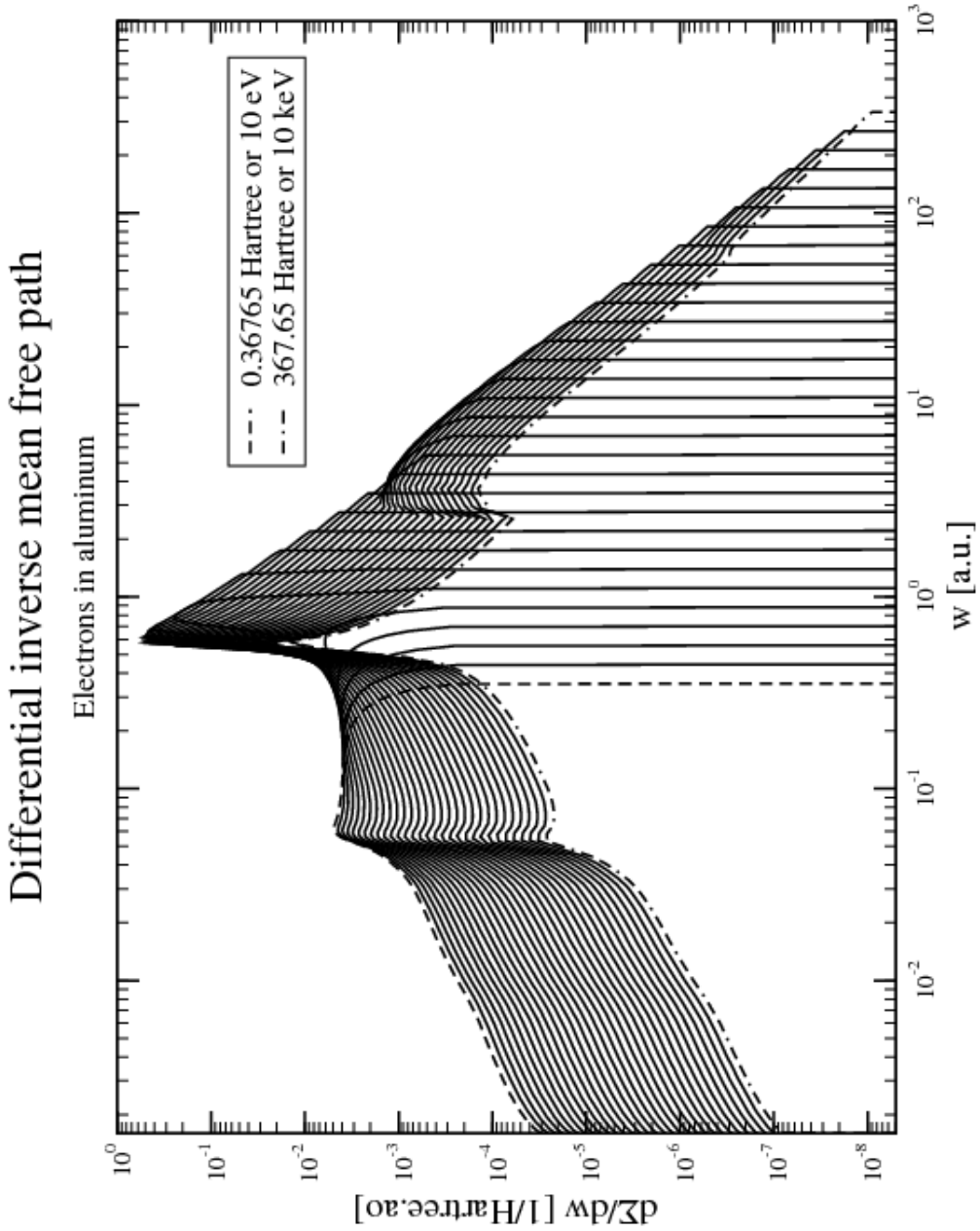

Figure 27: DIMFP of electrons in aluminum

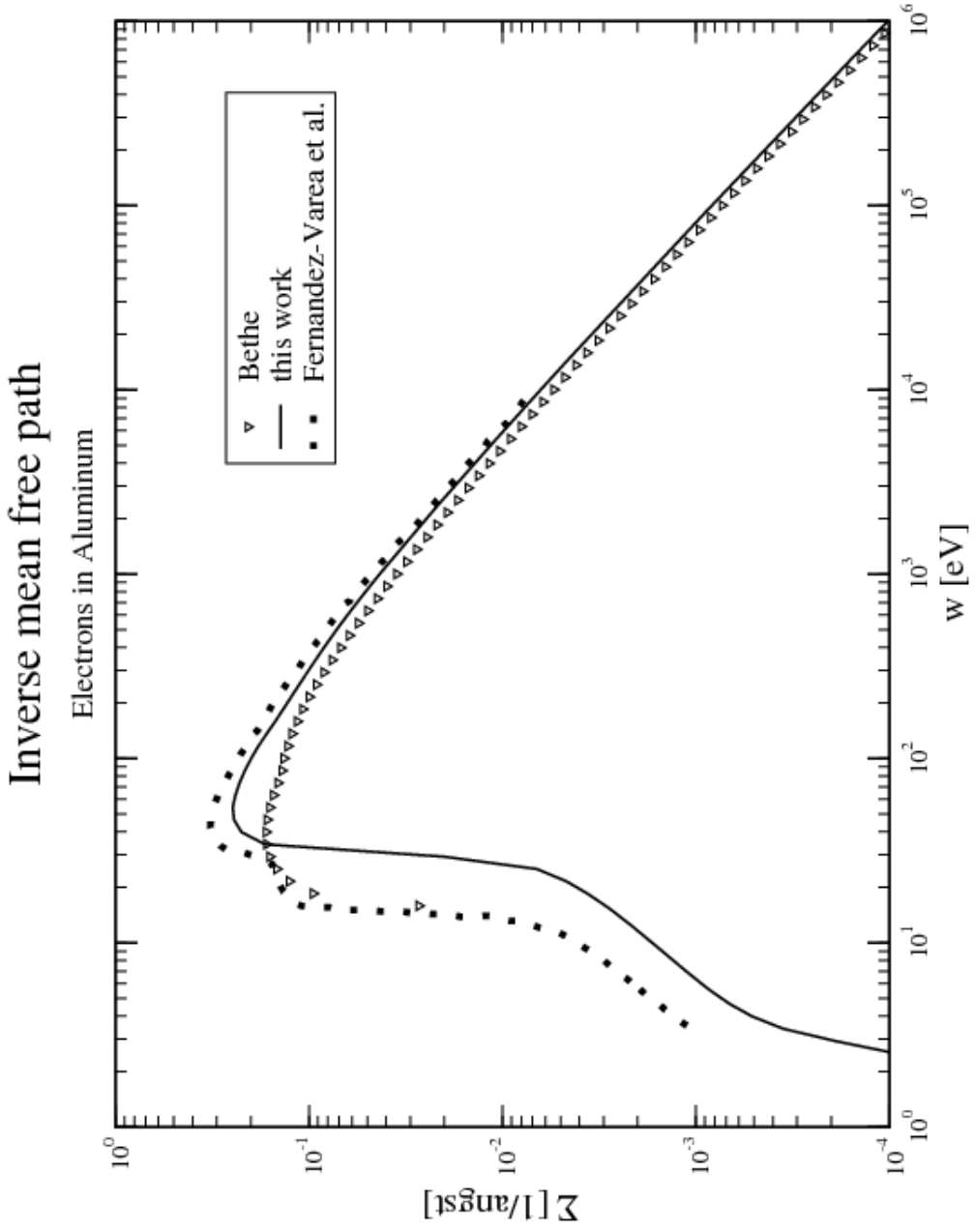

Figure 28: IMFP of electrons in aluminum. Data from

Fernandez- Varea et al. can be found in [39].

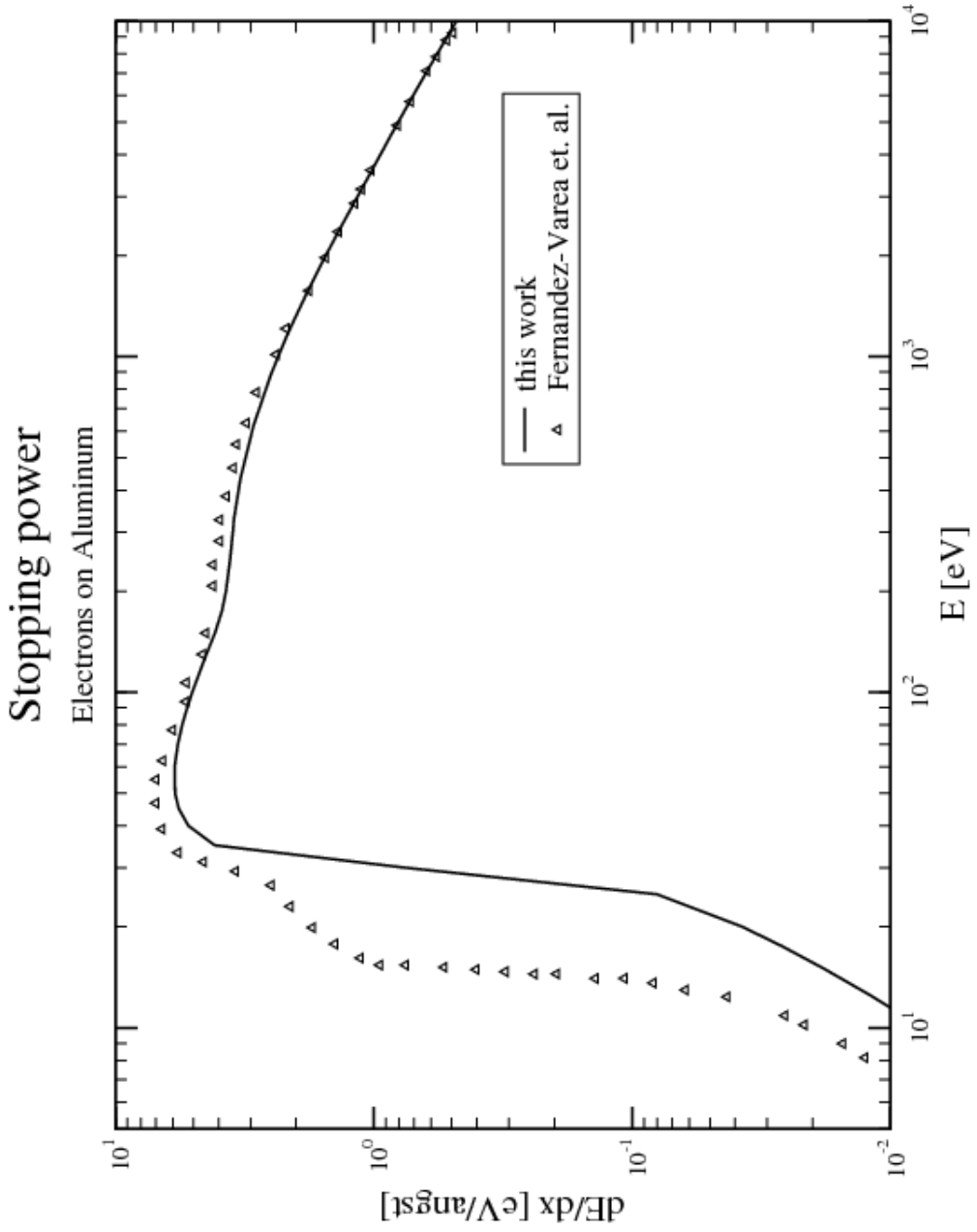

Figure 29: STP of aluminum for electron source. Data from

Fernandez- Varea et al. can be found in [39].

4.1.2 Copper DIMFP, IMFP, and STP

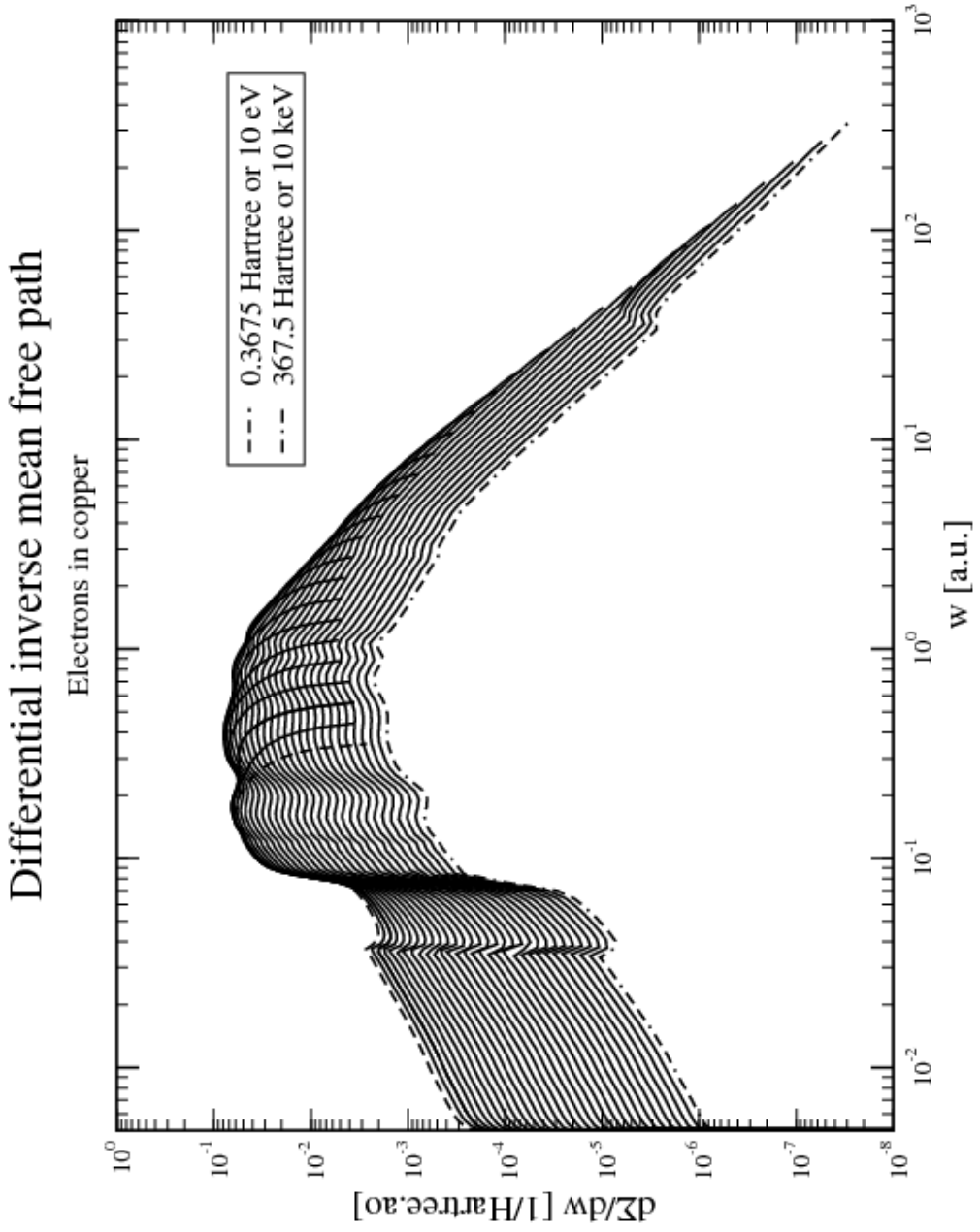

Figure 30: DIMFP of electrons in copper

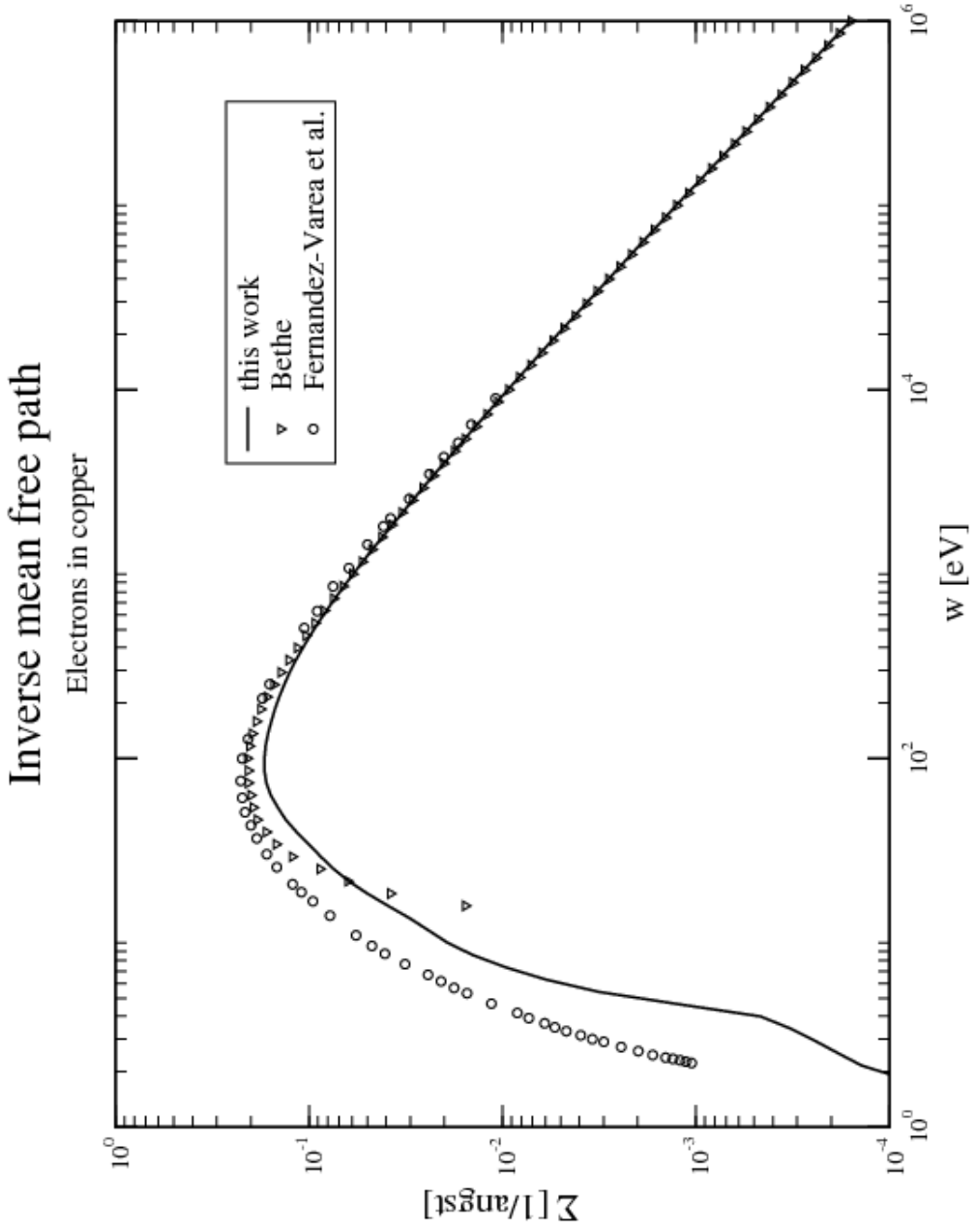

Figure 31: IMFP of electrons in copper. Data from

Fernandez- Varea et al. can be found in [39].

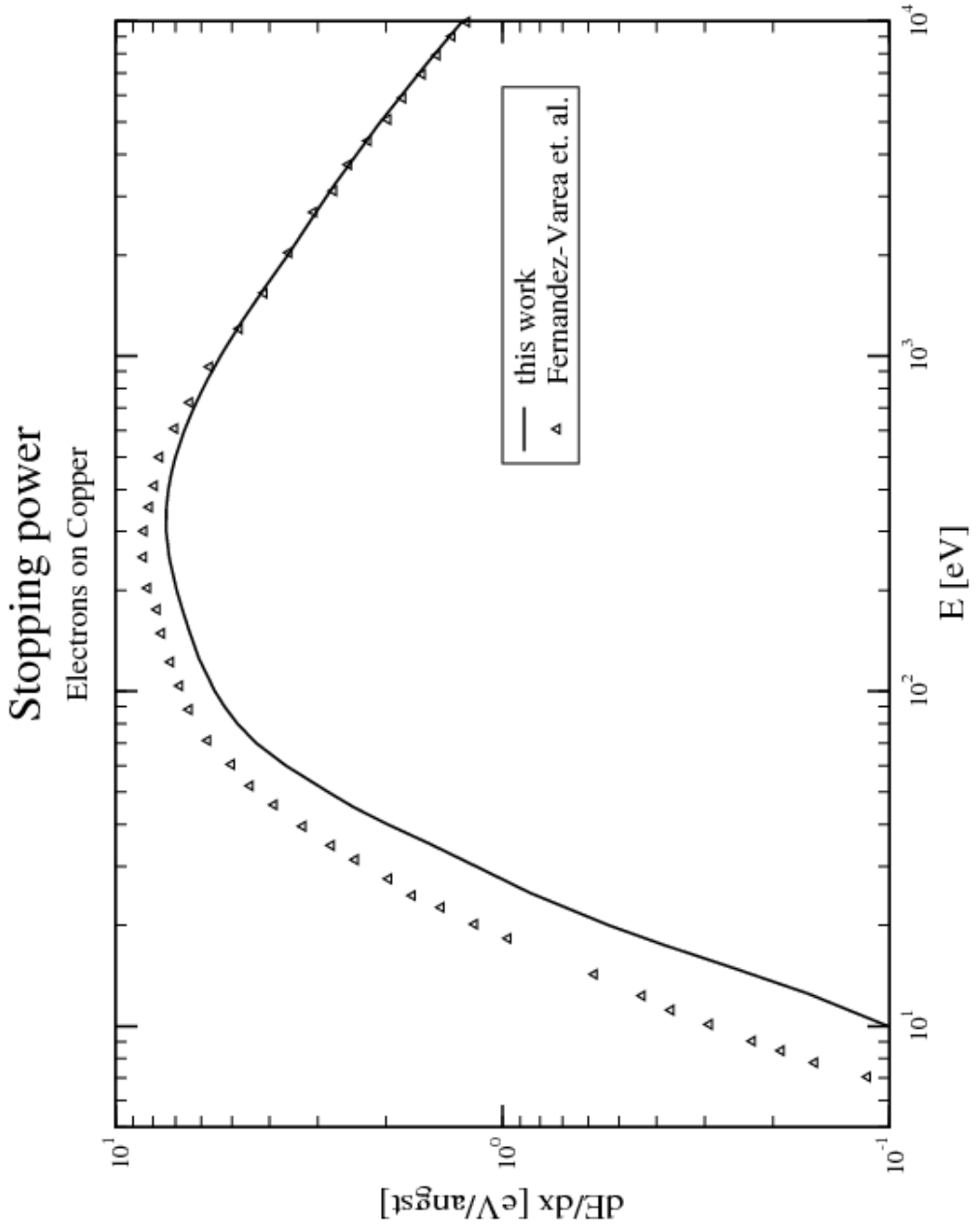

Figure 32: STP of copper for electron source. Data from

Fernandez- Varea et al. can be found in [39].

4.1.3 Gold DIMFP, IMFP, and STP

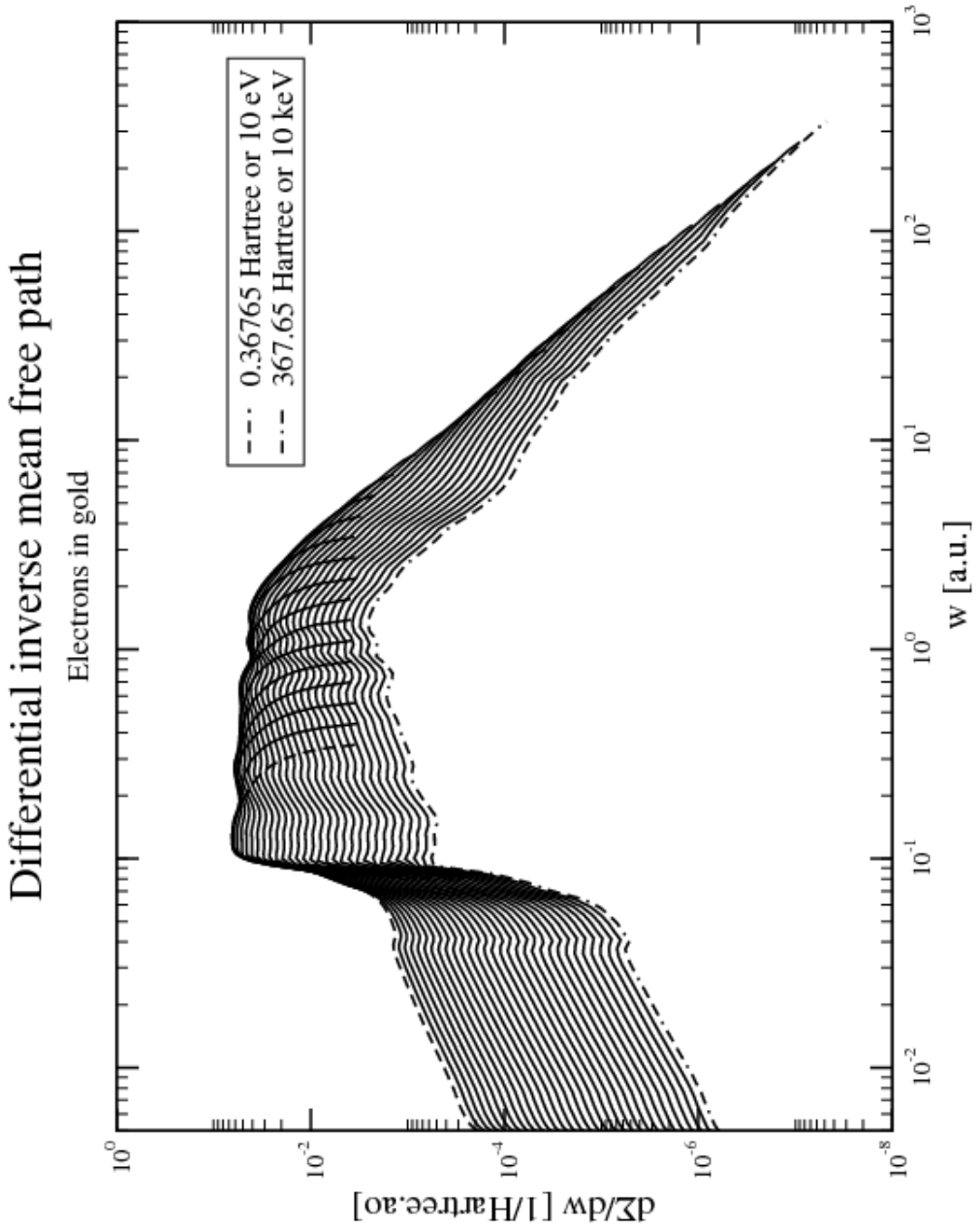

Figure 33: DIMFP of electrons in gold

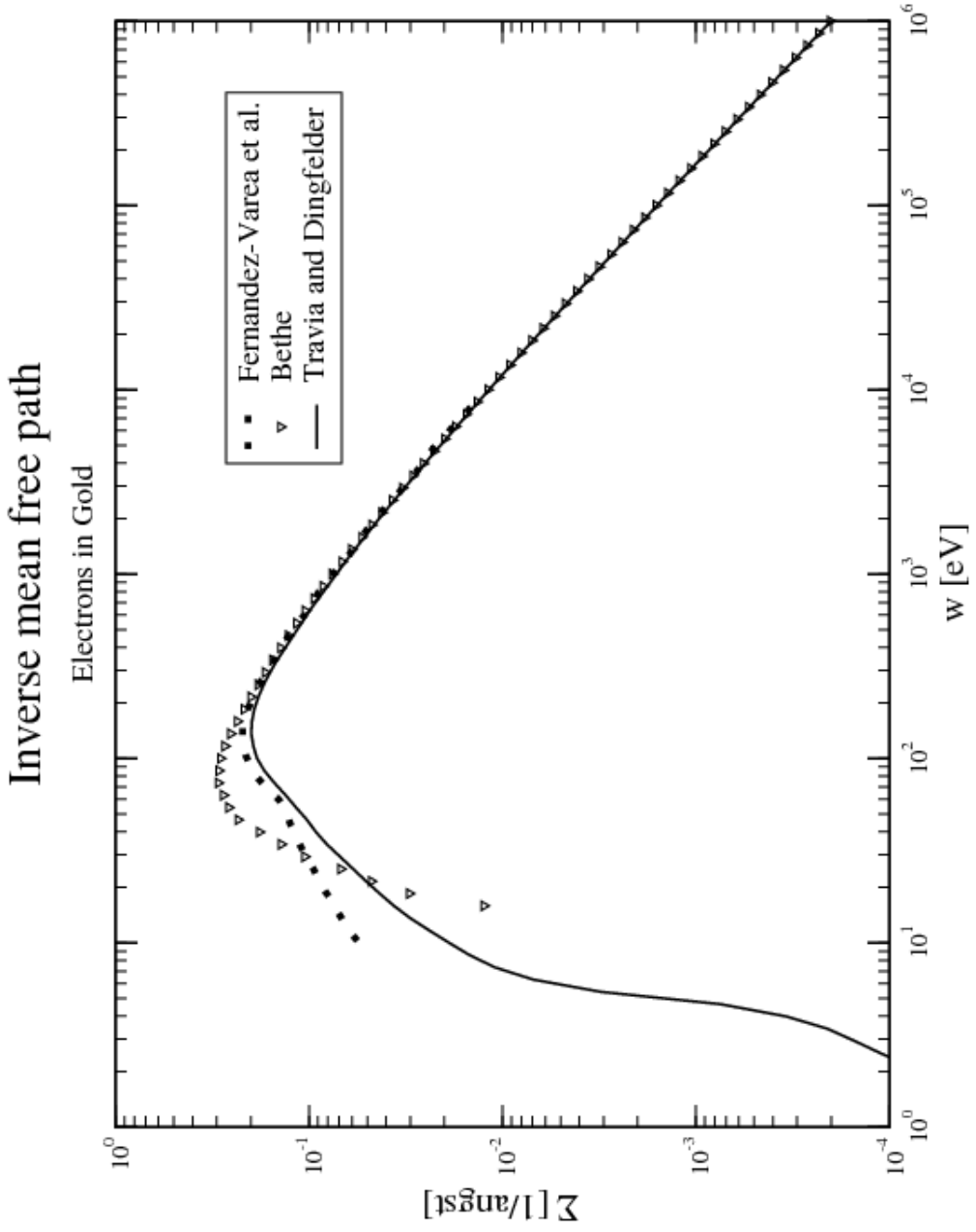

Fig 34: IMFP of electrons in gold. Data from

Fernandez- Varea et al. can be found in [40].

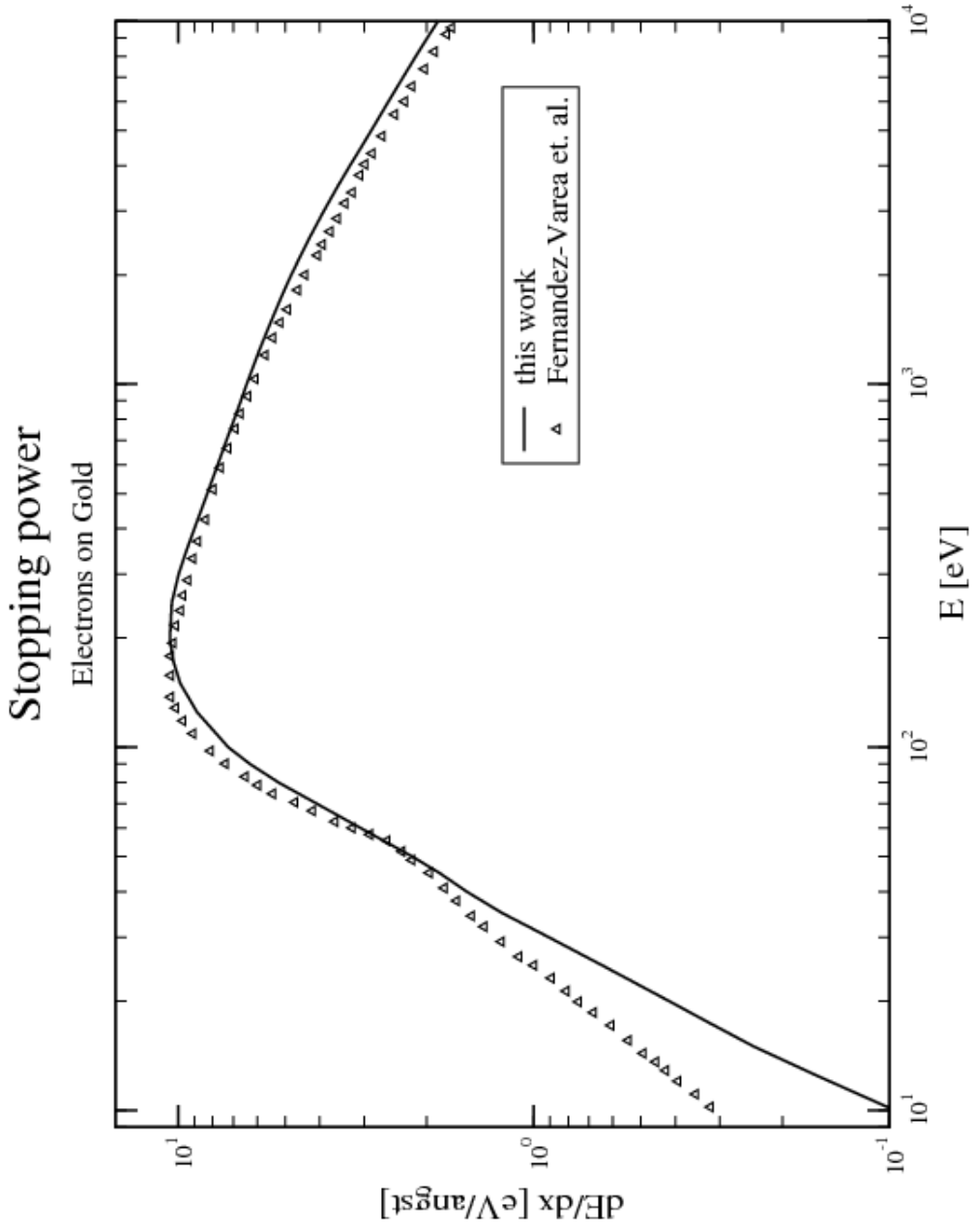

Figure 35: STP of gold for electron source. Data from

Fernandez- Varea et al. can be found in [40].

4.2 Proton impact in aluminum, copper, and gold thin foils

4.2.1 Aluminum DIMFP, IMFP, and mass STP

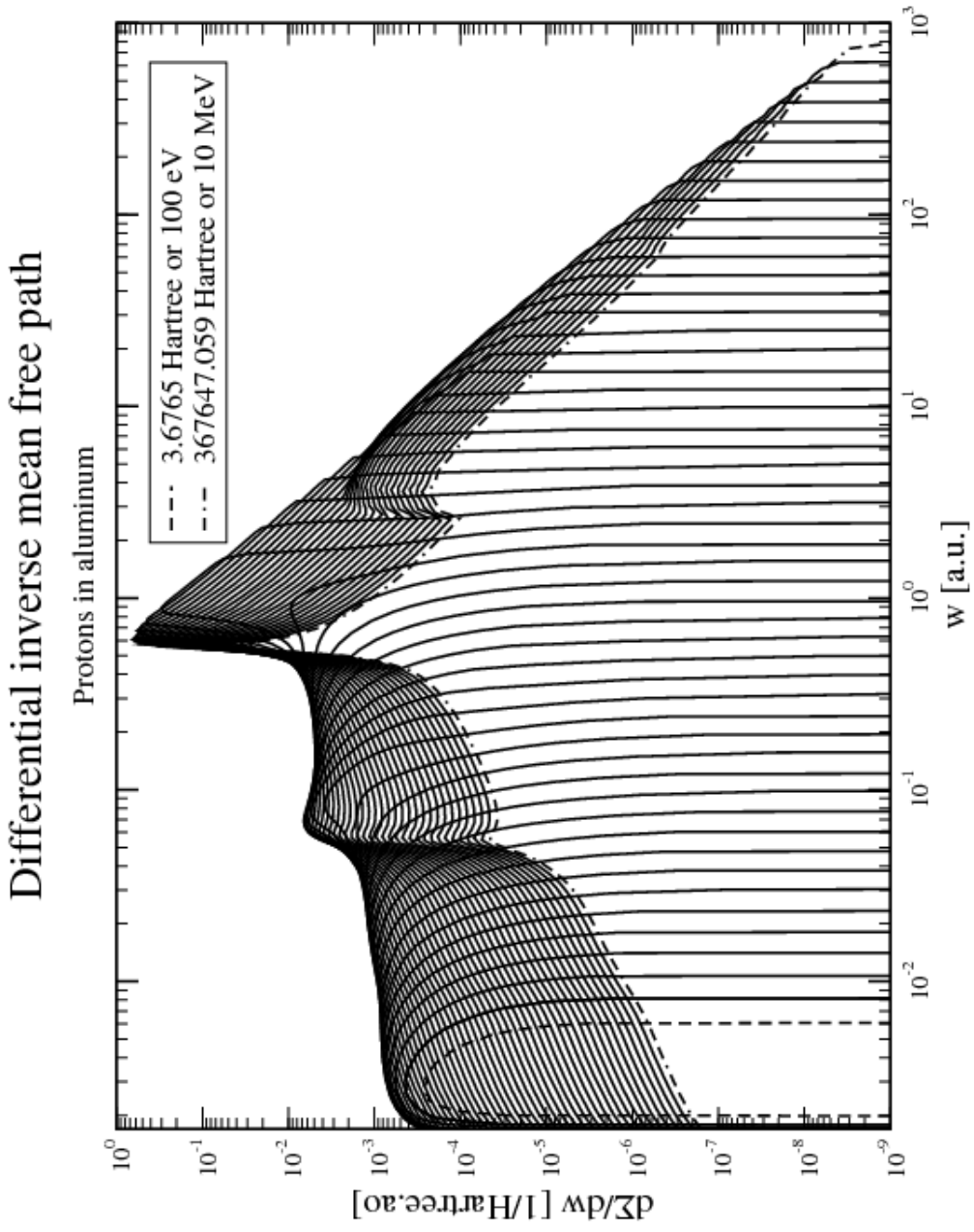

Figure 36: DIMFP of protons in aluminum

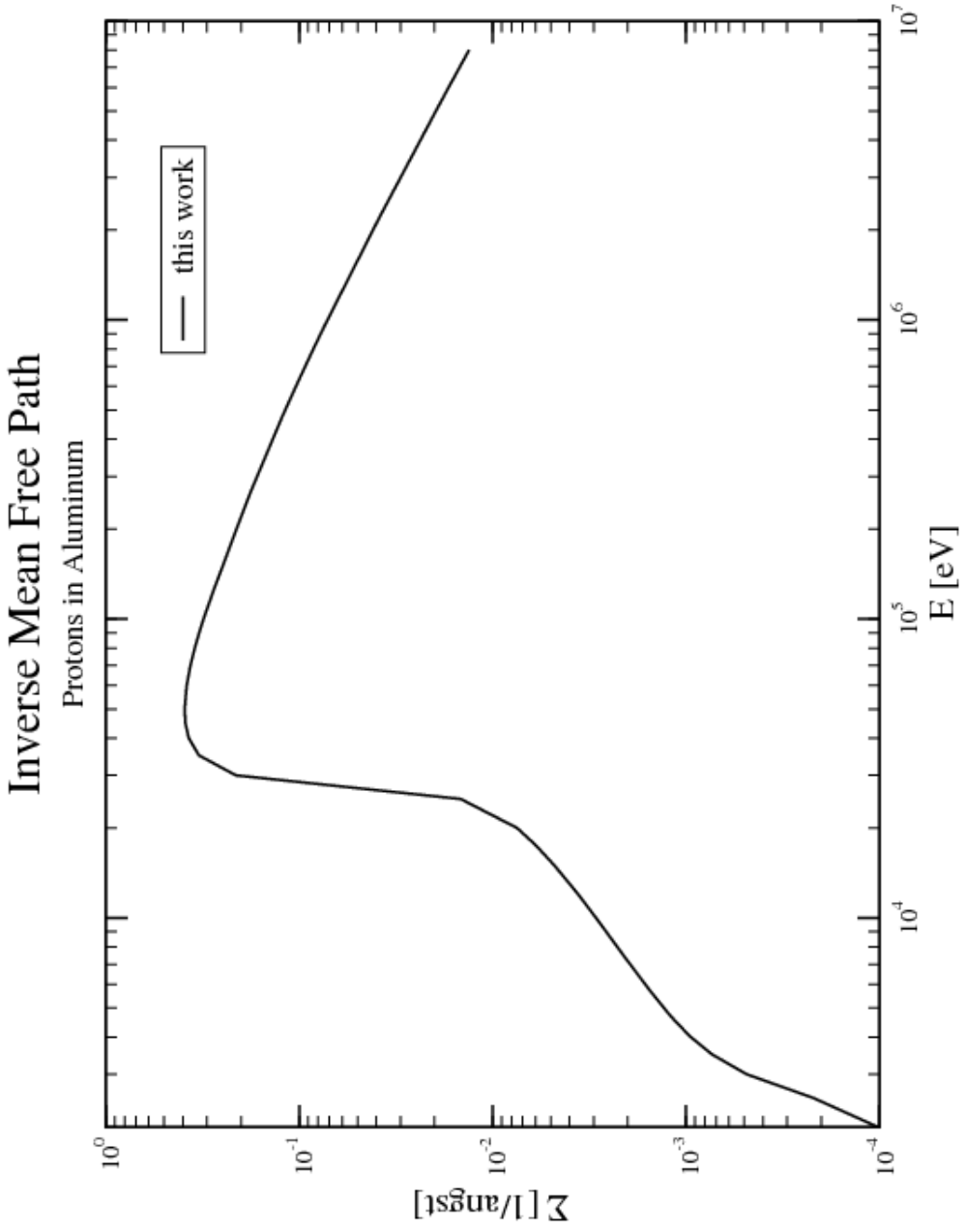

Figure 37: IMFP of protons in aluminum

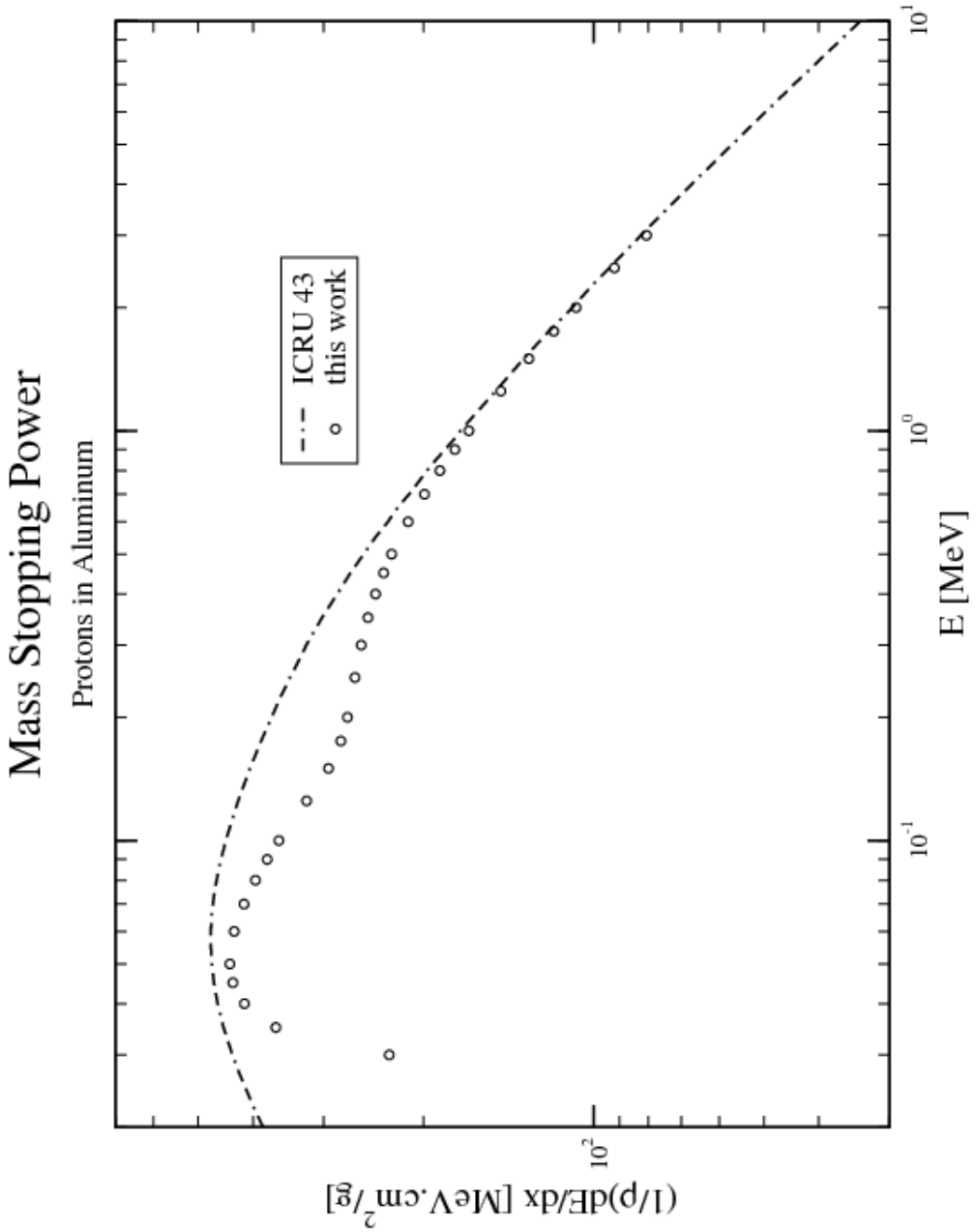

Figure 38: Mass STP of aluminum for proton source

4.2.2 Copper DIMFP, IMFP, and mass STP

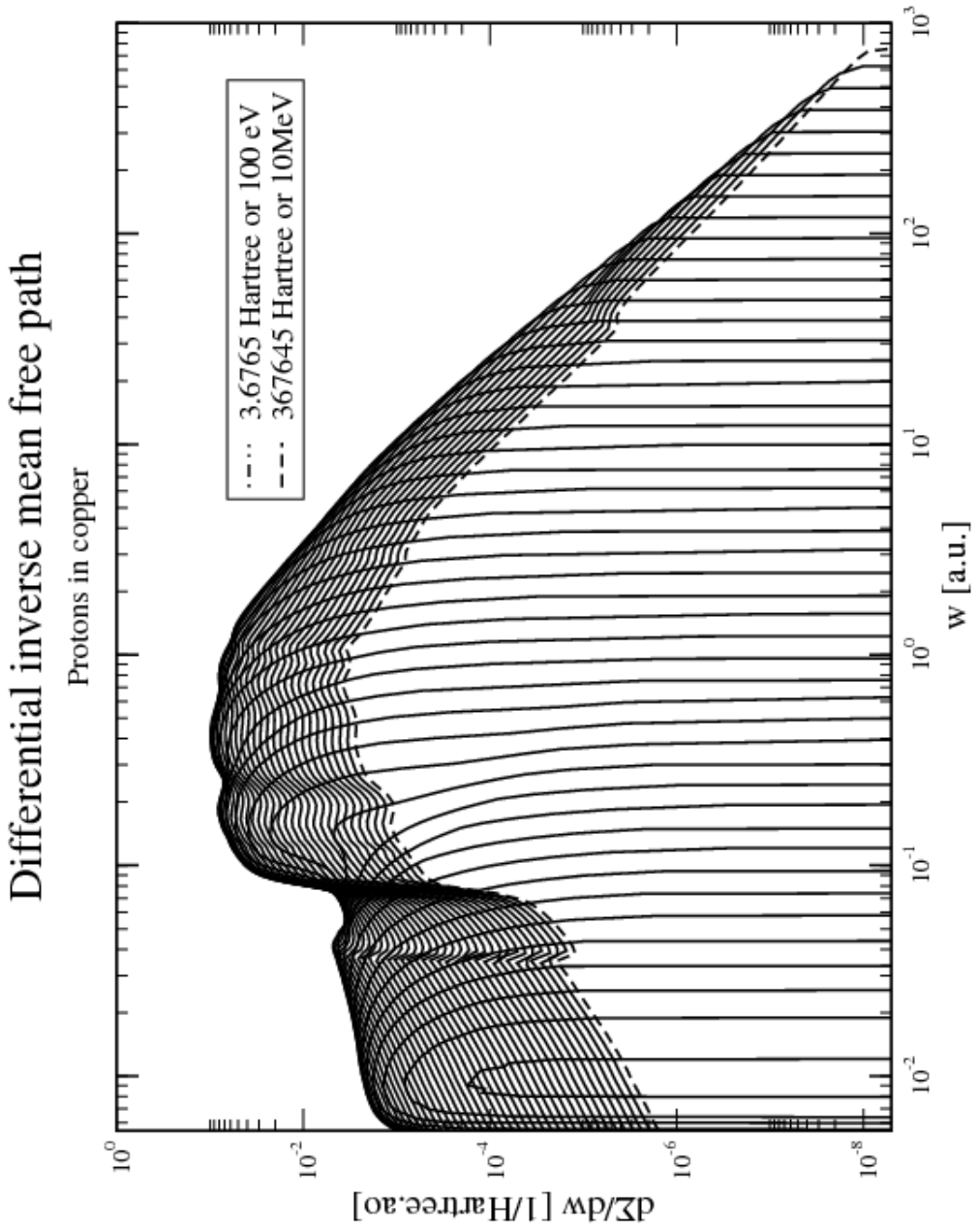

Figure 39: DIMFP of protons in copper

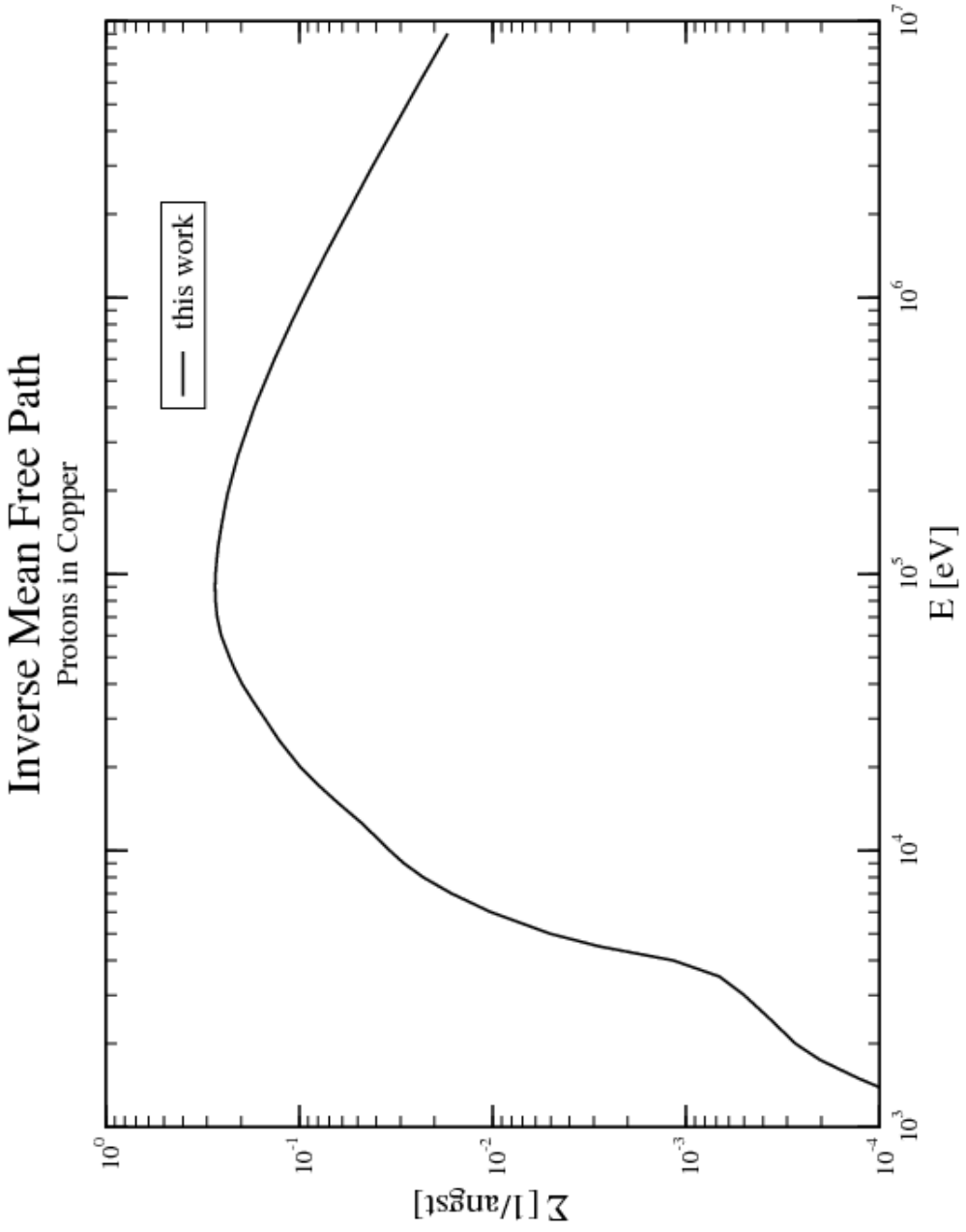

Figure 40: IMFP of protons in copper

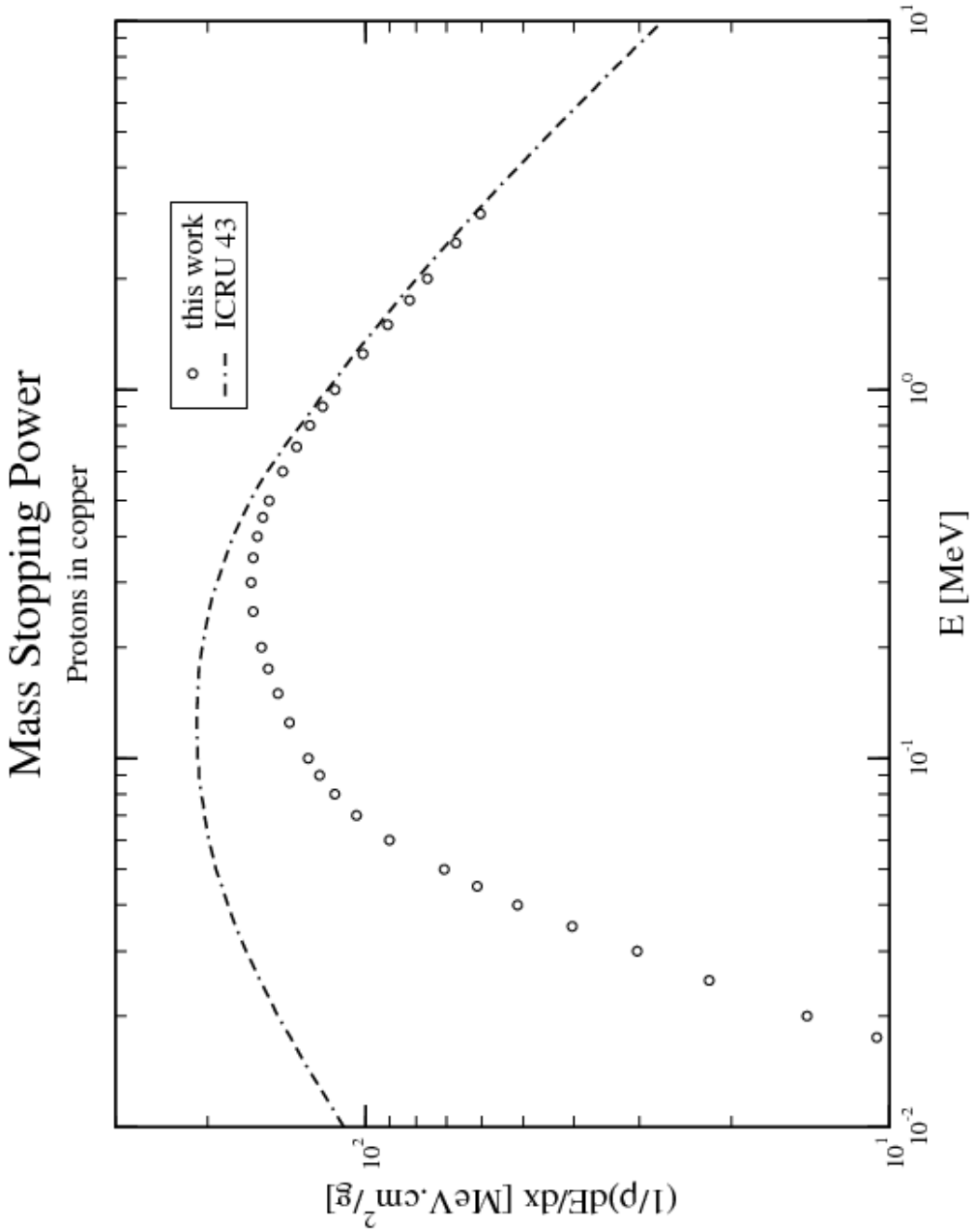

Figure 41: Mass STP of copper for proton source

4.2.3 Gold DIMFP, IMFP, and mass STP

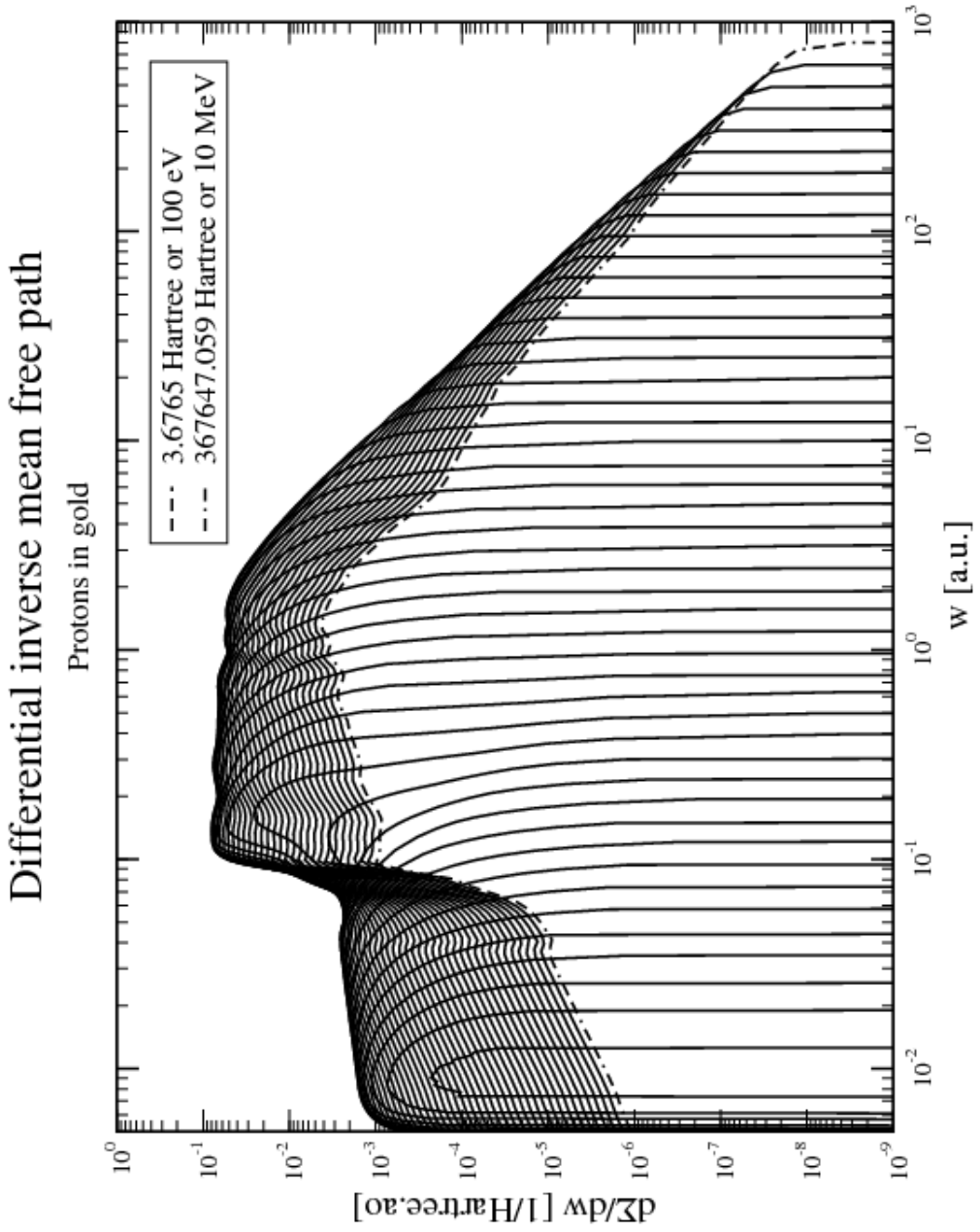

Figure 42: DIMFP of protons in gold

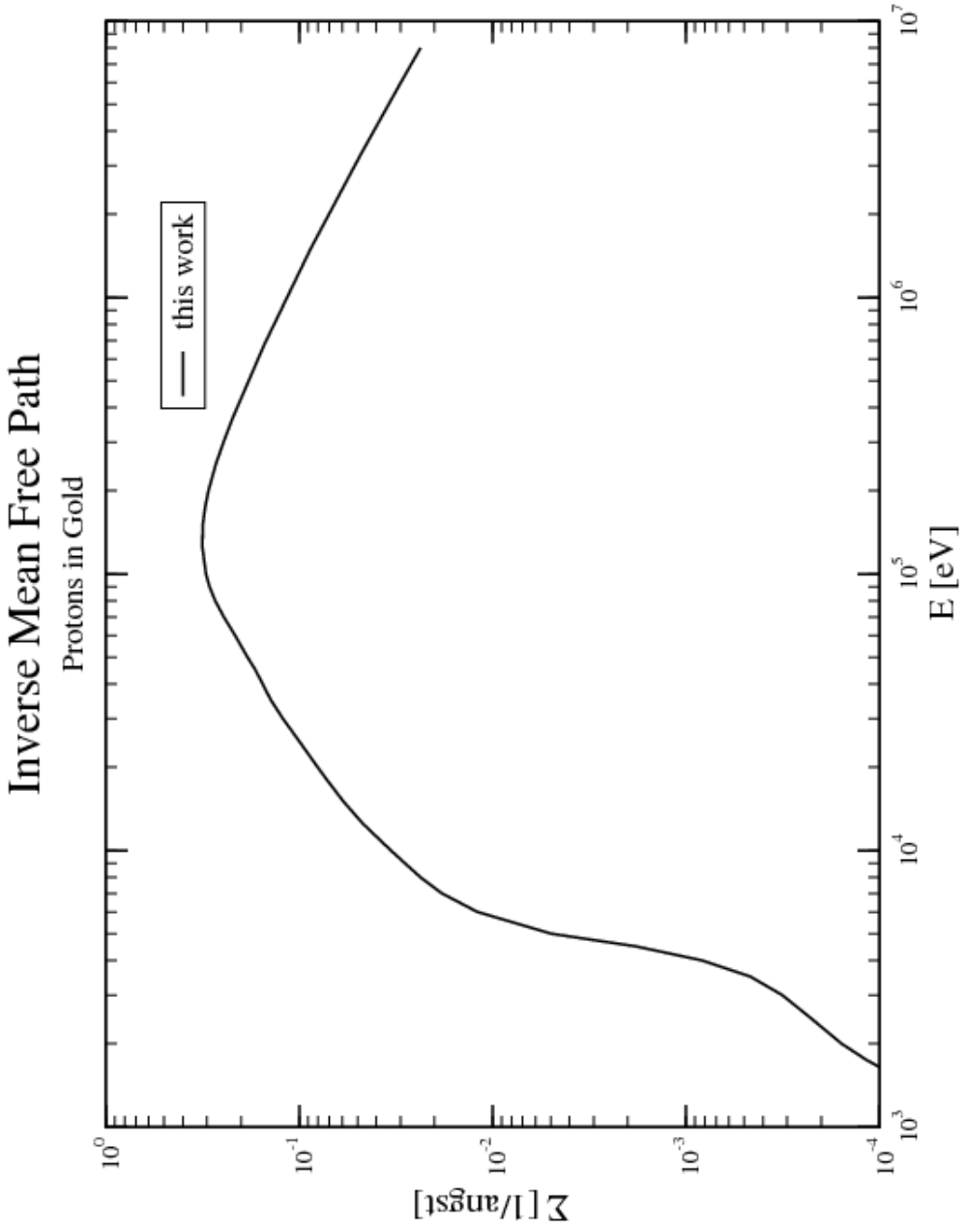

Figure 43: IMFP of protons in gold

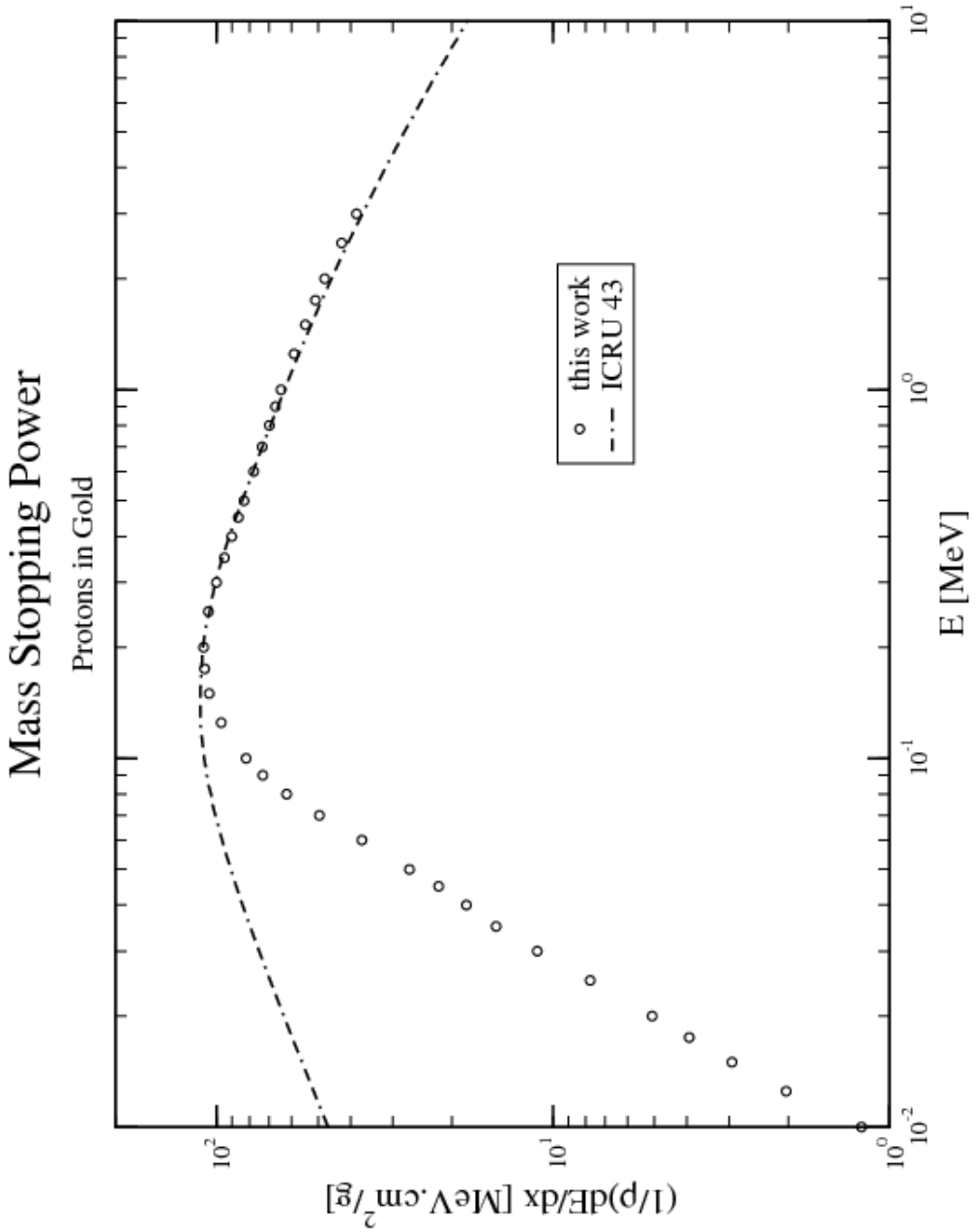

Figure 44: Mass STP of gold for proton source

4.3 Electron yields from 0.1 micron copper foil after 6 MeV proton impact

4.3.1 Forward electron yields

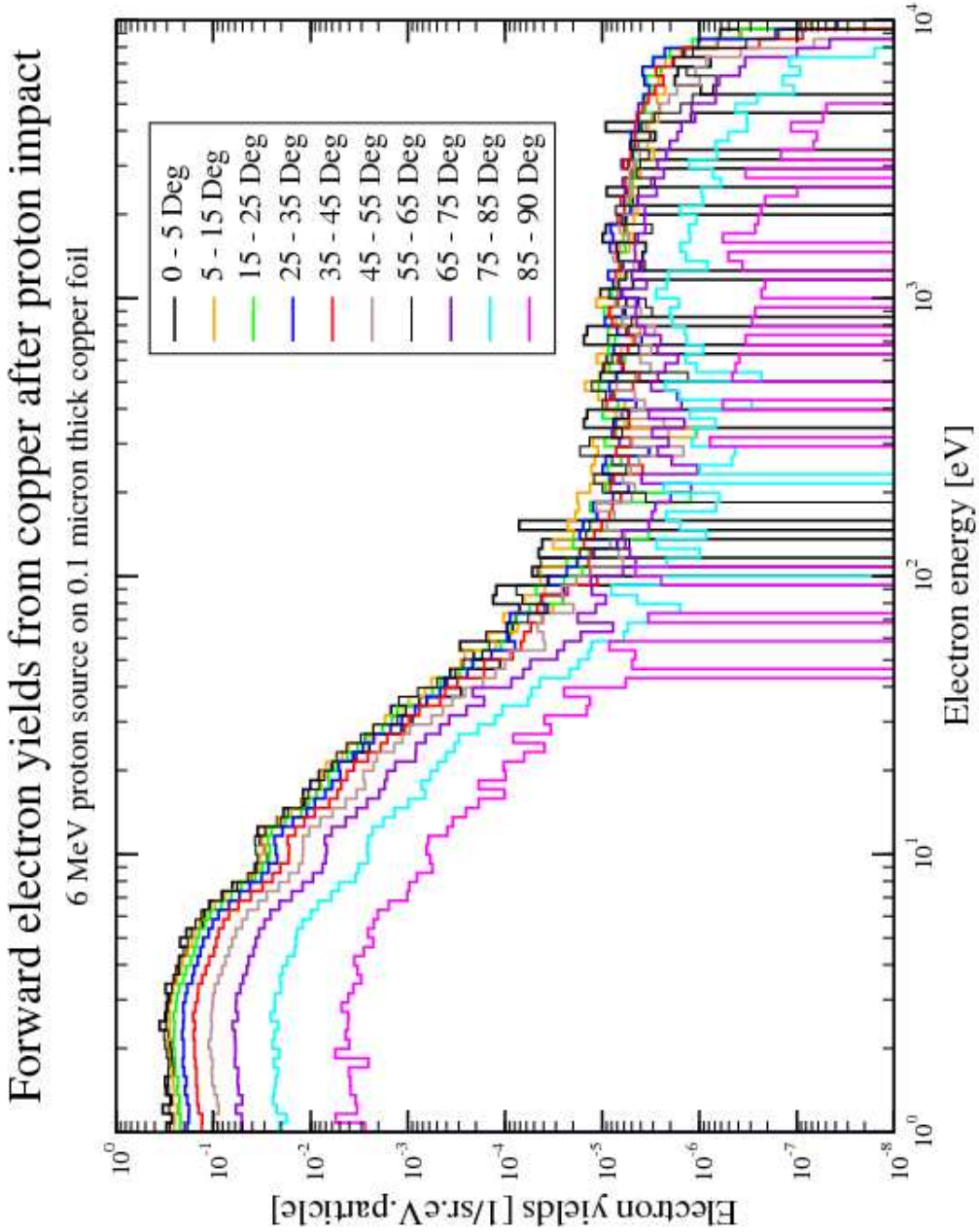

Figure 45: MC simulation of forward electron yields from copper foil.

Simulation data provided by Dr. Michael Dingfelder.

4.3.2 Backward electron yields

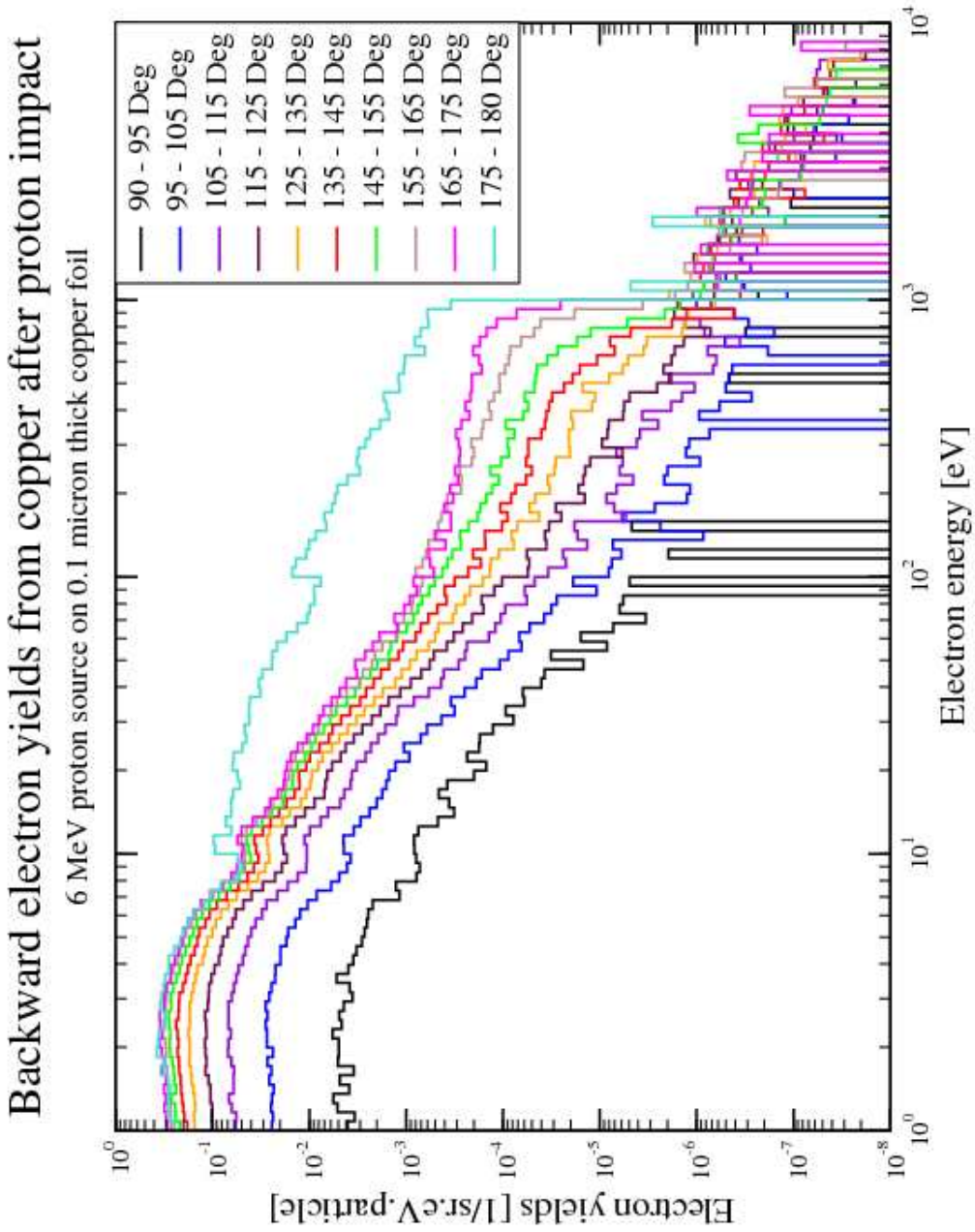

Figure 46: MC simulation of backward electron yields from copper foil.

Simulation data provided by Dr. Michael Dingfelder.

5 Conclusion and Remarks

In summary, the simulation of the secondary electron emission from a thin copper foil after fast proton impact has been accomplished using the Monte Carlo code PARTRAC after implementation of interaction cross sections calculated from dielectric theory under the PWFBA. This aloowed us to connect the most important quantity of the theory, the DDCS, to the GOS through a simple dispersion algorithm known as the δ-oscillator model and the available OOS of the target. After the DDCS was defined, the important quantities for the simulation could all be obtained by simple quadrature numerical methods.

As expected, the results are in agreement within the energy range ($>$ 1 keV for electron impact and $>$ 1 MeV for proton impact) in which the incident particle is considerd fast but still nonrelativistic compared with the average speed of the target electrons. Although our δ-oscillator model includes only the Bethe-ridge or the binary region of the surface and is clearly not the best representation available of these targets, equation 81, it satifies the simplicity requirement. It allows a simplification that is evident from our equation for the GOS and DDCS defined by equations 82 and 83 and obviously the numerical procedures for their implementation.

The continuation of this work could possibly concentrate on improvements in two fields:

- In the modelling of the Bethe surface of these targets. Rather than using a simple δ- function, the Bethe-ridge could be expanded with functions (Gaussian type functions) that allow for a greater momentum exchange interval around the binary ridge.
- In the numerical implementation - using more dynamical integration routines that account for pre-defined maximum allowed errors in place of simple quadrature schemes.

References

[1] J. E. Turner, Atoms, Radiation, and Radiation Protection (2007), WILEY- VCH Verlag GmbH & Co. KGaA, Weinheim, ISBN: 978-3-527-40606-7.

[2] G. R. Freeman, Kinetics of Nonhomogeneous Processes - A Practical Introduction for Chemists, Biologists, Physicists, and Material Scientists (1987), John Wiley & Sons, Inc., N.Y., ISBN: 0-471-8324-9.

[3] W. A. Glass, and M. N. Varma, Physical and Chemical Mechanisms in Molecular Radiation Biology, Basic Life Sciences Vol. 58 (1991), Plenum Press, N. Y., ISBN: 0-306-44110-1.

[4] M. Zaider, A. Y. C. Fung, J. Li, and J. Ladik, From Track Structure to Stochastic Chemistry and DNA Damage: Microdosimetry Perspective, Inter. Journal of Quantum Chem., vol 80 (2000), 327-340.

[5] L. H. Toburen, W. Friedland, M. Dingfelder, N. Ozturk, C. Christou, R. D. DuBois, G. Lapicki, J. L. Shinpaugh, C. G. Drexler, E. L. B. Justiniano, and H. G. Paretzke, Secondary Electron Production and Transport Induced by Fast Protons in Thin Foils, Application of Acc. in Research and Industry: 17th Int'l. Conference (2003), Am. Inst. of Phys., 0-7354-0149-7/03.

[6] J. D. Jackson, Classical Electrodynamics (1999), John Wiley & Sons, Inc., ISBN: 0-471-30932.

[7] L. Eyges, The Classical Electromagnetic Field (1972), Dover Publications, N. Y., ISBN: 0-486-63947-9.

[8] D. Atwood, Soft X-rays and Extreme Ultraviolet Radiation (1999), Cambridge University Press, ISBN:0-521-65214-6.

[9] G. R. Fowles, Introduction to Modern Optics (1989), Dover Publications, Inc., N. Y., ISBN:0-486-65957-7.

[10] M. L. Boas, Mathematical Methods in The Physical Sciences (1983), John Wiley & Sons, Inc., ISBN: 0-471-04409-1.

[11] G. B. Arfken and H. J. Weber, Mathematical Methods for Physicists (2001), Harcourt Academic Press, ISBN: 0-12-059825-6.

[12] M. Fox, Optical Properties of Solids - Oxford Master Series in Condensed Matter Physics Vol.I (2001), Oxford University Press Inc., N. Y., ISBN: 0198506120.

[13] L. D. Landau, E. M. Lifshitz, and L. P. Pitaevskiĭ, Electrodynamics of Continuous Media - Landau and Lifshitz Course of Theoretical Physics Vol. 8 (1984), Pergamon Press Ltd., ISBN: 0-08-030276-9.

[14] M. Inokuti, Inelastic Collisions of Fast Charged Particles with Atoms and Molecules - The Bethe Theory Revisited (1971), Rev. of Mod. Phys. 43 (3), 297-347.

[15] M. Inokuti, Y. Itikawa, J. E. Turner, Addenda: Inelastic collisions of fast charged particles with atoms and molecules (1971) [Rev. Mod. Phys. 43, 297] – The Bethe theory revisited, Rev. of Mod. Phys. 50 (1), Part I (1978), 23-35.

[16] H. A. Bethe, R. Jackiw, Intermediate Quantum Mechanics (1986), Westview Press, ISBN: 0-201-32831-3.

[17] E. Fermi, The Ionization Loss of Energy in Gases an in Condensed Materials (1940), Phys. Rev. 57, 485.

[18] J. Hubbard, The Dielectric Theory of Electronic Interactions in Solids (1955), Proc. Phys. Soc. A 68, 976-986.

[19] U. Fano, Penetration of Protons, Alpha Particles, and Mesons (1963), Ann. Rev. Nucl. Sci. 13, 1-66.

[20] K. L. Bell, D. J. Kennedy, and A. E. Kingston, Excitation of helium by fast electrons (1968), J. Phys. B (Proc. Phys. Soc.), ser. 2, vol. 1.

[21] K. L. Bell, D. J. Kennedy, and A. E. Kingston, Excitation of helium by fast protons (1968), J. Phys. B (Proc. Phys. Soc.), ser. 2, vol. 1.

[22] A. Szabo, and N. S. Ostlund, Modern Quantum Chemistry - Introduction to Advanced Electronic Structure Theory (1982), Dover Publications, Inc., N.Y., ISBN: 0-486-69186-1.

[23] D. B. Cook, Handbook of Computational Quantum Chemistry (1998), Dover Publications N. Y., ISBN: 0-486-44307.

[24] D. Emfietzoglou, A. Pathak, and M. Moscovitch, Modeling the energy and momentum dependent loss function of the valence shells of liquid water (2005), Nucl. Instr. and Meth. in Phys. Res. B 230, 77-84.

[25] E. D. Palik, Handbook of Optical Constants of Solids (1985), Academic Press Inc., N. Y., ISBN: 0-12-544420-6.

[26] NIST, National Institute of Standards and Technology - Physics Laboratory, http://physics.nist.gov/PhysRefData/Xcom/html/xcom1.html

[27] M. Dingfelder, D. Hantke, M. Inokuti, and H. G. Paretzke, Electron inelastic-scattering cross sections in liquid water (1998), Rad. Phys. and Chem. 53, 1-18.

[28] M. Dingfelder, M. Inokuti, H. G. Paretzke, Inelastic-collision cross sections of liquid water for interactions of energetic protons (2000), Rad. Phys. and Chem. 59, 255-275.

[29] N. W. Ashcroft, N. D. Mermin, Solid State Physics (1976), Thomson Lerning Inc., ISBN: 0-03-083993-9.

[30] J. C. Ashley, Optical-data model for the stopping power of condensed matter for protons and antiprotons (1991), J. Phys.: Condens. Matter 3, 2741-2753.

[31] M. Dingfelder, R. H. Ritchie, J. E. Turner, W. Friedland, H. G. Paretzke, and R. N. Hamm, Comparisons of Calculations with PARTRAC and NOREC: Transport of Electrons in Liquid Water (2008), Rad. Res. 169, 584-594.

[32] M. H. Kalos and P. A. Whitlock, Monte Carlo Methods, vol. 1 (1986), Jon Wiley & Sons, Inc., N.Y., ISBN:0-471-89839-2.

[33] F. Salvat, J. M. Fern*á*ndez-Varea, E. Acosta, and J. Sempau, PENELOPE - A Code System for Monte Carlo Simulation of Electron and Photon Transport (2001), Workshop Proceedings Issy-les-Moulineaux, France, ISBN: 92-64-18475-9.

[34] C. B. Opal, E. C. Beaty, and W. K. Peterson, Tables of Energy and Angular Distributions of Electrons Ejected from Simple Gases by Electron Impact, Report No. 108, Joint Institute for Laboratory Astrophysics (JILA), Boulder, CO, (1971).

[35] C. B. Opal, E. C. Beaty, and W. K. Peterson, Tables of secondary electron production cross sections, Atomic Data 4, 209 (1972).

[36] M. Dingfelder, Cross section calculations in condensed media: charged particles in liquid water, Rad. Protec. Dosim. 99, Nos 1-4, (2002) 23-28.

[37] Y. -Ki Kim, Angular Distribution od secondary electrons in the dipole approximation, Phys. Rev. A. 6, No 2, (1972) 666-670.

[38] Y. -Ki Kim and M. Eugene Rudd, Binary-encounter-dipole model for electron-impact ionization, Phys. Rev. A. 50 (5), (1994), 3954-3967.

[39] J. M. Fern*á*ndez-Varea, R. Mayol, F. Salvat, and D. Liljequist, A comparison onf inelastic electron scattering models based on δ-function representations of the Bethe surface, J. Phys.: Condens. Matter 4 (1992) 2879-2890.

[40] J. M. Fern*á*ndez-Varea, R. Mayol, D. Liljequist, and F. Salvat, Inelastic scattering of electrons in solids from a generalized oscillator strength model using optical and photoelectric data, J. Phys.: Condens. Matter 5 (1993) 3593-3610.

[41] ICRU Report 49, Stopping power and ranges for protons and alpha particles, International Commission on Radiation Units and Measurements.